DYNAMIC FLUORESCENCE IMAGING WITH MOLECULAR AGENTS FOR CANCER DETECTION

A Dissertation

by

SUN KUK KWON

Submitted to the Office of Graduate Studies of
Texas A&M University
in partial fulfillment of the requirements for the degree of

DOCTOR OF PHILOSOPHY

December 2006

Major Subject: Chemical Engineering

DYNAMIC FLUORESCENCE IMAGING WITH MOLECULAR AGENTS FOR CANCER DETECTION

A Dissertation

by

SUN KUK KWON

Submitted to the Office of Graduate Studies of
Texas A&M University
in partial fulfillment of the requirements for the degree of

DOCTOR OF PHILOSOPHY

Approved by:

Chair of Committee,	Eva M. Sevick-Muraca
Committee Members,	Daniel F. Shantz
	Gerard L. Cote
	Michael A. Bevan
Head of Department,	Nagamangala K. Anand

December 2006

Major Subject: Chemical Engineering

ABSTRACT

Dynamic Fluorescence Imaging with Molecular Agents for Cancer Detection.

(December 2006)

Sun Kuk Kwon, B.S., Hanyang University

Chair of Advisory Committee: Dr. Eva M. Sevick-Muraca

Non-invasive dynamic optical imaging of small animals requires the development of a novel fluorescence imaging modality. Herein, fluorescence imaging is demonstrated with sub-second camera integration times using agents specifically targeted to disease markers, enabling rapid detection of cancerous regions. The continuous-wave fluorescence imaging acquires data with an intensified or an electron-multiplying charge-coupled device. The work presented in this dissertation (i) assessed dose-dependent uptake using dynamic fluorescence imaging and pharmacokinetic (PK) models, (ii) evaluated disease marker availability in two different xenograft tumors, (iii) compared the impact of autofluorescence in fluorescence imaging of near-infrared (NIR) vs. red light excitable fluorescent contrast agents, (iv) demonstrated dual-wavelength fluorescence imaging of angiogenic vessels and lymphatics associated with a xenograft tumor model, and (v) examined dynamic multi-wavelength, whole-body fluorescence imaging with two different fluorescent contrast agents.

PK analysis showed that the uptake of Cy5.5-c(KRGDf) in xenograft tumor regions linearly increased with doses of Cy5.5-c(KRGDf) up to 1.5 nmol/mouse. Above

1.5 nmol/mouse, the uptake did not increase with doses, suggesting receptor saturation. Target to background ratio (TBR) and PK analysis for two different tumor cell lines showed that while Kaposi's sarcoma (KS1767) exhibited early and rapid uptake of Cy5.5-c(KRGDf), human melanoma tumors (M21) had non-significant TBR differences and early uptake rates similar to the contralateral normal tissue regions. The differences may be due to different compartment location of the target.

A comparison of fluorescence imaging with NIR vs. red light excitable fluorescent dyes demonstrates that NIR dyes are associated with less background signal, enabling rapid tumor detection. In contrast, animals injected with red light excitable fluorescent dyes showed high autofluorescence.

Dual-wavelength fluorescence images were acquired using a targeted ^{111}In-DTPA-K(IRDye800)-c(KRGDf) to selectively detect tumor angiogenesis and an untargeted Cy5.5 to image lymphatics. After acquiring the experimental data, fluorescence image-guided surgery was performed.

Dynamic, multi-wavelength fluorescence imaging was accomplished using a liquid crystal tunable filter (LCTF). Excitation light was used for reflectance images with a LCTF transmitting a shorter wavelength than the peak in the excitation light spectrum. Therefore, images can be dynamically acquired alternating frame by frame between emission and excitation light, which should enable image-guided surgery.

DEDICATION

To my wife, Sorin,

for always being by my side.

ACKNOWLEDGMENTS

The work presented here would not have been possible without the support and guidance I received from many people. *ACKNOWLEDGEMENT* is very small word that does not adequately thank everyone whose efforts helped with the completion of this dissertation.

First, I would like to thank and acknowledge my advisor, Dr. Eva M. Sevick-Muraca, who shared with me her knowledge and taught me the skills I needed to become a successful researcher. Even before joining Photon Migration Laboratories (PML) at TAMU, when I went through difficult times, her support and encouragement inspired me to continue my academic career. She helped me to develop as an engineer and a scientist in new interdisciplinary research field, and to complete this dissertation.

I would also like to thank Dr. Shi Ke and Dr. Wei Wang. Without their help with animal handling and development of imaging agents at M.D. Anderson Cancer Center and Baylor College of Medicine, I would not have been able to finish this dissertation. I would also like to acknowledge my committee members, Dr. Daniel F. Shantz, Dr. Gerard L. Cote, and Dr. Eric E. Simanek, who not only took the time to serve on this committee but also provided advice and guidance throughout this process.

My former and present PML colleagues, Drs. Jessica P. Houston, John Rasmussen, and Kristen E. Adams have become good friends, collaborated on many projects, and provided assistance with data presentation and analysis. Also, I would like to acknowledge other colleagues at PML, who advised me: Drs. Amit Joshi, Sarabjyot Dali, Tianshu Pan, Feng Liang, Kildong Hwang, and Amit Sahu.

Without my family I would not be where I am today, they have always supported and encouraged me. For me, this accomplishment is shared with my parents, sisters and wife, as it would not have been possible without them. I am grateful to my parents, who inspired and motivated me throughout my life to achieve my goals and become the scientist I am today. My sisters were my first and best friends, always there helping me to succeed, and encouraging me to learn about and experience new things. Finally, I would like to thank my wife, Sorin Kwak. She was my inspiration, moral support, and friend throughout my years of research, and she kept me focused and working towards the completion of this dissertation. Without her loving support, understanding, and friendship, I could not have completed this work. She will always have my deepest gratitude and love.

NOMENCLATURE

Abbreviation

1-D	one dimensional
3-D	three-dimensional
a.u.	arbitrary unit
BBB-D	disruption of the blood-brain barrier
CCD	charge-coupled device
CEU	contrast-enhanced ultrasound
CT	computed tomography
CW	continuous wave
CYT-103	B72.3-glycyl-tyrosyl N—dimethylenetriaminepenta-acetic acid
Cy	cyanine
EGF	epidermal growth factor
EGFR	epidermal growth factor receptor
EPR	enhanced permeability and retention
ECM	extracellular matrix
EMCCD	electron multiplication charge-coupled device
EGFR	epidermal growth factor receptor
FBP	filtered back projection
FDG	2-fluoro-2-deoxy-D-glucose
FDPM	frequency domain photon migration
FGF	fibroblast growth factor
Gd	gadolinium
ICCD	intensifier charge-coupled device
ICG	indocyanine green
i.d.	intradermal
i.v .	intravenous
LCTF	liquid crystal tunable filter
MAb	monoclonal antibody
MAP	maximum a posteriori
MRI	magnetic resonance imaging
MVD	microvessel density
NIR	near-infrared
OD	optical density
OSEM	ordered-subset expectation maximization
PEG	polyethylene glycol
PET	positron emission tomography
PK	pharmacokinetic
PLAP	placental alkaline phosphatase
R	transmission ratio
ROI	region of interest
ROIs	regions of interest

RGD	arginine-glycine-aspartic
$S(\lambda_m)$	mean fluorescence intensity values associated with the measurements taken in the presence of dye in the solution
$S(\lambda_x)$	mean fluorescence intensity values associated with the measurements taken in the absence of dye in the solution
SNR	signal to noise ratio
SPECT	single photon emission computed tomography
SUV	standard uptake values
SLN	sentinel lymph node
TK	tyrosine kinase
TBR	target to background ratio

Symbols

α	pharmacokinetic parameter
β	pharmacokinetic parameter
$C_{BOUND}(t)$	concentration of dye bound to integrin receptor either in the vascular or extravascular compartments
$C_{EXTRAVASCULAR}(t)$	concentration of dye in extravascular space
$C_{VASCULAR}(t)$	concentration of dye in vascular space
I_0	background fluorescence intensity
k_c	rate constant for distribution of dye from vascular or extravascular to bound compartment
k_p	rate constant for distribution of dye from vascular to extravascular space
k_{el}	rate constant for elimination
k_r	reflux rate constant for distribution of dye from extravascular to vascular space
w_i	weight function
t	time

TABLE OF CONTENTS

Page

Page

LIST OF FIGURES

Page

Page

Page

Page

Page

LIST OF TABLES

1. INTRODUCTION

Cancer is typically detected and diagnosed through anatomical imaging and then subsequent tissue biopsy. However, tissue biopsy is prone to sampling error and lesions of finite volume, thereby providing diagnosis of late rather than early stage disease. As a result, recent research has focused on molecular imaging, which can be defined as the imaging of biological processes at cellular and molecular levels *in vivo*. Since molecular changes precede anatomical changes, molecular imaging may provide diagnostic information enabling earlier intervention and greater therapeutic efficacy. Molecular imaging promises to avoid sampling error and provides diagnosis based upon the entire diseased site.

Molecular imaging has been recently garnered attention due to the advances in imaging modalities for image acquisition, molecular biology, and novel molecular probes. For successful molecular imaging, the important elements are: (1) highly specific molecular probes to monitor molecular interactions and (2) imaging systems with high sensitivity to reporters found at very low concentrations *in vivo*. The non-invasive imaging modalities include magnetic resonance imaging (MRI), X-ray computed tomography (CT), positron emission tomography (PET), single photon emission computed tomography (SPECT), ultrasound, and optical imaging and have varying sensitivities to the reporters. These imaging modalities depend upon energy-tissue interaction or the administration of imaging probes as presented in Table 1.1.

This dissertation follows the style of *Journal of Molecular Imaging*.

As shown in Table 1.1, MRI and CT imaging system require a substantial amount of contrast agents to generate sufficient signal in small animal imaging as well as clinical imaging. In addition, CT provides anatomical imaging, which does not have functional information at a molecular level. Among these modalities, nuclear medicine is the "gold-standard" for molecular imaging of cancer. While nuclear imaging is non-invasive, provides functional information, and requires small amounts of the contrast agents as described in Table 1.1, it has several limitations. Nuclear imaging requires radioactive contrast agents, which are potentially hazardous especially with repeated use. Nuclear techniques suffer from limited resolution as well as poor signal to noise (SNR) and tumor to background ratio (TBR) when compared with small animal optical imaging techniques [7]. In addition, most standard nuclear imaging studies report static images, which include information about tracer distribution and receptor densities. Although dynamic nuclear imaging is possible, it requires substantial amounts of contrast agent and long integration times.

Of the previously discussed imaging modalities, optical imaging techniques are developing rapidly for use in medicine, because of their sensitivity and use of non-ionizing radiation. This technique requires molecularly targeted fluorescent contrast agents, since intrinsic contrast in cancerous regions is non-existent or insufficient for detection of early metastatic lesions.

Table 1.1 Comparison of current molecular imaging modality.

Imaging modality	Depth / resolution	What is measured	Molecular contrast agents
X-ray, CT	No apparent limit / 50 μm	Attenuation owing to endogenous or exogenous compounds	Iodinated compound (mM)
MRI	No apparent limit / <100 μm	Relaxation of spin-spin states of endogenous or exogenous paramagnetic compounds	Lanthanide chelates, Gadolinium, dysprosium (mM), ultrasmall iron oxide particles (nM)
Ultrasound	mm / 50 μm	Reflection of sound waves from endogenous or exogenous compound that produce acoustic mismatches	Liposomes, microbubbles (mM)
PET	No apparent limit / <1~2 mm	Beta emission from the annihilation of exogenous radiotracers	^{13}N, ^{11}C, ^{18}F, ^{94m}Tc, ^{124}I (pM ~ nM)
SPECT	No apparent limit / <1~2 mm	Gamma emission from the annihilation of exogenous radiotracers	^{99m}Tc, ^{111}In, ^{123}I, ^{125}I (pM ~ nM)
Optical imaging Endogenous (mM) Fluorescence (pM-nM)	cm / mm	Attenuation owing to absorbance due to oxy- and deoxy- hemoglobin and production of fluorescence/luminescence from exogenous agents, gene reporters (GFP, RFP), and bioluminescence (Luciferin)	Fluorophores (pM ~ nM) Chromophores (mM)

Fluorescent contrast agents can be specifically targeted to disease markers within cancer, such as those present on the neovasculature, cancer cell surface, or both. Therefore, fluorescence imaging techniques may be used as a diagnostic tool for finding precancerous or malignant lesions and assessing tumor response. Imaging tumor response to therapy may lead to tailored therapies and increased treatment efficacy. In addition, fluorescence imaging may serve as a surgical tool for resection of lymph nodes or tumor margins.

This thesis reports work toward developing a dynamic, continuous-wave (CW) fluorescence-enhanced optical imaging system, which is designed to evaluate the efficacy of novel targeted fluorescent contrast agents for *in vivo* small animal imaging and ultimately for clinical imaging. Fluorescence-enhanced imaging with disease-specific or nonspecific contrast agents is in the early stages of clinical translation. Our current studies have emphasized the promising aspects of fluorescence-enhanced imaging techniques. In order to develop dynamic optical imaging for diagnosing cancer and for assessing therapeutic efficacy of molecular medicines targeting disease markers, a better understanding of the information contained in molecular dynamic optical imaging must be obtained from pre-clinical, small animal imaging. In this work, the integrin receptor overexpressed on tumors and on proliferating endothelium is focused upon. Section 2 provides a biological background on $\alpha v\beta 3$ integrins, especially their role in tumor angiogenesis. In addition, the various molecular imaging modalities which use $\alpha v\beta 3$ targeting are outlined. Section 3 details the instrumentation involved in dynamic

fluorescence imaging used to acquire the pharmacokinetic (PK) data reported in the subsequent Sections.

Section 4 is the first Section that describes the experimental work of this thesis research. For molecular diagnostics and therapeutics, it is important to know the optimal dose of the agent. Too much agent could cause receptor oversaturation and expose the patient to excess amounts, while too little could cause weak signals and lead to poor diagnostic efficacy. The optimal dose of a diagnostic agent may also provide information about the optimal dose of molecular therapeutic agents for individualized therapies. Section 4 summaries experimental studies using a three-compartmental PK analysis of dynamic *in vivo* fluorescence data to assess dose-dependent uptake of an integrin targeted fluorescent contrast agent following intravenous (i.v.) injection to animals bearing tumors. Dynamic imaging has the potential to improve delineation between normal and disease tissues and to detect transient alterations in tumor physiology resulting from cancer treatment. In addition, real-time dynamic imaging might help screen drugs and optimize treatment procedures. For example, the action of integrin based therapies differ depending upon the location of the integrin receptor, i.e., anti-angiogenesis in the vascular space or direct cytotoxicity to cancer cells in the extravascular space.

Expanded studies of PK models are presented in Section 5, where pharmacokinetic models to enable the assessment of disease marker availability in potentially different tissue compartments are discussed. Two three-compartmental PK models are used to evaluate the uptake rate of an integrin-targeted fluorescent contrast agent in two different xenograft tumor models.

Real-time dynamic whole-body imaging might also be able to monitor circulation of the agents through the animal due to its high sensitivity and sub-second camera exposure time. However, the sensitivity of dynamic fluorescence-enhanced imaging can deteriorate dramatically owing to inefficient rejection of backscattered excitation light [8] and the presence of tissue autofluorescence. Section 6 presents experimental work investigating the impact of autofluorescence in dynamic fluorescence imaging of the epidermal growth factor receptor (EGFR) with NIR and red light excitable fluorescent contrast agents.

Section 7 presents dual-wavelength fluorescence imaging: specific targeting NIR fluorescent conjugates to detect tumor angiogenesis and non-specific red light excitable fluorescent dye to detect lymphangiogenesis. In addition, fluorescence image-guided lymphadectomy was described.

Section 8 presents improved fluorescence whole-body small animal imaging by extending dynamic fluorescent imaging to rapid multi-wavelength imaging. Using a liquid crystal tunable filter (LCTF) we monitored multiple fluorescent dyes on different conjugates, targeting different tissue compartments all in near rear time with a single camera system.

Figure 1.1 provides the organization of this dissertation. When combined with highly specific molecular probes, sensitive imaging systems, and quantitative analysis methods for fluorescence data, dynamic fluorescence-enhanced imaging could provide the preclinical validation necessary to translate dynamic, fluorescent optical imaging technology into human clinical trials using molecularly targeting agents.

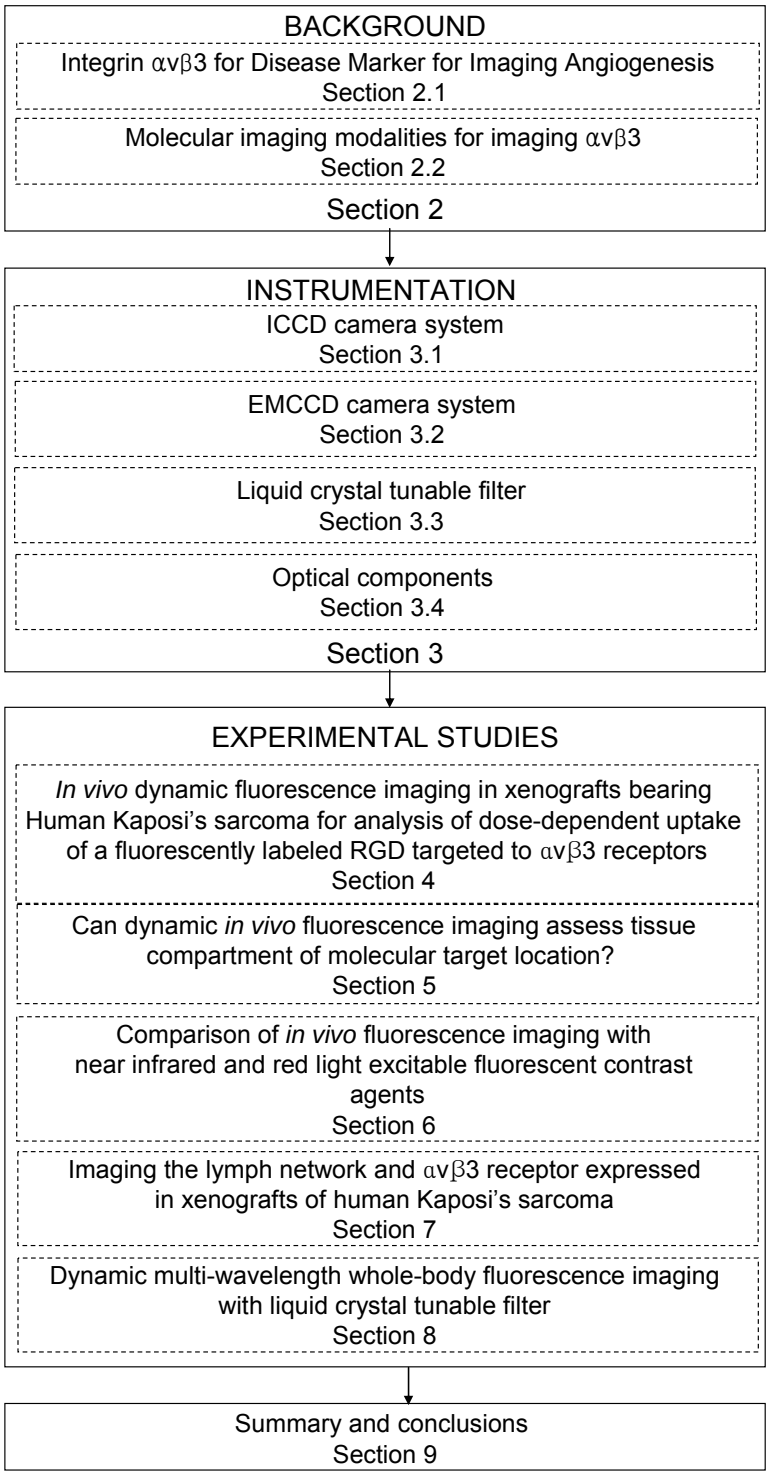

Figure 1.1 Organization of dissertation

2. BACKGROUND: DIAGNOSTIC IMAGING OF INTEGRIN αvβ3

2.1 Integrin αvβ3 for Disease Marker for Imaging Angiogenesis

Integrins are a large family of transmembrane glycoproteins consisting of two subunits, α and β [9]. There are at least 24 distinct integrin heterodimers comprised of 18 known α subunits and 8 β subunits. Each subunit in an integrin receptor consists of a large extracellular domain, a single membrane spanning domain and usually a short cytoplasmic domain [10]. Integrins mediate cell to cell and cell to extracellular matrix (ECM) adhesion by binding to an arginine-glycine-aspartic (RGD) peptide sequence or a non-RGD sequence [11, 12]. Integrin binding to ECM molecules transmits signals from inside the cell to the ECM (inside-out signaling) to regulate the affinity and conformation of the receptor. Integrin binding also transmits signals from the ECM into the cell (outside-in signaling) to trigger the intracellular events mediated by receptor-ligand binding, which can induce changes in gene expression, leading to events such as stimulation of cell proliferation or apoptosis [9, 11]. The role of integrins in cancer growth is very complex and can differ among cancer types [11]. Integrin expression or function can even be different between the primary tumor and its metastases [13, 14]. In cancer growth, integrin expression can change during cancer progression from overexpression to no expression or the reverse [15].

One of the integrins, αvβ3 is expressed at low levels in most normal tissues including intestinal, vascular, and smooth muscle cells, but, is highly expressed in mature, bone resorbing osteoclasts, activated macrophages, angiogenic endothelial cells, and migrating smooth muscle cells. These cell types clearly reflect the involvement of

integrin αvβ3 in bone resorption, neovascularisation, and inflammation (Figure 2.1). Moreover, integrin αvβ3 is also expressed in several invasive tumor types including melanoma [16], glioma, ovarian, and breast cancer [17]. Therefore, integrin αvβ3 is an ideal target for diagnosing disease as well as for tracking the therapeutic efficacy. It has been shown that antagonists of αvβ3, such as peptides and anti-integrin antibodies, induce tumor regression and disrupt newly formed vasculature generated by growth factors and tumor fragments, but pre-existing quiescent blood vessels remain unaffected [18-20].

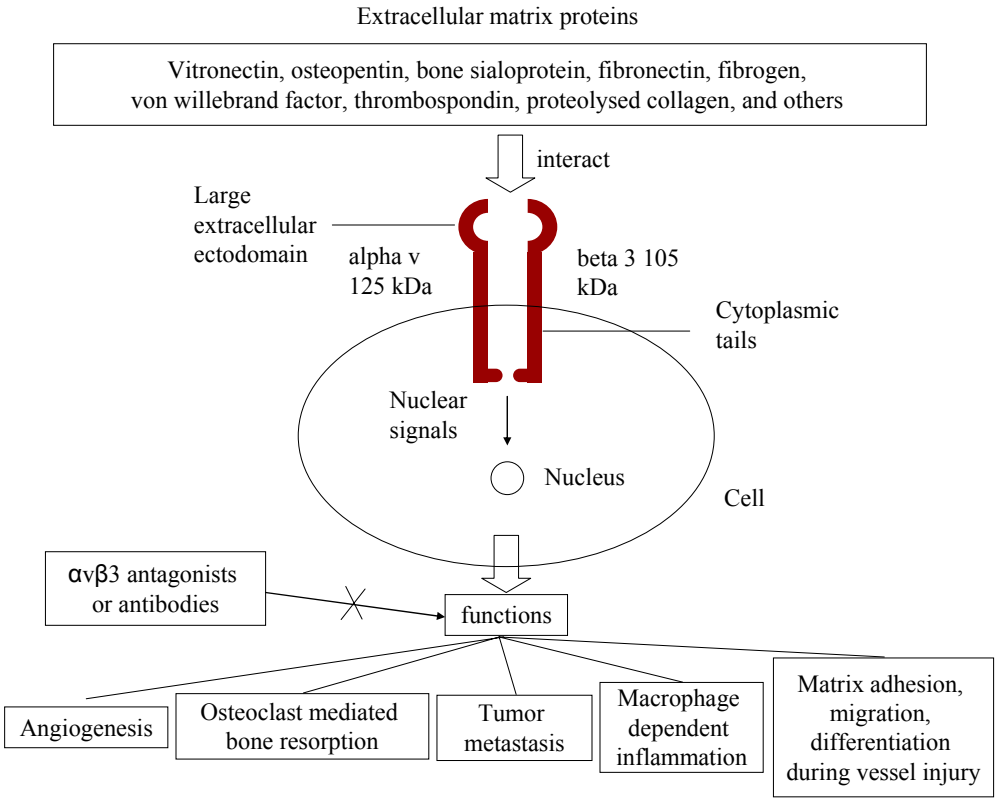

Figure 2.1 Schematic of the role of αvβ3 receptors with interaction of ECM molecules. Reproduced from [1].

Knockout mice have been used to determine the role of integrin αvβ3. Although knocking out αv or β3 integrin led to developmental abnormalities and defects, neither was lethal [21-23]. Additionally, these mice as well as those lacking β5 integrins supported developmental angiogenesis [21, 22]. More interestingly, mice lacking β3 integrins or both β3 and β5 integrins showed enhanced pathological tumor angiogenesis [24]. This result is contrary to the previous findings from extensive studies on tumor growth using integrin antagonists. One possible explanation is that when bound to the ECM, integrins trigger survival signals. Whereas in the absence of ECM binding, or in the presence of endogenous or therapeutic antagonists, the integrins activate a death pathway, 'integrin-mediated death,' leading to cell death and suppression of angiogenesis. Absence of αvβ3 leads to loss of the ability to sense ECM and to trigger endothelial cell apoptosis through this pathway, resulting in increased pathological angiogenesis [25].

2.2 Molecular Imaging Modalities for Imaging αvβ3

Although most of the experimental data presented in this dissertation was obtained using an optical imaging system to dynamically image integrin αvβ3, it is appropriate to discuss briefly the other modalities used for imaging integrin αvβ3. The following section contains a description of how the instrumentation works and which contrast agents and imaging modalities are used to image integrin αvβ3.

2.2.1 Computed Tomography

Computed tomography (CT) is a imaging method employing tomography. A schematic of the x-ray CT technique is provided in Figure 2.2. In MicroCAT™ II, which is present at the Baylor College of Medicine (BCM) Frensley Center for Imaging Research, a rotating frame has an x-ray tube mounted on one side and the detector on the opposite side. The frame spins the x-ray tube and detector around the object, taking a large series of 2-D x-ray images around a single axis of rotation. Each profile is then backwards reconstructed by a dedicated computer. When x-rays pass through the body they are absorbed or attenuated at different tissues due to their thickness and densities.

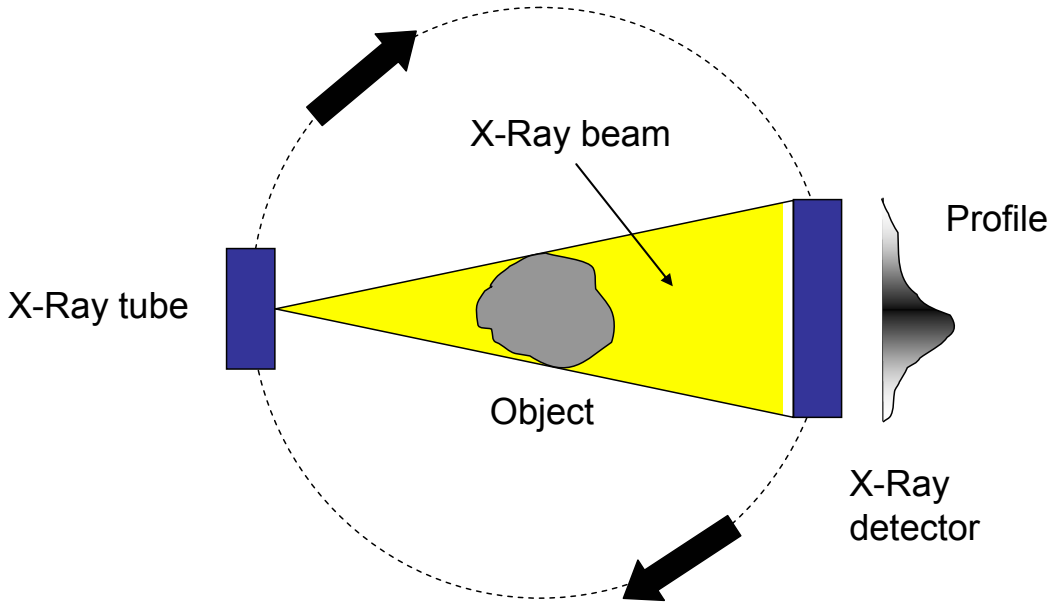

Figure 2.2 Schematic of CT imaging technique. As x-ray tube and detector rotate around the object, a series of 2-D x-ray images are taken.

These intrinsic tissue differences, such as bone and fat provide the contrast of anatomical structures with high resolution (Figure 2.3 (a) and (b)). However, CT has relatively poor soft-tissue contrast and can generally not differentiate between tumors and surrounding soft-tissue. Although high concentrations of CT contrast agents can be used to overcome the sensitivity limitation of CT, they can result in toxicity, limiting repeated CT scanning. Nonetheless, the use of contrast agents, such as those for the liver and vasculature, is useful to highlight structures that otherwise would be difficult to delineate from their surroundings. Moreover, the visualization software, AMIRA (version 3.1, Konrad-Zuse-Zentrum fur Informationstechnik Berlin, Germany) can interactively segment different organs or tissue types from the 3D image data after administration of contrast agents as shown in Figure 2.3 (c).

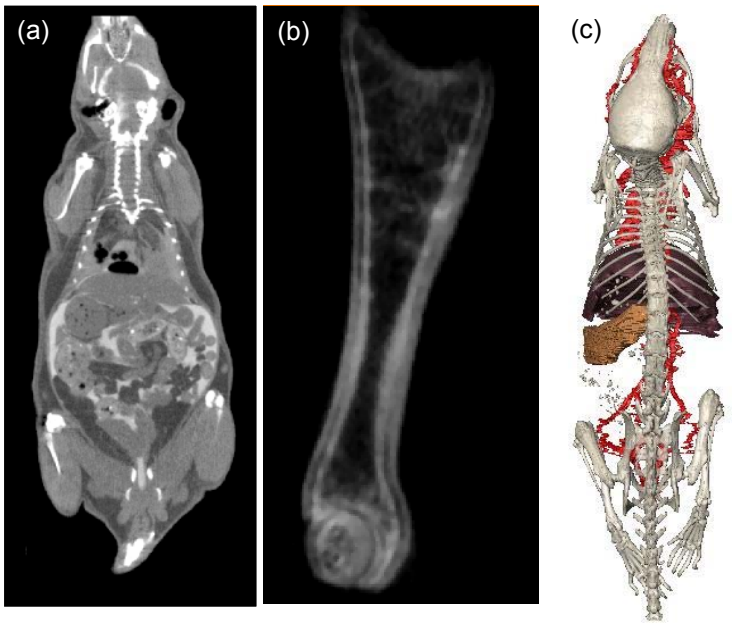

Figure 2.3 CT anatomical (a) whole body image, (b) trabecular bone image, and (c) reconstructed image after segmentation from an animal injection with CT liver and vasculature contrast agents.

2.2.2 Magnetic Resonance Imaging

In magnetic resonance imaging (MRI), the nuclei of hydrogen act like small spinning bar magnets. An external magnetic field excites a number of protons in the nuclei of hydrogen causing them to align. The difference between the number of protons in the nuclei of hydrogen in the presence and the absence of the magnetic field results in a net magnetization in the nucleus of the atoms. The net magnetization causes the atoms to rotate about the axis of the applied electromagnetic field. When perturbing the magnetic alignment using a radio frequency (RF) pulse, the nuclei of the atoms rotate in phase and return to their original positions, emitting RF signals, which can be detected by gradient coils placed around the object (Figure 2.4).

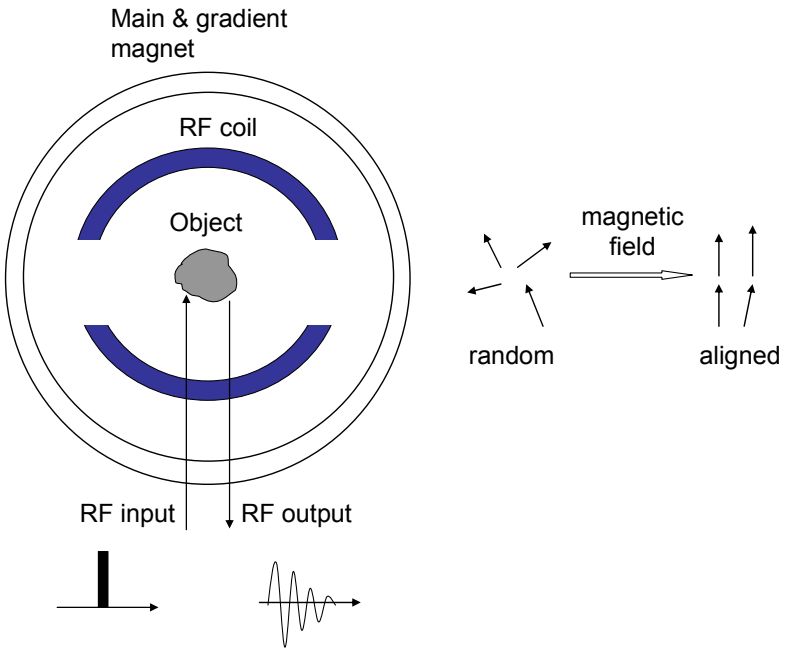

Figure 2.4 Schematic of MRI technique. Right figure shows that external magnetic field aligns protons. When perturbing alignment by a radio frequency (RF) pulse, the nucleus of the atoms rotates in phase and returns to their original position, emitting RF signal.

Magnetic resonance (MR) signal depends on the proton density as well as on the temporal T1 and T2 relaxation times. T1 is the time when nuclei placed in the magnetic field return to the axis of the original field. T2 describes the rate of MR signal decay, since there are variations in local magnetic field during the signal fade. Since T1 relaxation times differ among body tissues, T1 images usually provides anatomical details, including differentiation of diseased or abnormal tissue from normal tissue. T2 relaxation times also vary in different tissue types. Most pathological processes increase T2 relaxation times, producing a higher signal than the surrounding normal tissue on T2-weighted scans.

Gadolinium (Gd) has been used a successful contrast agent for molecular imaging applications. The Gd chelates are diffusible and serve as markers for detecting tumor angiogenesis due to high permeability in tumor region, allowing differentiation between normal tissue and malignant tumors. In addition, its high resolution enables MRI to detect tumors that are not visible through x-ray mammography. Recently, paramagnetic nanoparticles have been conjugated with antibodies [26, 27] or peptide/peptidomimectic integrin αvβ3 antagonist [28, 29] for imaging of integrin αvβ3 expressed in neovascular endothelium. Sipkins *et al.* first demonstrated MRI imaging of integrin αvβ3 expressed in tumor neovasculature using an antibody against αvβ3, LM 609 conjugated with paramagnetic liposomes (300-350 nm in diameter) [26]. Immunohistochemical staining confirmed MRI imaging of the integrin on vascular endothelium. Anderson *et al.* used Gd-perfluorocarbon nanoparticles conjugated to another αvβ3 antibody DM101 (400-700 nm in diameter) [27]. In their study, neovasculature induced by bFGF was imaged, and

the MR signal intensity increased 25 % at 4 hrs after injection of the agent. An atherosclerosis model was also used to image the integrins with a peptidomimetic integrin αvβ3 antagonist conjugated to magnetic nanoparticles [28]. In addition, integrin αvβ3 induced by nascent human melanoma xenografts was detected using targeted paramagnetic nanoparticles [29]. Imaging was conducted 12 days after inoculation of melanoma cells. Although MRI has higher spatial resolution as described in Table 1.1, MRI is less sensitive. Therefore, the large amounts of contrast agent, which can be toxic, are generally required for obtaining an enhanced contrast. In addition, contrast agents remain in the blood circulation for a long time and may have difficulty penetrating tumors due to the large particle size.

2.2.3 Radionuclide-based Imaging

Radionuclide based imaging, i.e. nuclear imaging detects emitted gamma rays from tissues injected with radioisotopes. There are two types of nuclear imaging techniques; single photon emission computed tomography (SPECT) and positron emission tomography (PET).

SPECT is a nuclear medicine tomographic imaging technique using gamma rays. A schematic of SPECT imaging technique is given in Figure 2.5. Gamma rays are electromagnetic radiation emitted during radioactive decay which has an extremely short wavelength. The radioactive isotope decays and emits gamma rays that can be detected by the SPECT detectors.

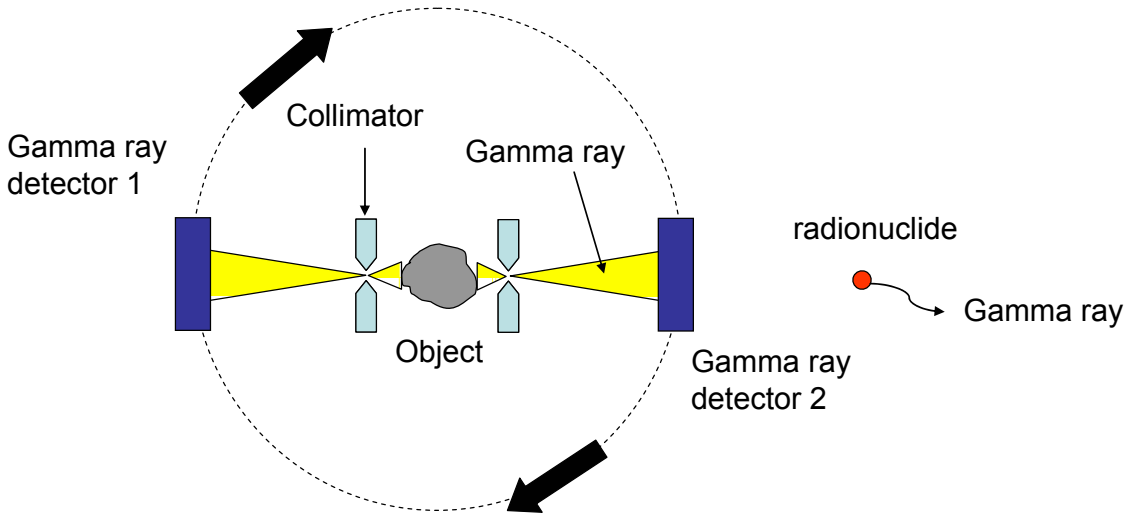

Figure 2.5 Schematic of SPECT imaging technique. Two SPECT detectors rotate around an object and detect gamma rays emitted from radionuclides within the object.

The radionuclides used in SPECT are gamma emitters with relatively long half-lives (Table 2.1). In the MicroCAT II, two SPECT detectors rotate around an object (usually 360 degrees around an animal), creating a series of 2-D images. For each image, only photons moving perpendicular to the camera face are allowed to pass through the collimator.

Table 2.1 Emission energy window and half-life of Radioisotopes frequently used for SPECT.

Radioisotope	Emission energy (keV)	Half-life
Technetium-99m	140	6 hours
Iodine-123	159	13 hours
Iodine-125	27-33	59 days
Indium-111	171& 245	3 days

The collimator is a pattern of holes through the gamma ray absorbing material (tungsten) that projects the gamma ray image onto the detector crystal. These photons originate from various depths in the animal, resulting in overlapping of all tracer emitting organs along the specific path. In addition, a multi-head SPECT file which contains data from two SPECT files, one from detector # 1 and the other from detector # 2 can be merged into a single SPECT data file, resulting in reduced acquisition time and increased sensitivity. Furthermore, different isotopes which emit different energies can be simultaneously used to image different tissue compartments. The functional SPECT images are collected with anatomical microCT images for enhanced analysis. Figure 2.6 shows a fused image of reconstructed SPECT and CT images in an animal injected with a bone targeting agent, Technescan.

Figure 2.6 Fused image of reconstructed SPECT and CT images in an animal injected with bone targeting agent, Technescan.

PET uses a short-lived radioactive tracer which decays by emitting a positron (Table 2.2). The positrons travel a short distance in the object before striking a nearby electron. When this collision occurs, two gamma rays are simultaneously produced and travel away from each other at a 180 degree angle, toward the ring of photon detectors. Each time two detectors detect a gamma ray simultaneously, the annihilation event is recorded. A schematic of PET imaging is given in Figure 2.7.

With computer controlled vertical and horizontal bed motion, microPET® can perform whole body biodistribution or gated imaging with continuous bed motion acquisition. Continuous bed motion acquisitions also afford a higher resolution image for static imaging due to over sampling effect caused by the motion. Raw images can be reconstructed with several kinds of algorithms, such as 2-D ordered-subset expectation maximization (OSEM), 3-D OSEM, 2-D filtered back projection (FBP), 3-D maximum a posteriori (MAP). AMIRA also enables fusion of anatomical CT image and functional PET image for enhanced analysis. Figure 2.8 shows a fused image of reconstructed PET and CT images in a human breast cancer (MDA-MB-231) xenograft tumor bearing mouse injected with ^{18}F-FDG.

Table 2.2 Half-life of Radioisotopes frequently used for PET.

Isotope	Half-life
Fluorine-18	110 minutes
Carbon-11	20 minutes
Oxegen-15	2 minutes
Iodine-124	100 hours
Copper-64	13 hours

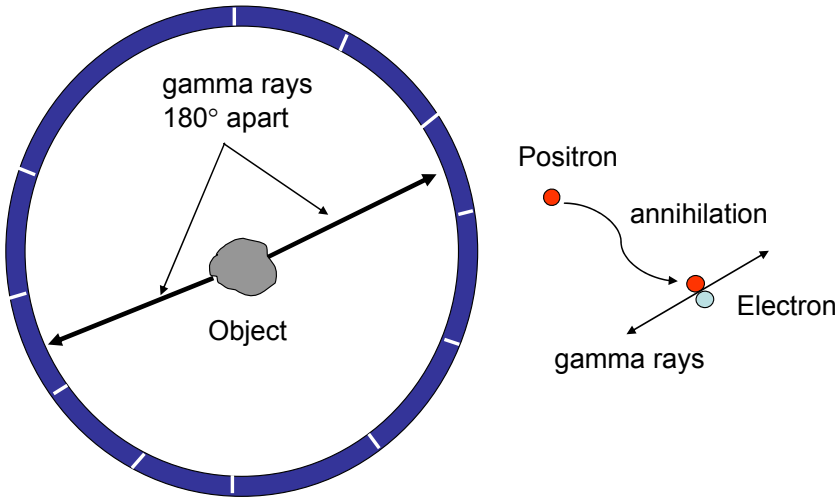

Figure 2.7 Schematic of PET imaging technique. PET detects two gamma rays 180 degrees apart after positrons emitted from the object collide with nearby electrons.

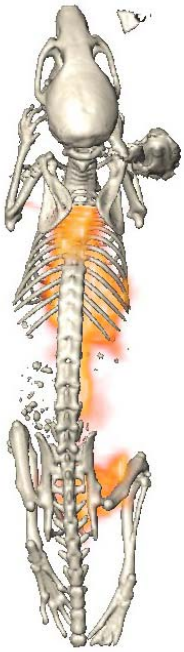

Figure 2.8 Fused image of reconstructed PET and CT images in a human breast cancer (MDA-MB-231) xenograft tumor bearing mouse injected with ^{18}F-FDG.

To date, most RGD-based imaging of integrin αvβ3 has been performed using nuclear imaging, the "gold-standard" of molecular imaging (Table 2.3). In SPECT imaging, Jenssen *et al.* [30] used a dimeric RGD peptide E-[c(RGDfK)]$_2$ labeled with ^{111}In, ^{99m}Tc, and ^{90}Y in ovarian carcinoma xenografts. They demonstrated highly specific tumor uptake of ^{111}In-DOTA-E-[c(RGDfK)]$_2$ and ^{99m}Tc-HYNIC-E-[c(RGDfK)]$_2$ in human tumor xenografts. In addition, they showed ^{90}Y-DOTA-E-[c(RGDfK)]$_2$ induced a significant regression in tumor growth. ^{111}In-RP748, a quinolone* that binds to integrin αvβ3, was used to image injury-induced vascular proliferation [31]. In addition, Meoli *et al.* [32] used a dual isotope probe with two different energies to image ischemia-induced angiogenesis and perfusion. Furthermore, αP2, a synthesized decapeptide that contains two RGD sequences in its structure was labeled with ^{99m}Tc to image metastatic tumors in human melanoma patients [33, 34]. One patient with αvβ3 positive melanoma showed imaging of tumor sites, while imaging of patients with other metastatic tumors was not successful. In these studies, there was no significant toxicity or immune response to the high doses.

PET has been used extensively for αvβ3 imaging, because of its high sensitivity and lack of depth limitations (Table 1.1). A variety of different radiolabeled RGD-peptides have been developed for non-invasive imaging of integrin αvβ3 expression, including peptides labeled with minimum structural alteration, peptide carbohydrate conjugates, peptidomimetics based on the RGD-structures, and heterodimeric, homodimeric and homotetrameric ligand systems [35]. These peptides were mostly

* quinolone: a family of an antibiotic with activity against a wide range of disease-causing bacteria

labeled with ^{18}F and ^{64}Cu for imaging in human xenografts or mouse tumor models (Table 2.3). Haubner *et al.* [16] reported for the first time noninvasive PET imaging of integrin αvβ3 expression using [^{18}F]Galacto-RGD in cancer patients. A patient with malignant melanoma stage IIIb and a solitary lymph node metastasis in the right axilla showed high uptake of both [^{18}F]FDG and [^{18}F]Galacto-RGD. Another patient with a soft tissue sarcoma dorsal of the right knee joint showed circular peripheral tracer uptake in the tumor with variable intensity and a maximum after injection of [^{18}F]Galacto-RGD. Although multiple metastases in liver, skin, and lower abdomen in a patient with malignant melanoma stage IV were shown with marked uptake of [^{18}F]FDG in the lesions, there was no uptake of [^{18}F]Galacto-RGD in the metastatic lesions.

2.2.4 Ultrasound Imaging

Ultrasound imaging is based on detecting reflected and transmitted sound waves from tissue in response to high frequency sound emitted from a transducer. The transducer detects sound waves as they bounce off from internal structures and contours (Figure 2.9). Different tissues reflect these sound waves differently, causing a signature which can be measured and transformed into an image. Ultrasound is commonly used due to its low cost, portability, millimeter-range resolution, and non-ionizing radiation. Ellegala *et al.* [36] demonstrated that tumor angiogenesis can be assessed through contrast-enhanced ultrasound (CEU) imaging with microbubbles (3-4 μm in diameter) targeting integrins.

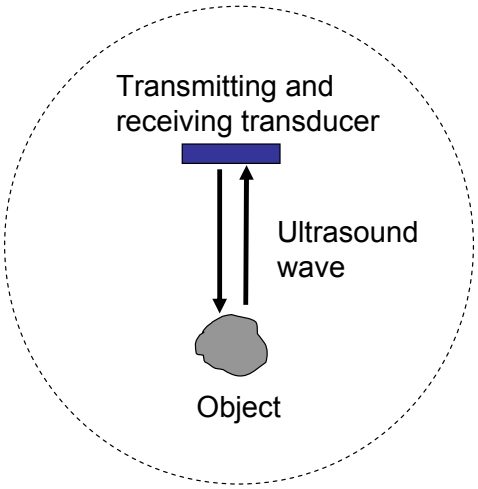

Figure 2.9 Schematic of ultrasound imaging technique. In ultrasound imaging transducer detects sound waves bouncing off an object.

The microbubbles were conjugated to an echistatin peptide bearing a RGD motif. The CEU signal was shown to be higher at the periphery of human glioma tumor (U87MG), where integrins are prominent as confirmed by immunohistochemistry. In addition, the results from the CEU signal correlated well with the tumor microvessel blood volume. Leong-Poi *et al.* [37] reported microbubbles conjugated to echistatin or a monoclonal antibody (MAb) targeted to αv integrin in mice after 4 days of sustained-release of fibroblast growth factor (FGF)-2. Intravital microscopy confirmed the binding of microbubbles to endothelium. The same group also assessed endogenous angiogenic responses to ischemia and proangiogenic responses to growth factor therapy [38]. Recently, when the microbubbles were conjugated with the tumor endothelial-specific binding tripeptide arginine-arginine-leucine (RRL) [39], they selectively bound to tumor-derived endothelium. Ultrasonic molecular imaging of angiogenesis may allow

functional assessment of neovasculature as well as monitoring of tumor response to antiangiogenic therapies.

2.2.5 Optical-based Imaging

Optical imaging is based on launching light onto a tissue surface and detecting the scattered and attenuated light. A schematic representation of optical imaging is shown in Figure 2.10. Many endogenous light absorbing molecules are present in biological tissue. The absorbance spectra for some of them, oxy- and deoxyhemoglobin, melanin, and water, are shown in Figure 2.11. Although the normal tissues can be differentiated from the diseased tissues based upon endogenous contrast in the optical properties such as absorption and scattering coefficient, it can be difficult to detect small tumors at early stages.

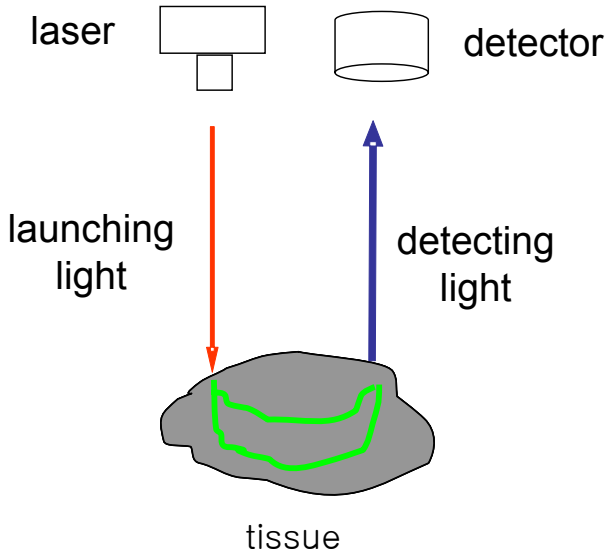

Figure 2.10 Schematic of optical imaging. Optical imaging launches incident light on the surface of an object and detects the scattered and attenuated light.

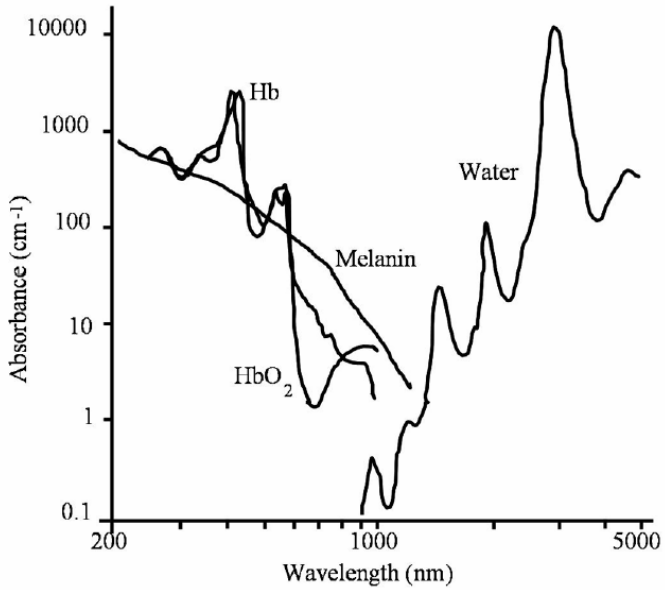

Figure 2.11 Biological absorbance spectra. Reproduced from Lin and Soter [2].

Fluorescent contrast agents have been developed to improve early detection of diseased tissues. Fluorescence refers to the process by which certain molecules absorb energy from light at a particular wavelength and re-emit light of a lower energy and longer wavelength. As shown in Figure 2.12, when light of a specific energy ($h\nu_1$) encounters a molecule residing at equilibrium in a ground state S0, the electrons are excited to a higher electronic level (S1). Fluorescence, i.e. photon emission, is generated by the relaxation of these electrons back to their ground state, releasing the energy ($h\nu_2$).

We and others (Table 2.3) have shown fluorescence imaging of αvβ3 expressed on tumors. Fluorescence dyes were conjugated to RGD peptides to specifically target αvβ3.

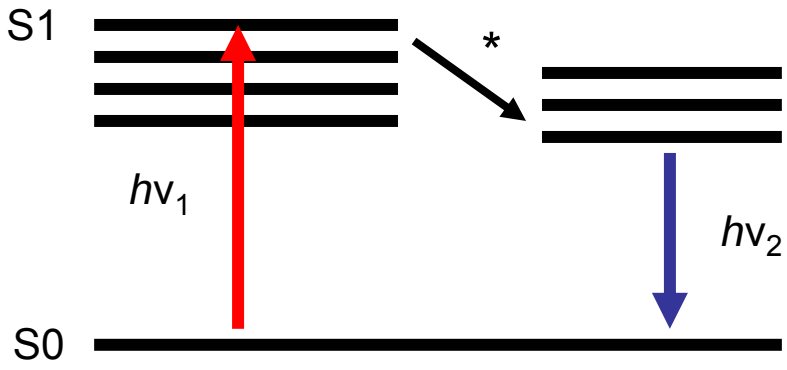

Figure 2.12 Simplified Jablonski diagram of fluorescence where * represents partial dissipation of absorbed energy. Reproduced from Lakowicz and Harris [3].

Chen *et al.* [40] used TBR to show the specificity of Cy5.5-c(RGDyK) in subcutaneous U87MG glioblastoma tumor model and reported no correlation between changes in TBR and dose. Subsequently, they showed the effect of the multimers of the RGD peptide labeled with Cy5.5 or Cy7 [41, 42]. Their results showed moderate improvement in imaging characteristics with the tetramer, as compared to the monomer and dimer. Wang *et al.* [43] showed dynamic fluorescence imaging of human Kaposi's sarcoma (KS1767) xenografts with Cy5.5- and IRDye800-c(KRGDf). Recently, the dynamic fluorescence intensity as a function of the time was analyzed with a pharmacokinetic model [8, 44]. Our work presented in Section 4 showed that the uptake of Cy5.5-c(KRGDf) in tumor regions was linearly related to the dose, up to 1.5 nmol/mouse. Above doses of 1.5 nmol / mouse, the uptake no longer increased with dose, suggesting receptor saturation [8]. In a recent analysis of nuclear and NIR optical imaging in which mice bearing human melanoma tumors were injected with a dual-labeled RGD imaging agent, Houston *et al.* [7] has shown that fluorescence imaging has

significantly higher signal for a given dose of agents, enabling rapid dynamic imaging and sensitive detection of diseased regions. Radionuclide imaging generates a maximum of 10^8 events/sec upon injecting milli-curie amounts of radionuclides. In contrast, fluorescence-enhanced optical imaging can generate almost ~ 10^{23} events/sec even using nanomolar concentrations of the fluorescent agents because they exhibit a fluorescence lifetime on the order of nanosecond. In addition, Houston *et al.* [45] highlighted the sensitivity of contrast-enhanced optical imaging. They were able to detect a signal of 100 fmol of the contrast agent located 4 cm below the surface. Thus, the contrast-enhanced optical imaging has the potential to compete with clinically available radionuclide imaging techniques. Because it is an inexpensive, rapid, non-ionizing alternative with higher target to background ratio (TBR) to current methods contrast enhanced optical imaging should improve upon the currently available imaging modalities.

Table 2.3 Targeting αvβ3 using the RGD peptide motif with molecular imaging modalities.

Reference	Imaging system	Subject Model	Tumor model	Probe	Dose	Comments
Chen *et al.* [46]	MicroPET Autoradiograph	Female athymic nude mice(nu/nu)	U87MG Glioblastoma tumor	^{64}Cu-DOTA-PEG-RGD	For biodistribution: 370 kBq (10 μCi). For imaging: 14.8 MBq (400 μCi). For blocking: 10mg/kg c(RGDyK)	Demonstrated the suitability of a PEG moiety to improve *in vivo* kinetics of ^{64}Cu-RGD
Chen *et al.* [47]	MicroPET, Autoradiograph	Female athymic nude mice(nu/nu)	MDA-MB-435 breast cancer	^{64}Cu-DOTA-RGD, [^{18}F]FB-RGD, ^{125}I-RGD	For biodistribution: 10 μCi (^{64}Cu-DOTA-RGD), 20 μCi ([^{18}F]FB-RGD), 2 μCi (^{125}I-RGD). For imaging: 200 μCi ([^{18}F]FB-RGD), 400 μCi (^{64}Cu-DOTA-RGD). For blocking: 2.5mg/kg c(RGDyK)	Compared the tumor targeting ability and *in vivo* kinetics and showed effective blocking (1hr, 2.5, 7.5 mg/kg c(RGDyK)) through coinjection with a blocking dose c(RGDyK)
Chen *et al.* [48]	MicroPET, Autoradiograph	Female athymic nude mice(nu/nu)	U87MG Glioblastoma tumor	[^{18}F]FB-PEG-RGD	For biodistribution: 740kBq (20 μCi). For imaging: 200 μCi. For blocking: 10mg/kg c(RGDyK)	Demonstrated the suitability of a PEG moiety for improving *in vivo* kinetics of [^{18}F]FB-RGD
Haubner *et al.* [49]	PET	Female BALB/c mice	Human M21 and M21-L melanoam	[^{18}F]Galacto-RGD	For biodistribution: 370 kBq. For imaging: 5.5 MBq. For blocking: 6 or 18 mg/kg cyclo(-Arg-Gly-Asp-d-Phe-Val-)	Demonstrated ^{18}F-labeled RGD-containing glycopeptide and noninvasive assessment of the blockade of the receptor by specific antagonists (10min, 6,18mg/kg c(RGDfV))
Janssen *et al.* [30]	Scintigram	Female nude BALB/c mice	Ovarian carcinoma	^{111}In-DOTA-E-[c(RGDfK)]$_2$, ^{99m}Tc-HYNIC-E-[c(RGDfK)]$_2$, ^{90}Y-DOTA-E-[c(RGDfK)]$_2$	For biodistribution: 370kBq (=0.5μg, ^{111}In-DOTA-E-[c(RGDfK)]$_2$, and scrambled one), 1.7MBq (=0.04 μg, ^{99m}Tc-HYNIC-E-[c(RGDfK)]$_2$). For receptor specificity: 1000-fold excess of ^{115}In-DOTA-E-[c(RGDfK)]$_2$. For imaging: 1.8MBq (^{111}In-DOTA-E-[c(RGDfK)]$_2$)	Demonstrated highly specific tumor uptake in a human tumor xenograft and showed that injection of ^{90}Y-DOTA-E-[c(RGDfK)]$_2$ induced a significant regression in tumor growth

Table 2.3 Continued.

Reference	Imaging system	Subject Model	Tumor model	Probe	Dose	Comments
Haubner *et al.* [50] (Also see [51])	Gamma camera imaging	BALB/c mice	Murine osteosarcoma and human M21 melanoma	[^{125}I]P2 , [^{125}I]GP2, [^{125}I]P2, [^{125}I]P4, [^{125}I]P6, [^{123}I]GP2	For biodistribution: 300 to 400 MBq ([^{125}I]P2, [^{125}I]P4, [^{125}I]GP2). For imaging: 5.6 MBq ([^{125}I]GP2). For blocking: 3 or 6 mg/kg cyclo(-Arg-Gly-Asp-d-Phe-Val-).	Demonstrated the improvement of the pharmacokinetics using glycosylation of a modified derivative by using a sugar amino acid and showed the decrease of lipophilicity and hepatic uptake
Winter *et al.* [28]	MRI	Male New Zealand White rabbits	Atherosclerosis	αvβ3-Integrin-targeted paramagnetic nanoparticles	0.5 Ml/kg body weight, 0.1mmol/kg gadolinium-DTPA	Developed a paramagnetic nanoparticle contrast agent targeted to αvβ3 integrins and demonstrated noninvasive molecular imaging of plaque-associated angiogenesis
Chen *et al.* [52]	Optical imaging	Female athymic nude mice(nu/nu)	Glioblastoma (U87MG)	Cy5.5-c(RGDyK)	For imaging: 0.1 to 3 nmol. For biodistribution: 0.5 nmol	Demonstrated receptor specificity and long-lasting tumor accumulation of a RGD-Cy5.5 conjugate in human primary tumor cells in mouse xenografts
Sivolapenko *et al.* [33]	Scintigram	14 patients	Metastatic melanoma	^{99m}Tc-αp2	For biodistribution: 100 to 400 μg (185 to 1222 MBq)	Demonstrated RGD-containing synthetic peptide successfully ocalized metastatic melanoma lesions in man, and its *in vivo* profile predisposes of an attractive and safe novel diagnostic radiopharmaceutical
Hua *et al.* [53]	SPECT	Male C57BL/6 mice	unilateral hindlimb ischemia	^{99m}Tc-NC100692	1.5 mCi of ^{99m}Tc-NC100692	Demonstrated the temporal changes in ischemia induced angiogenesis as targeting integrin αvβ3

Table 2.3 Continued.

Reference	Imaging system	Subject Model	Tumor model	Probe	Dose	Comments
Poethko *et al.* [54]	PET	Female nude mice	pancreatic tumor (AR42J) and M21 melanoma	Gluc-*S*-Dpr([^{18}F]FBOA)TOCA, $(c(RGDfE)HEG)_2$-K-Dpr-[^{18}F]FBOA	For biodistribution: 1.48 to 2.22 MBq. For blocking: 0.4 mg Tyr3-octreotide/kg (10 µg per mouse) or 18mg c(RGDfV) (360 µg per mouse)	Demonstrated that $(c(RGDfE)HEG)_2$-K-Dpr-[^{18}F]FBOA and Gluc-*S*-Dpr([^{18}F]FBOA)TOCA showed favorable pharmacokinetics and high TBR ratios *in vivo*
Chen *et al.* [47]	MicroPET, autoradiography	Female athymic nude mice(nu/nu)	Glioblastoma (U87MG)	[^{18}F]FB-E[c(RGDyK)]$_2$	50 µCi (imaging), 20 µCi (biodistribution), 10mg/kg c(RGDyK) (for blocking Experiment)	Demonstrated that [^{18}F]FB-E[c(RGDyK)]$_2$ has significantly improved tumor targeting efficacy compared to [^{18}F]FB-c(RGDyK)
Wang *et al.* [43]	Optical Imaging	Athymic nude mice	KS1767, M21 or M21-L	Cy5.5-c(KRGDf), IRDye800-c(KRGDf)	For imaging: 3 nmol Cy5.5-c(KRGDf) and IRDye800-c(KRGDf). For blocking: 600 nmol c(KRGDf) 1 hour before the injection of the conjugate at 3 nmol.	Demonstrated *in vivo* near-fluorescence optical imaging and suggested a possible way to quantify the impact of dye conjugate
Li *et al.* [55]	Dual optical and nuclear imaging	Athymic nude mice	M21 and M21-L	^{111}In-DTPA-Bz-SA-Lys(Irdye800)-c(KRGDf)	For biodistribution: 0.4 nmol/mouse (12 Ci/mouse). For imaging: 5 nmol/mouse (90 Ci/mouse). For blocking: 600 nmol of c(KRGDf) followed by the injection of dual-labeled agent 1 h later	Demonstrated that dual modality imaging with dual labeled probe can give complementary information in the assessment of the molecular characteristics of various disease models.
Houston *et al.* [7]	Dual optical and nuclear imaging	Female athymic nude mice	M21 and M21-L	^{111}In-DTPA-Bz-SA-Lys(Irdye800)-c(KRGDf)	For imaging: equivalent dose of 5 nmol of IRDye800 and 90 µCi of ^{111}In	Demonstrated that SNR was significantly higher for optical than nuclear imaging, and optical imaging for the subcutaneous tumor targets had greater sensitivity than nuclear imaging

Table 2.3 Continued.

Reference	Imaging system	Subject Model	Tumor model	Probe	Dose	Comments
Sadeghi *et al.* [31]	Autoradiography	Female apoE-/- mice	Left common carotid artery	^{111}In-quinolone (RP748)	7.4 MBq of RP748 for imaging	Demonstrated that RP748 binds to activated αvβ3 integrin to track the injury-induced arterial proliferation in mice
Meoli *et al.* [32]	SPECT	chronic rat and dogs	injury-induced myocardial angiogenesis	^{111}In- RP748, ^{99m}Tc-2-methoxy-2-metholpropyl-isonitrile (sestamibi), ^{201}Tl,	1.2 mCi of ^{111}In- RP748 and 0.78 mCi of ^{201}Tl for rat; 6.6 mCi of ^{111}In- RP748 and 22.3 mCi of ^{99m}Tc- sestamibi for dog	Used dual isotope SPECT imaging for imaging ischemia-induced angiogenesis and perfusion
Posey *et al.* [34]	Gamma camera	9 patients	Metastatic cancer	^{99m}Tc-Vitaxin	30 mCi of ^{99m}Tc-Vitaxin	Nuclear imaging of tumor vasculature was not successful, while one patient with αvβ3 positive melanoma had imaging of tumor sites. In addition, there was no immune response to Vitaxin (2.5-3.5 mg/kg)
Van Hagen *et al.* [56]	Autoradiography	Male Lewis rats	Rat pancreatic tumor (CA20948)	^{125}I-DTPA-RGD	3MBq	Demonstrated that uptake decreased with increasing peptide amount and the incorporation of the DTPA group in the peptide resulted in renal clearance of the radiopharmaceutical
Gurfinkel *et al.* [44]	Optical imaging	Female athymic nude mice	Murine Kaposi's sarcoma (KS1767)	Cy5.5-c(KRGDf)	For imaging: 3 nmol. For blocking: 600 nmol of c(KRGDf)	Demonstrated the use of a pharmacokinetic analysis on *in vivo* fluorescence data to test for the specificity of a targeted diagnostic fluorescent contrast agent in a murine Kaposi's sarcoma model

Table 2.3 Continued.

Reference	Imaging system	Subject Model	Tumor model	Probe	Dose	Comments
Haubner *et al.* [16]	PET	Mice and 9 patients	M21 and M21L, chondrosarcoma, soft tissue Sarcoma, renal cell carcinoma, villonodular synovitis of the knee	[^{18}F]Galacto-RGD and [^{18}F]FDG	144–200 MBq	Demonstrated PET imaging of integrin αvβ3 expression in cancer patients. The uptake does not correlate with melanoma patient tumor grading, since multiple metastases in the liver, skin, and lower abdomen in a malignant melanoma patient were shown with marked uptake of [18F]FDG but no uptake of [18F]Galacto-RGD.
Chen *et al.* [42]	Optical	Mice	Human glioblastoma (U87MG)	Cy7-c(RGDyK), Cy7-E[c(RGDyK)], Cy7-E{ E[c(RGDyK)]}$_2$	0.5 nmol	Showed that there was no advantage of dimeric and tetrameric RGD peptides over monomeric peptide, while integrin affinity of RGD peptide follows the order of tetramer>dimmer>monomer. They speculated that the observed higher affinity is likely related to receptor clustering
Chen *et al.* [57]	Optical	Mice	Human glioblastoma (U87MG)	Cy5.5-c(RGDyK), Cy5.5-E[c(RGDyK)], Cy5.5-E{ E[c(RGDyK)]}$_2$	0.5 nmol	Showed that multimerization of RGD peptide results in moderate improvement of imaging characteristics of the tetramer, compared to that of the monomer and dimeric counterparts.
Kwon *et al.* [8]	Optical	Mice	Kaposi's sarcoma (KS1767)	Cy5.5-c(KRGDf)	0.5-6 nmol in 200 ul of saline	Demonstrated the dose dependent uptake of Cy5.5-c(KRGDf) to αvβ3 in Kaposi's sarcoma
Gurfinkel *et al.* [44]	Optical imaging	Female athymic nude mice	Murine Kaposi's sarcoma (KS1767)	Cy5.5-c(KRGDf)	For imaging: 3 nmol. For blocking: 600 nmol of c(KRGDf)	Demonstrated the use of a pharmacokinetic analysis on *in vivo* fluorescence data to test for the specificity of a targeted diagnostic fluorescent contrast agent in a murine Kaposi's sarcoma model

Table 2.3 Continued.

Reference	Imaging system	Subject Model	Tumor model	Probe	Dose	Comments
Line *et al.* [58]	Scintigraph	Male SCID mice	DU145 orPC-3	$^{99m}Tc(CO)_3$-labeled RGE4Cmonomer, RGE4C polymer, RGD4C monomer, and RGD4C polymer	31.2-34.9 nmol (14.8-18.5 MBq) of compounds in 200ul of normal saline	Showed increase in tumor uptake in the series RGE4C monomer < RGE4C polymer < RGD4C monomer < RGD4C polymer, and demonstrated specific molecular targeting of the αvβ3 integrin and nonspecific vascular permeability are both significant in the relative tumor localization of polymeric conjugates of RGD4C.
Beer *et al.* [14]	PET	19 patients	Various human tumors	[^{18}F]Galacto-RGD	133-200 MBq	Correlated the level of integrin αvβ3 expression with SUV, MVD, and TBR using PET in human cancer patients

3. INSTRUMENTATION

The fluorescence imaging data presented in this dissertation was obtained using an intensified charge-coupled device (ICCD) developed in the Photon Migration Laboratories or using a commercially available electron multiplication charge-coupled device (EMCCD). This section contains a brief discussion of the ICCD, EMCCD, liquid crystal tunable filter, and optical components used for small animal imaging.

3.1 Intensified Charge-coupled Device System

The fluorescence-enhanced intensified charge-coupled device (ICCD) system instrumentation was developed in the Photon Migration Laboratories. The main ICCD components for continuous wave (CW) imaging are (1) a charge-coupled device (CCD) camera, (2) a CCD cooling unit, and (3) a CCD controller, and (4) an image intensifier. The CCD camera (model: PI-SCX, Roper Scientific in Tucson, AZ) has 16-bit dynamic range with a frame transfer CCD chip. In addition, it features 1024 x 1024 pixels where each pixel is 13 μm in length. Due to the 16-bit dynamic range, where 2^{16} is equivalent to 65,536 gray levels, the CCD camera can detect very dim and very bright fluorescent area within an image. In addition, unlike the full-frame CCD that must wait for all charge to be readout prior to beginning the next exposure, the frame-transfer CCD has a maximum digitation frequency of 5 MHz and has its parallel register divided into two distinct areas; the image and storage arrays. When the CCD is exposed to light, the charge is accumulated in the image array. Then, the accumulated charge in the image array is

rapidly transferred to the storage array (in less than 300 microseconds), which enables the image array to begin next exposure without the need of a mechanical shutter.

Quantum efficiency, the fraction of incoming photons that are absorbed by the CCD, and system read-out noise, as inherent property of the CCD, are important features which affect signal-to-noise ratios at low light levels. The optimal quantum efficiency of the CCD is between approximately 200 to 900 nm.

The CCD camera has a fiber bundle that is directly laminated to the square CCD chip, enlarging the size of CCD. Therefore, an image intensifier can be directly attached to CCD without loss of resolution. The image intensifier amplifies low fluorescence emission signals, resulting in a better signal to noise ratio (SNR). The image intensifier (Gen. 3 Pinnacle™, model: FS9910, ITT NightVision, Roanoke, VA) was used for the small animal imaging presented in Sections 4, 5, and 6.

3.2 Electron-Multiplying Charge-coupled Device

Although image intensifier in ICCD camera system amplifies extremely low fluorescence signals to enable highly sensitive imaging, the intensifier is susceptible to damage when exposed to high signal levels. In addition, the CCD camera has a maximum digitation frequency of 5 MHz, which limits rapid, real-time dynamic fluorescence imaging. Hence, an electron-multiplying CCD (EMCCD) camera (model PhotoMAX:512B, Princeton Instruments, Trenton, NJ) was used for dynamic imaging without the addition of the image intensifier. Figure 3.1 shows a schematic of 'on-chip multiplication gain' which is employed in EMCCD camera system to multiply photon-

generated charge above the read noise levels at video frame rates. The multiplication gain occurs after the device detects a photon but before the chip read-out amplifier. In the extended multiplication register, the CCD clock voltages, which control gain, accelerate electrons from pixel to pixel, resulting in the generation of secondary electrons by an impact-ionization process. Therefore, this process can reduce the CCD read-out noise, which is one of the primary noise sources, by varying clock voltage, on-chip multiplication gain factor. The ICCD system employs a 5 MHz, 16-bit digitizer, while EMCCD camera uses a 10 MHz, 16-bit digitizer. Therefore, with ROI selection and/or binning, the frame rates in excess of 400 frames per second are possible.

PhotonMAX is the back-illuminated CCD with dual-amplifiers. PhotonMAX has an active imaging area of 512x512 pixels, where each pixel is 16 μm in length. In addition, it does not require a cooling unit, since deep thermoelectric cooling (-70 C) is used to suppress system noise. The thermoelectric cooling method uses a Peltier cooler in combination with air-circulation. Quantum efficiency is 90 % at 550 nm and 65 % at 830 nm. This system is used only for CW imaging, since this camera can not modulate incoming photons. PVCAM is a dynamic link library (DLL) of functions. The imaging acquisition software V++ (Digital Optics, New Zealand) uses DLL library of ICCD and EMCCD to control the camera and acquire the images. The EMCCD camera was used for the experimental work described in Sections 7 and 8.

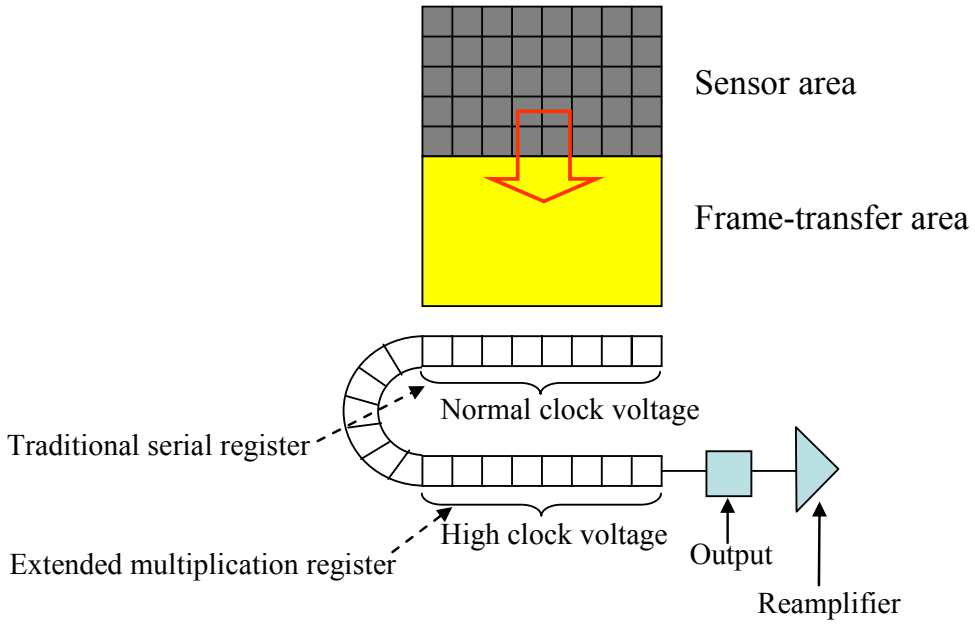

Figure 3.1 Schematic of 'on-chip multiplication gain' in EMCCD camera system. Reproduced from [4].

3.3 Liquid Crystal Tunable Filter

A liquid crystal tunable filter (LCTF) is a birefringent optical filter that can select a specific center wavelength for transmission, since the birefringent element is a material that displays two different indices of refraction, while rejecting wavelengths outside this wavelength band. LCTF is based on the lyot filter principle. A lyot filter is made from several birefringent plates where each plate is half the thickness of the previous one. Since each birefringent plate is surrounded by polarizers, the filter has a spectral transmission peak. While a lyot filter provides a static bandpass, if the filter has electrically tunable birefringent elements inserted, an electrically tunable filter can be obtained. As shown schematically in Figure 3.2 (a), each stage consists of an initial linear polarizer, a birefringent element, a liquid crystal waveplate, and a final analyzer

oriented on an axis parallel to the initial polarizer [5]. The liquid crystal waveplate is comprised of two transparent electrodes on either side of a cell filled with nematic liquid crystals [5]. The electrodes are normal to the incident light and the alignment of liquid crystals is initially perpendicular to the light path (Figure 3.2 (b)). When a voltage is applied across the electrodes, the molecules align with the applied electrical field. This produces a waveplate with an electronically adjustable retardance [5].

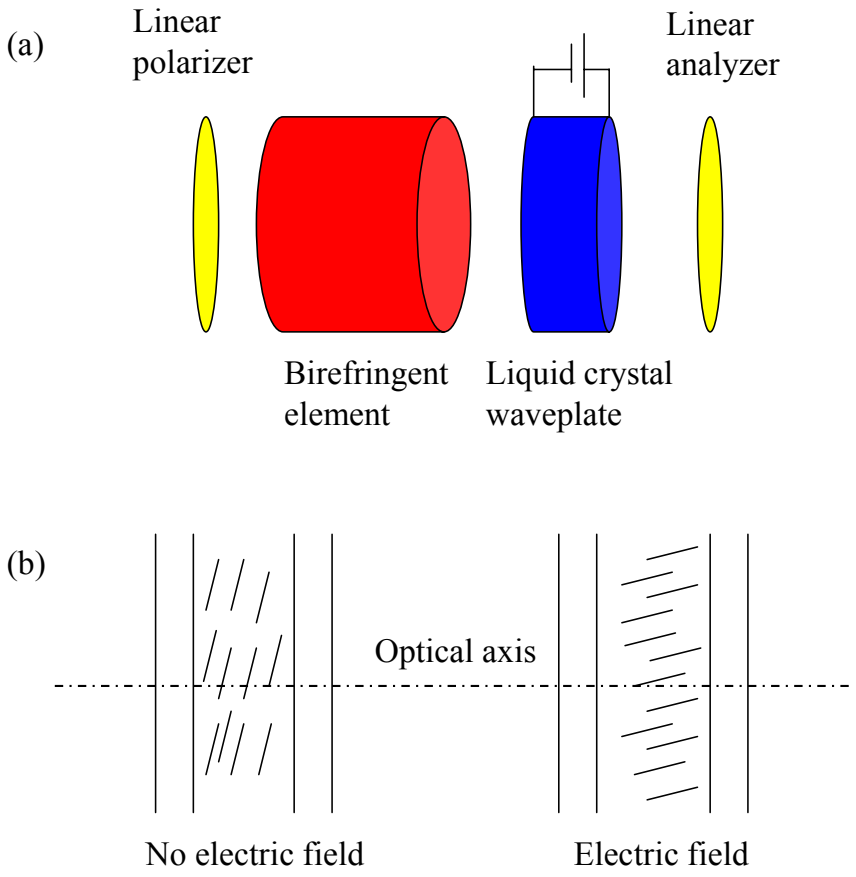

Figure 3.2 Schematic of a LCTF single stage (a) and alignment of liquid crystals when a voltage is applied across the electrodes (b). Reproduced from Slawson *et al.* [5]

The LCTF (Varispec: SNIR, Cambridge Research & Instrumentation, Inc., Woburn, MA) has a spectral bandwidth of 7 or 10 nm, with a central wavelength electronically tunable between 650 and 1100 nm. Transmittance varies from 18 % at 650 nm to 67 % at 1100 nm for randomly polarized incident light. The LCTF has a 20mm circular clear aperture. The response time for altering wavelengths of the filter is 150 ms at 25 °C [59].

3.4 Optical Components and Accessories

Fluorescence imaging requires light with an appropriate wavelength source to excite a fluorophore. In the experimental studies in this thesis, we employ laser diodes (660-nm, 35-Mw, model HL6501MG, or 785-nm, 80-Mw, model DL7140-201, ThorLabs, Inc., Newton, NJ). For uniform illumination of excitation light on the object to be imaged, a plano-convex lens and an optical diffuser are placed in front of the laser diode. In addition, the intensity and wavelength of excitation light are maintained constant by a laser diode driver and temperature controller (ThorLabs, Inc., models LDC500 and TEC2000, respectively, Newton, NJ).

For optimal performance of fluorescence imaging, the optical filters used consist of a holographic notch-plus band rejection filter (660 nm center wavelength for Cy5.5 or 785 nm center wavelength for IRDye800 or indocyanine green (ICG), Kaiser Optical Systems, Inc., Ann Arbor, MI) and a bandpass or interference filter (710 nm center wavelength for Cy5.5, model F10-710.0-4-2.00 or 830 nm center wavelength for IRDye800 or ICG, model F10-830.0-4-2.00, CVI Laser Corporation, Albuquerque, NM)

to reject backscattered excitation light and isolate fluorescence light. A Nikon 50 nm f/1.8 zoom AF Nikkor camera lens for ICCD camera system and 28 mm f/2.8 zoom AF Nikkor camera lens for EMCCD camera combine the optical filters to provide accurate focus adjustment.

4. *IN VIVO* DYNAMIC FLUORESCENCE IMAGING IN XENOGRAFTS BEARING HUMAN KAPOSI'S SARCOMA FOR ANALYSIS OF DOSE-DEPENDENT UPTAKE OF A FLUORESCENTLY LABELED RGD TARGETED TO αvβ3 RECEPTORS [*]

Section 4 in this thesis describes the small animal imaging undertaken at the University of Texas M. D. Anderson Cancer Center in Houston. Animal care and preparation of fluorescent contrast agents were performed by our collaborators who are gratefully and individually recognized in the Acknowledgments section in this thesis. Although the data was obtained with our collaborators, the PK analysis of the data was performed entirely by the author. The experimental studies in this section are intended to analyze the molecular uptake of a molecularly targeting agent *in vivo* during dynamic fluorescence imaging. The work presented in this section was published in *Journal of Molecular Imaging* and *Proceedings of the SPIE*.

4.1 Introduction

As described in Section 2, the vitronectin receptor, αvβ3, plays an important role in tumor metastasis and angiogenesis [60-64], which is the growth of new blood vessels from pre-existing vasculatures during tumor growth [61, 65, 66]. This integrin is expressed on tumor cells as well as on angiogenic endothelial cells [67-72]. Furthermore, it has been shown that antagonists of αvβ3 induce tumor regression and apoptosis of

[*] Reprinted in part with permission from Kwon S, Ke S, Houston JP, Wang W, Wu Q, Li C, and Sevick-Muraca EM (2005). Imaging Dose-Dependent Pharmacokinetics of an RGD Fluorescent Dye Conjugate Targeted to Alpha v Beta 3 Receptors in Kaposi 's sarcoma. *Mol Imaging*, **4**, 75-87. Copyright 2005 by the Society of Molecular Imaging.

angiogenic endothelial cells [72-74], thus implying that the αvβ3 integrin may be as a viable therapeutic target. Therefore, noninvasive imaging methods for quantitative and visual monitoring of αvβ3 integrin expression in real-time could provide opportunities for assessing therapeutic intervention as well as for detection of metastasis.

Kaposi's sarcoma (KS1767), a common cancer in HIV-infected patients [75], is characterized by intense angiogenesis producing a highly vascular tumor with concurrent elevated αvβ3 expression [76, 77]. Arginine-glycine-aspartic (RGD) has been identified as one antagonist of αvβ3 and has been radiolabeled for diagnostic imaging and therapeutic purposes. Table 2.3 contains a list of previous experimental cancer imaging studies performed by targeting αvβ3 using the RGD peptide motif. To date, with the exception of a few laboratories [41, 43, 52], all RGD-based imaging has been performed using the "gold-standard" of molecular nuclear imaging. In a recent analysis of nuclear and near-infrared (NIR) optical scintigraphy in which xenografts bearing melanoma were administered a dual-labeled RGD imaging agent, we have shown that fluorescence imaging has significantly higher signal per mass of agent, enabling rapid and dynamic imaging [7, 55]. Unfortunately, to date there are no standardized fluorescence imaging systems and newly reported evidence from our laboratories suggests that target-to-background (TBR) values generated from intensity-based fluorescence imaging systems which produce planar images may be more likely dependent upon instrumentation rather than on the selectivity of the targeting contrast agent [78].

While tomographic imaging systems are under development in our laboratory as well as in others, we have taken advantage of the high signal intensity afforded by

fluorescence imaging and have developed dynamic optical imaging system. This modality can determine the rate of fluorescent agent uptake which is not dependent upon instrumentation artifacts as TBR may be [8, 78]. In addition, we have shown that pharmacokinetic analysis of dynamic optical imaging can provide quantitative information relating to the availability of integrin receptor target as caused by the administration of unlabeled RGD peptide one hour prior to administration of the targeted imaging agent [44]. Our pharmacokinetic analysis assumed three compartments: (i) unbound conjugate in the vascular space, (ii) unbound conjugate in the extravascular space, and (iii) bound conjugate in the vascular and extravascular spaces as associated with proliferating endothelium as well as Kaposi sarcoma cancer cells. Furthermore, we assumed that an unsaturated receptor binding model, which predicts that the rate of uptake of fluorescent labeled RGD depends linearly upon its concentration as well as on the density of available integrin receptors. When the administration of agent at large doses causes receptor saturation, the rate of uptake should be independent of the concentration of administered fluorescently labeled RGD. However, there is currently no means to determine the concentration at which binding is saturated *in vivo*. For the purposes of molecular diagnostics, it is important to know the optimal dose of agent in order to avoid receptor oversaturation and excess administration of the imaging agent. The optimal dose of a diagnostic agent may also provide information for the optimal dose of molecular therapeutic agents for individualized therapies. However, it is unclear whether the administration of a molecular diagnostic or a therapeutic agent is at a level which causes saturation of the binding sites *in vivo*.

In this contribution, we demonstrate the use of dynamic optical imaging to assess changes in integrin-targeting as a function of agent dose in order to evaluate not only the availability of the integrin receptor, but also its expression level. From a non-invasive assessment of the disease marker availability through these dynamic molecular imaging approaches, a simplified and sensitive approach for individualized molecular therapies can be envisioned. In the following sections, we present pharmacokinetic models, animal and tumor models, and instrumentation used in this study to generate the dose-dependent pharmacokinetic response from planar, fluorescence optical imaging.

4.2 Pharmacokinetics

The three-compartment pharmacokinetic models which describe molecularly specific uptake in the vascular or extravascular compartments are described schematically in Figure 4.1. The models are comprised of the unbound vascular component, unbound extravascular component, and the bound component and whether each is associated with proliferating endothelium in the vascular space (Figure 4.1 a) or cancer cells in the extravascular space (Figure 4.1 b). In dynamic imaging studies, fluorescence intensity was detected at the animal tissue surface, which may be mediated by the time-invariant autofluorescence and optical properties of scattering and absorption in the tissue over the short period of imaging time, and by the time-dependent concentration of the fluorophore within each compartments.

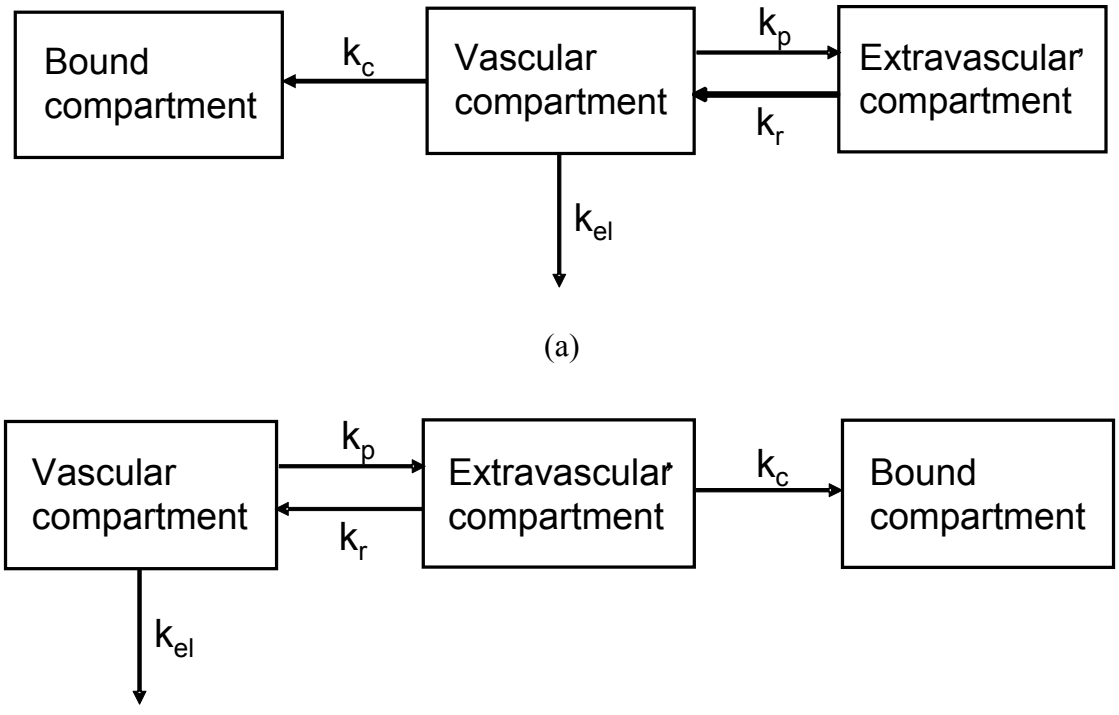

Figure 4.1 Description of two three-compartment PK models used to describe the uptake of a fluorescent contrast agent by proliferation endothelium in the vascular space (a) and cancer cells in the extravascular space.

The time-dependent fluorescent intensity can be expressed by

$$I(t) \cong w_1 C_{VASCULAR}(t) + w_2 C_{EXTRAVASCULAR}(t) + w_3 C_{BOUND}(t), \qquad (4.1)$$

where $I(t)$ is the time-dependent fluorescence intensity and w_1, w_2, and w_3 are weighting factors that not only represent the fraction of the vascular, extravascular, and bound compartment, respectively, but also account for the attenuation that occurs due to light propagation in each compartment. In the short imaging times employed herein, the w_i 's are considered constant. $C_{VASCULAR}(t)$ and $C_{EXTRAVASCULAR}(t)$ represent the concentration of unbound Cy5.5-c(KRGDf) in the vasculature and extravascular

compartments, respectively while $C_{BOUND}(t)$ represents the concentration of conjugate bound to integrin receptor whether in the vascular (Figure 4.1 (a)) or extravascular (Figure 4.1 (b)) compartments. Finally, the time-dependent observed fluorescence intensity was solved for both PK models of Figure 4.1 (a) and Figure 4.1 (b) to yield the common solution:

$$I(t) = I_o + A[1-\exp(-\alpha t)] + B[1-\exp(-\beta t)], \tag{4.2}$$

where I_0 is the background fluorescence intensity level:

$$I_0 = w_1 C_{VASCULAR}(0), \tag{4.3}$$

where $C_{VASCULAR}(0)$ is the concentration in vascular compartment at the time of i.v. bolus injection of the conjugate. After subtracting the background intensity, the final time-dependent observed fluorescence intensity may be expressed as:

$$I(t) = A\left[1-\exp(-\alpha t)\right] + B\left[1-\exp(-\beta t)\right]. \tag{4.4}$$

For Figure 4.1 (a) pre-exponential factors are given by:

$$A = \frac{C_{Bo}}{\alpha-\beta}\left[k_p w_2 - (\alpha - k_r)w_1 - \frac{k_c(k_r-\alpha)w_3}{\alpha}\right], \tag{4.5}$$

$$B = \frac{C_{Bo}}{\alpha-\beta}\left[(\beta - k_r)w_1 - k_p w_2 - \frac{k_c(\beta-k_r)w_3}{\beta}\right], \tag{4.6}$$

and for Figure 4.1 (b):

$$A = \frac{C_{Bo}}{\alpha-\beta}\left[k_p w_2 - (\alpha - k_{EES})w_1 - \frac{k_c k_p w_3}{\alpha}\right], \tag{4.7}$$

$$B = \frac{C_{Bo}}{\alpha-\beta}\left[(\beta - k_{EES})w_1 - k_p w_2 + \frac{k_c k_p w_3}{\beta}\right]. \tag{4.8}$$

For Figure 4.1 (a) the time dependent terms are given by:

$$\alpha = \tfrac{1}{2}\left[k_a + k_r + \sqrt{(k_a - k_2)^2 + 4k_r k_p} \right], \tag{4.9}$$

$$\beta = \tfrac{1}{2}\left[k_a + k_r - \sqrt{(k_a - k_r)^2 + 4k_r k_p} \right], \tag{4.10}$$

where

$$k_a = k_c + k_p + k_{el}, \tag{4.11}$$

and for Figure 4.1 (b):

$$\alpha = \tfrac{1}{2}\left[k_{EES} + k_B + \sqrt{(k_{EES} - k_B)^2 + 4k_r k_p} \right], \tag{4.12}$$

$$\beta = \tfrac{1}{2}\left[k_{EES} + k_B - \sqrt{(k_{EES} - k_B)^2 + 4k_r k_p} \right], \tag{4.13}$$

where

$$k_{EES} = k_r + k_c, \text{ and } k_B = k_{el} + k_p. \tag{4.14}$$

The kinetic terms are different between the two models and are defined as illustrated in Figure 4.1 (a) and (b). In the initial dynamic imaging of short duration, the concentration difference between bound and unbound agent is the greatest and we assume reverse binding to be negligible as shown in Figure 4.1. Furthermore, if dyes do not experience specific, molecular targeting, the vascular and extravascular compartments may be sufficient to describe their distribution. However, for dyes with molecular specificity, it is necessary to include the third compartment, which represents surface

receptor binding and/or cellular uptake at a molecular level. The rate constant at which the dye accumulates in the bound compartment is denoted by k_c, regardless of the PK model chosen.

The pre-exponential parameters *A* and *B* reflect the magnitude of the detected fluorescence signal, which can provide the differentiation between contralateral normal and tumor tissue regions within an individual animal. For both PK models, the expression of $\alpha + \beta$ represents the sum of all rate constants between the various compartments:

$$\alpha + \beta = k_p + k_r + k_{el} + k_c, \tag{4.15}$$

which can be exploited as the dose response at various dose amounts in tumor ROIs among all animals. Assuming that all rate constants are unchanged except k_c, variation of net uptake at different doses in different animals can be attributed to receptor binding. Previous work from our laboratory shows that there is no significant difference in the PK parameters of $\alpha + \beta$ of free, non-targeting Cy5.5 dye associated with KS1767 and contralateral normal tissues [44].

4.3 Materials and Methods

4.3.1 Animal and Tumor Models, and Fluorescently Conjugated RGD

Four to six week-old female athymic nude mice (nu/nu; 18 –22 g) were purchased from Harlan Sprague Dawley, Inc. (Indianapolis, IN) and housed five per cage and fed sterilized pelleted food (Harlan Sprague Dawley Inc., Indianapolis, IN) and sterilized

water. Animals were maintained in a pathogen-free mouse colony in the Department of Veterinary Medicine (The University of Texas M. D. Anderson Cancer Center, Houston, TX). The facility is accredited by the American Association for Laboratory Animal Care and all experiments were performed in accordance with the guidelines of the Institutional Animal Care and Use Committee. Human Kaposi's sarcoma (KS1767) cells to be implanted into mice were harvested near confluence by incubation with 0.05% trypsin-EDTA. KS1767 Cells (2-3 × 10^6 / animal) were implanted subcutaneously into the hind region of mice.

Cyclo(Lys-Arg-Gly-Asp-Phe)[c(KRGDf)] was synthesized on linker-PL-DMA resin using Fmoc solid chemistry at the M.D. Anderson Cancer Center by Dr. Wei Wang [43].

4.3.2 Experimental Methods

Animals were subdivided into eight test groups (n=3 for each test group) based on the dose amount of contrast agent administered. Six dose groups received different amounts of Cy5.5-c(KRGDf), while two blocking groups received RGD peptide at 300 or 600 nmol one hour prior to the 3 nmol of Cy5.5-c(KRGDf). Prior to imaging and agent administration, mice were anesthetized with Nembutal (Sigma, St. Louis, MO, 50 mg/kg bw, i.p.), and a tail vein catheter was introduced in each animal. Animals were then placed on the temperature-controlled water circulation pad (Heat Therapy Pump T/Pump®, Model No. TP-500, Gaymar Industries Inc., Orchard Park, NY) at 37 C under

isofluorane anesthesia (VetEquip, Pleasanton, CA and IsoSol Isofluorane USP, VEDCO Inc., St. Joseph, MO). Imaging commenced prior to the administration of agent.

4.3.3 Fluorescence Imaging System

Figure 4.2 illustrates the experimental apparatus used for small animal fluorescence imaging. A laser diode (35 Mw, 660-nm for Cy5.5 excitation) provided excitation light, which uniformly illuminated the whole body of the mouse through a convex lens and diffuser. To reject backscattered and reflected excitation light, a holographic notch-plus band rejection filter (660-nm center wavelength; Kaiser Optical Systems, Inc., model, Ann Arbor, MI, OD at λ_x reported to be >6) and a bandpass filter (710-nm center wavelength; CVI Laser, model, OD at λ_x reported to be 3) were positioned prior to a 28-50-mm Nikkor lens (Nikon, Japan). Therefore, re-emitted fluorescence light and the small amount of leaked excitation light [78] was detected by an intensified charge-coupled device (ICCD) camera (Photometrics, model CH350/L, Tucson, AZ) coupled to an image intensifier (model FS9910C, ITT Night Vision, Roanoke, VA).

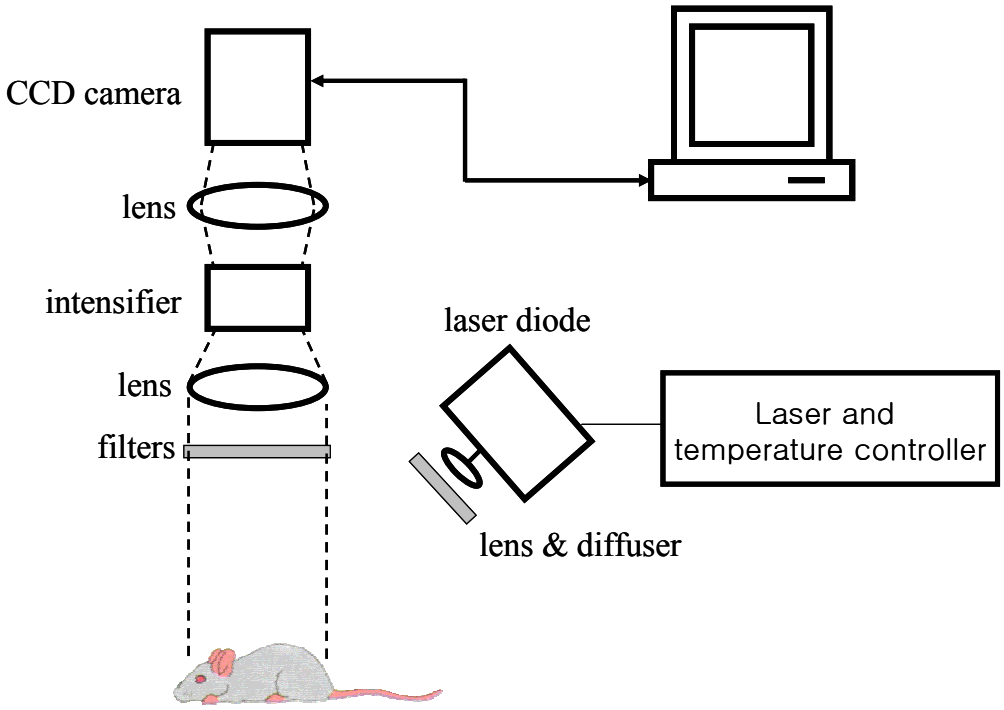

Figure 4.2 Instrumentation for the intensified charge-coupled device (ICCD) system for the small animal imaging.

When a low-power lamp provided a white-light source for white light images, the filters were removed. All images were acquired by a personal computer with V++ imaging software (Digital Optics, Auckland, New Zealand). Imaging commenced with initial white-light images and at least six images serving as "background" images prior to bolus administration of the imaging agent. Dynamic fluorescence images were acquired immediately following the injection of contrast agent for approximately 20-mins. The injected dose of Cy5.5-c(KRGDf) was varied from 0.75 to 6-nmol per animal. The CCD integration time was 3000-msec for the 0.75 nmol dose, 1000-msec for 1 and 1.25 nmol doses, and 300-msec for 1.5, 3 and 6 nmol agent doses in order to maintain signal to

noise ratio. Fluorescence images were also obtained under ocalized e anesthesia at 24 and 48 hours after initial injection of the imaging agent at all doses.

4.3.4 Data Processing and Statistics

After completion of the image acquisition, data analysis and processing was accomplished by Matlab software (The MathWorks, Inc., Natick, MA), SigmaPlot software package (SPSS Inc., Chicago, IL), and ImageJ (National Institutes of Health, Washington, DC). First, the average of the six background images was subtracted from each of the acquired fluorescence images. Using white light images, two regions of interest (ROI), (i) the tumor and (ii) the contralateral normal ROI, were defined, each having the same numerical surface area. The mean of the fluorescence intensity within each ROI in each fluorescence image was calculated. Using this data, plots of mean fluorescence intensity versus time profiles after agent administration were fitted to solution of the pharmacokinetic models. The statistical analysis was performed with SPSS 12.0.1 statistical program (SPSS, Inc., Chicago, Illinois). The data from the non-linear least-squares regression were analyzed using one-way ANOVA, LSD, Student t-test. The differences were considered significant at $p < 0.05$.

4.4 Results

4.4.1 *In vivo* NIR Fluorescence Imaging

Figure 4.3 a presents an example of white light and fluorescence images of a xenograft bearing a subcutaneous human Kaposi's sarcoma on the left anterior limb 24

hours after the injection of 3 nmol dose of Cy5.5-c(KRGDf) conjugate. During all acquisition times for all animals, the tumor was detected from the fluorescence images, up to 48 hours after agent administration. Cy5.5-c(KRGDf) was also excreted to the bladder as evident from the fluorescent images. In order to demonstrate the binding specificity of the Cy5.5-c(KRGDf), fluorescence imaging was performed 24 hours after injection of 3nmol dose of Cy5.5-c(KRGDf) conjugate but 25 hours after the injection of 600nmol of c(KRGDf) peptide as a competitive agent. The examples of white light and fluorescent images of the blocked receptor xenografts are illustrated in Figure 4.3. The fluorescence images with the same exposure time are illustrated on the same linear color scale to allow for a qualitative comparison. For all animals (n=3), the fluorescence intensity originating from the tumor ROIs was larger when Cy5.5-c(KRGDf) conjugate was administered alone as compared to when c(KRGDf) was administered 1 hour prior to imaging agent administration. The reduced uptake of Cy5.5-c(KRGDf) resulting from preadministration of c(KRGDf) validates the *in vivo* molecular specificity of the conjugate to $\alpha v\beta 3$ receptors [44].

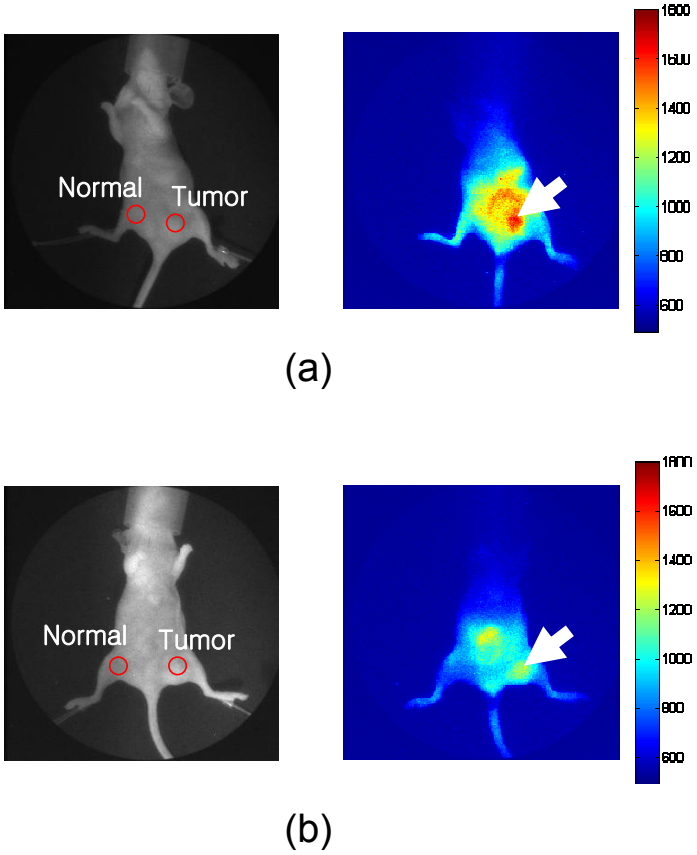

Figure 4.3 White-light images (left column) and Fluorescence images (right column) 24 hours after the administration of (a) 3 nmol of Cy5.5-c(KRGDf) conjugate alone, (b) RGD-Cy5.5 conjugate 1-hour after the injection of 600nmol of RGD peptide. The white arrows on the fluorescence images indicate the location of the xenografted Kaposi's sarcoma tumor.

4.4.2 Dynamic Fluorescence Imaging

Figure 4.4 displays the fluorescence intensity (in arbitrary units) in (a) selected tumor and (b) corresponding normal tissue ROIs as a function of time after administration for one of three animals injected with 0.75, 1.5, and 3 nmol doses of Cy5.5-c(KRGDf) and one of three animals injected with 3 nmol dose of conjugate one hour after administration of 600 nmol of c(KRGDf). It also shows the results of the

regression and the corresponding least-squares fit. The coefficient of determination R^2 for the regression was 0.99 or greater in all cases. As shown in the Figure 4.4, the fluorescence intensities in tumor ROIs are higher than those in their corresponding normal ROIs. The figure also shows fluorescence intensities with the conjugate administered at 0.75 nmol are the highest, because of the longer camera integration time of 3000 msec in comparison to the 300 msec integration times employed for the other dosages. When compared to intensities from 1.5 nmol dose of the conjugate alone, fluorescence intensities resulting from 3 nmol dose of the conjugate 1 hour after injection 600 nmol of c(KRGDf) are higher with the same integration time.

A ratio of the target (tumor ROI) to background (contralateral normal tissue ROI) fluorescence intensity normalizes against differing CCD integration time, since both tumor and normal tissue are collected in the same animal using the same image acquisition parameters. However, TBR may fail to account for differences in the fractional contribution of excitation light leakage [78], non-uniformity of excitation illumination, as well as the background autofluorescence which results from the red excitation wavelength. Figure 3.5 shows the average and standard deviation of the TBR for four groups of animals in the injection of Cy5.5-c(KRGDf) at doses of 0.75 (n=3), 1.5 (n=3), 3 nmol (n=3) and 3 nmol 1 hour after injecting 600 nmol of c(KRGDf) (n=3) as a function of time after administration.

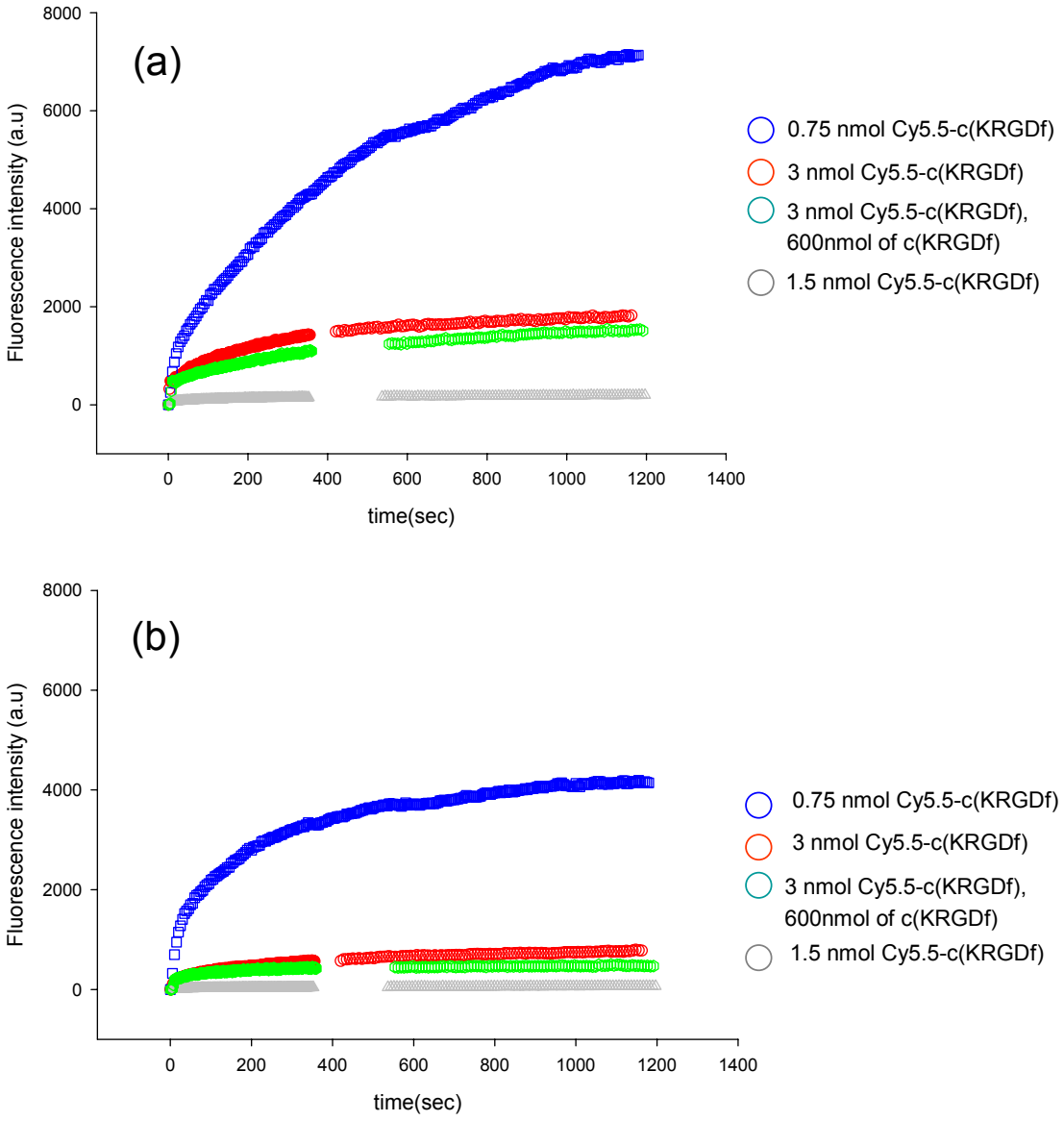

Figure 4.4 Fluorescence intensity vs. time profiles from the animal that received an injection of the Cy5.5-c(KRGDf) conjugate at 0.75 nmol (○), 3 nmol (○), 3 nmol 1 hour after the injection of 600nmol of c(KRGDf) (○), and 1.5 nmol (○) from above, acquired from the (a) tumor and (b) normal ROIs.

Figure 4.5 shows that the mice administered 0.75 nmol of the conjugate have the highest TBR while the mice administered 1.5 nmole have the lowest TBR. Furthermore, the TBR of mice injected with 600 nmol of c(KRGDf) prior to the injection of 3 nmol of Cy5.5-c(KRGDf) is higher than one of mice injected with 1.5 nmol of the conjugate.

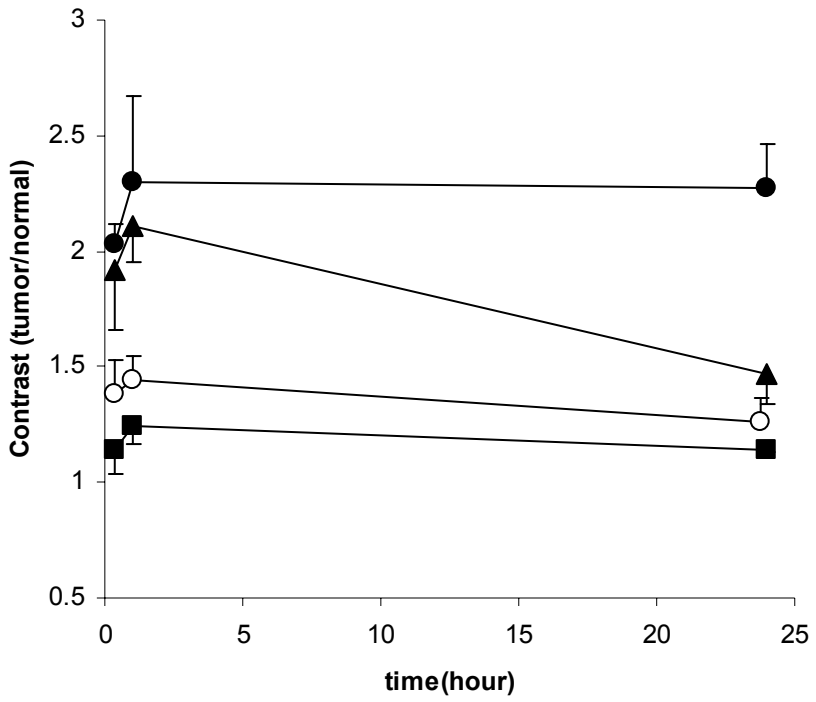

Figure 4.5 The ratio of the tumor to normal ROIs' intensities. The closed circles (●), triangles (▲), and squares (■) denote data from an animal receiving 0.75 nmol, 3 nmol, and 1.5 nmol of Cy5.5-c(KRGDf), respectively. The open circles (○) denote the mouse injected with 3nmol of Cy5.5-c(KRGDf) conjugate after the injection of 600nmol of c(KRGDf). The points represent the mean value of the test group and the error bars the standard deviation.

4.4.3 Pharmacokinetic Analysis

Figure 4.6 shows that the PK values of A and B in tumor region are higher than those in normal tissue region in each animal. The values of A and B are not only dependent upon the concentration of injected fluorophore but also vary with experimental conditions such as detector sensitivity, incident excitation fluence, and light leakage through optical filters. Therefore, A and B are not solely representative of the molecular specificity of conjugate uptake among all test groups in tumor ROIs but instead may reflect filter light leakage, integration time, autofluorescence, camera and intensifier gain, etc. However, because the exponential factors α and β are dictated only by the shape of the fluorescence intensity vs. time profiles rather than the magnitude of detected signal, they may be directly comparable between different experimental trials utilizing the same contrast agents regardless of the exposure time, differences in incident excitation fluence, as well as excitation light leakage through optical filters. Figure 4.7 shows that for all test groups the sum of α and β in normal ROIs from images resulting from different dosages of conjugate are not statistically different ($p = 0.86$), while those in tumor ROIs are different ($p < 0.0001$) and apparently depend upon the administered dose of imaging agent. The PK value of $\alpha + \beta$ in the tumor region with the conjugate alone is the lowest at the dose of 0.75 nmol, and the highest at 1.5 nmol. The figure shows a linear relationship between the dose amount and $\alpha + \beta$ for tumor ROIs for doses up to 1.5 nmol of Cy5.5-c(KRGDf). The PK value of $\alpha + \beta$ in tumor ROIs of mice injected with a dose of 0.75 nmol is significantly different ($p < 0.02$) compared to the corresponding values for mice injected with doses ranging from 1.25 to 6 nmol.

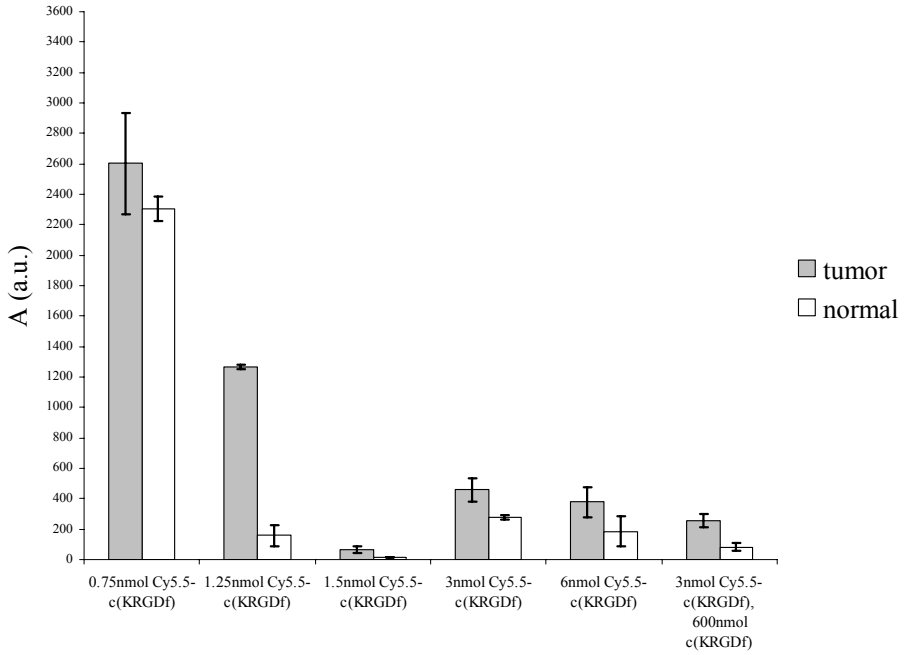

(a)

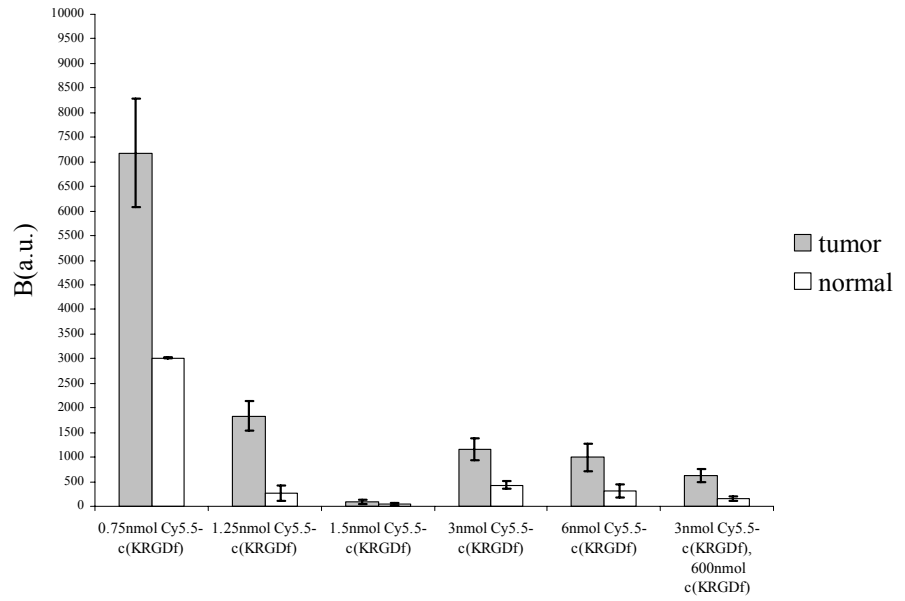

(b)

Figure 4.6 Results of the pharmacokinetic pre-exponential factors (a) *A* and (b) *B* after the non-linear least-squares regression. The column height represents the mean value of the test group (n=3 for each group) and the error bars represent the standard deviation.

Also, the value of α + β in tumor ROIs of mice injected at 1 nmol dose is statistically different ($p < 0.05$) from those values arising from doses ranging from 1.5 to 6 nmol. However, there is no significant difference in the values of α + β associated with tumor ROIs when Cy5.5-c(KRGDf) dose is varied from 1.5 to 6 nmol ($p = 0.25$). The PK parameters of α + β in the normal and tumor ROIs are not statistically different when free c(KRGDf) is pre-administered at doses of 300 or 600nmol 1 hour prior to administration of Cy5.5-c(RGDf) [44]. There is also no difference of α + β values in either normal or tumor ROIs between of blocking groups receiving c(KRGDf) prior to 3 nmol of the conjugate and the dose group of animals receiving 0.75 nmol of the conjugate alone.

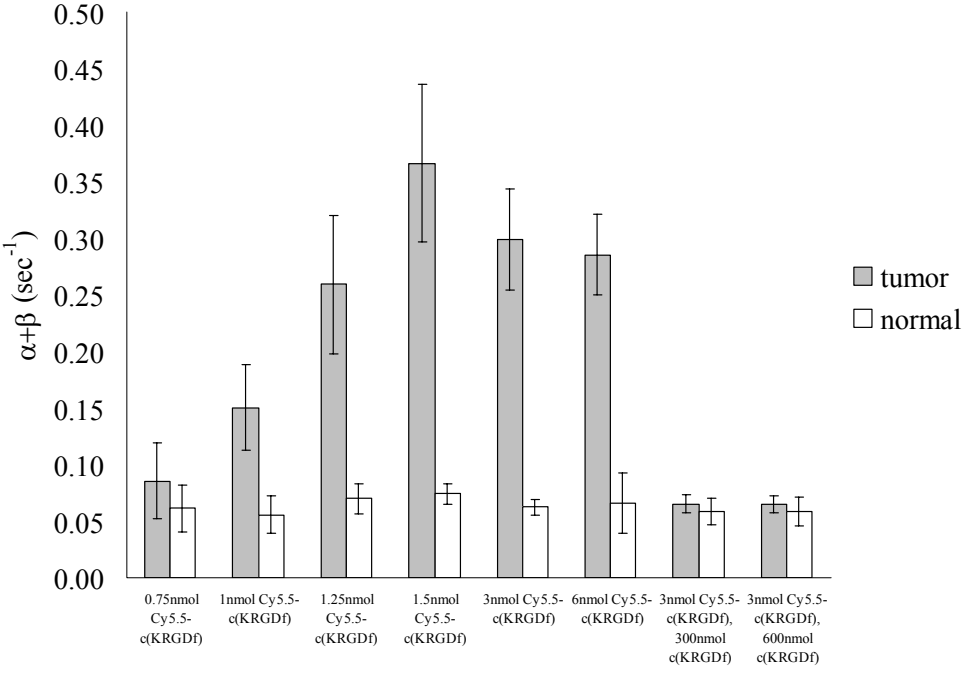

Figure 4.7 The sum of the pharmacokinetic constants α and β in the tumor and normal ROIs. The column height represents the mean value of the test group and the error bars represent the standard deviation.

4.5 Discussion

In this study, we demonstrated the advantages of dynamic imaging for dose-dependent uptake and compared the resulting pharmacokinetic values with the conventional measurement of TBR. As shown in Figure 4.4, the acquired fluorescent intensities within selected ROIs are dependent not only on agent dose, but also on the camera integration times, which are varied in order to collect comparable signal to noise at the varying doses. For example, the fluorescence intensities in tumor and tissue ROIs at 0.75 nmol Cy5.5-c(KRGDf) dose integrated over 3000 msec are larger in comparison to those from 3 nmol dose integrated over 300-msec (Figure 4.4). While the ratio of fluorescent counts of tumor to normal tissue ROIs, or the TBR, may normalize out the variation of integration times, systematic biases owing to excitation light leakage [78], autofluorescence, and variation in excitation light illumination with animal position or viewing angle [52] nonetheless alters TBR. Contribution of systematic biases to TBR becomes more pronounced with increased integration time. For example, Figure 4.5 shows the highest TBR for the lowest dose (0.75 nmol) but the highest integration time (3000 msec). Chen *et al.* [52] also used TBR to show the specificity of Cy5.5-conjugated RGD peptide in subcutaneous U87MG glioblastoma tumor model as a function of dose, but also noted changes in TBR that were unrelated to dose. Using a non-intensified CCD, their integration times were 120 sec for doses of 0.1, 1.5, and 3 nmol as opposed to our integration times of 300-msec at the dose of 1.5, 3, and 6 nmol and 1-3 seconds at 0.75, 1 and 1.25 nmol. A detector with increased sensitivity enables image acquisition over shorter integration times with reduced contribution of systematic bias in TBR. For the

red excitable dye such as Cy5.5, the endogenous autofluorescence and the fluorescence owing to chow may contribute to a higher systematic noise level that when utilizing a near-infrared fluorophore. In addition, the use of combined holographic and interference filters sets along with a narrow band illumination source, as used herein, reduces the out-of-band signal and the systematic noise level. Owing to the artifacts which impact it, TBR may not be a valid optical imaging metric for elucidating the dose dependent uptake in normal versus diseased tissues.

While we were unable to obtain a consistent dose response from fluorescent intensity and TBR for the reasons written above and elsewhere [8, 78], Figure 4.7 shows that the PK parameter estimate, $\alpha + \beta$ (which contained only the compartment rate parameters as shown in equation (3.15)) produced a consistent dose response. Figure 4.7 shows that $\alpha + \beta$ in the tumor ROI varied linearly with dose from 0.75 nmol to 1.5 nmol, with statistical difference between these amounts indicating unsaturated receptor binding mechanisms. Figure 4.7 also shows that the value $\alpha + \beta$ at the dose of 0.75 nmol of Cy5.5-c(KRGDf) alone is similar to that at 3 nmol dose 1 hour after the injection of 300 or 600 nmol of c(KRGDf). The ultra low dose may result in accumulation and selective compartmentalization to the kidney, spleen, and bladder rather than to tumor region [16]. However, the values of $\alpha + \beta$ remained statistically similar for the 1.5 nmol to 6 nmol doses ($p = 0.25$) in the tumor ROI and for all doses in the normal tissue ROIs ($p = 0.86$), which is indicative of a dose independent response. This dose independent response is consistent with literature reports and may be due to saturated or unavailable receptors for molecular targeting or due to partial self-inhibition at high doses. Chen *et al.* [52]

suggested partial self-inhibition of αvβ3 integrin specific uptake in U87MG at a 3 nmol dose of Cy5.5-c(KRGDf) similar to what they reported for targeting gastrin-releasing peptide receptor using MicroPET techniques [48]. Hagen *et al.* [56] investigated the tissue distribution of the targeted radiotracer, ^{111}In-DTPA-RGD at doses of 0.1 or 0.5 μg administered with and without 100 μg of the unlabeled RGD peptide as a competitive ligand. They showed that the uptake in CA20948 pancreatic tumor was the highest for 0.1 μg ^{111}In-DTPA-RGD. Zitzmann *et al.* [74] showed that RGD-4C-FITC peptide can bind to both endothelial cells and tumor cells in human breast cancer xenografts in nude mouse. Using *in vitro* confocal microscopy, Castel *et al.* [79] showed that RGD peptide targeted to αvβ3 was internalized by integrin-independent, fluid-phase endocytosis pathways in both integrin expressing and non-expressing melanoma cells. They showed that the number of functional integrin receptors at the cell surface remains constant after one hour following incubation with RGD peptide, while it decreased after incubation with monoclonal antibody (mAb 17E6). Furthermore, they demonstrated that high concentrations of RGD peptide may be required to induce apoptosis. Kok *et al.* [80] showed that the *in vitro* specific binding of radiolabeled RGD-protein conjugates to the αvβ3 integrin in H5V endothelial cells seemed to exhibit saturation, but the binding plateau was not reached even at the highest concentrations. However, while these *in vitro* cell culture studies may reflect the binding of integrins on the cancer cells or proliferating endothelium, they do not reflect the combined binding in both vascular and extravascular compartments which occurs *in vivo.*

To relate our *in vivo* dynamic imaging to integrin binding, we developed two distinct models for binding in the vascular compartment associated with proliferating endothelium (Figure 4.1 (a)) as well as the extracellular compartment associated with cancer cells (Figure 4.1 (b)). Conveniently, the solutions for the time-dependent fluorescent intensity from both models are similar and the expressions for $\alpha + \beta$ are exactly the same. Even though it is difficult to relate each PK rate constant to physiologically relevant values, the grouped value of $\alpha + \beta$ allows us to compare the dose dependence among all animals. In contrast to the grouped PK value of $\alpha + \beta$ the pre-exponential factors A and B indicate the magnitude of fluorescence intensities. Each value is higher in tumor region than in normal region in each individual animal (Figure 4.6).

The ability to estimate receptor densities from *in vivo* kinetic uptake analysis of radiopharmaceuticals has been reported. For example, Vera *et al.* [81] measured the receptor concentration, as well as forward and reverse binding rate constants of 99m-galactosyl-neoglycoalbumin with biodistribution data. With dynamic optical imaging, it may be possible to likewise measure the receptor density. Previously, Gurfinkel *et al.* [44] used the PK model of Figure 4.1 (a) to analyze uptake of free Cy5.5, Cy5.5-c(KRGDf) conjugate administered alone as well as with free c(KRGDf) administered as a competitive ligand 1-hour and 24 hours after the injection of Cy5.5-c(KRGDf). They inferred the uptake rate constant owing to integrin binding from differences in Cy5.5-c(KRGDf) uptake with and without c(KRGDf). Those studies did not evaluate the dose response of uptake due to *in vivo* binding. Using a dual-labeled optical and nuclear tracer,

we [55] have embarked on the evaluation of *in vivo* biodistribution data which should provide information for quantifying receptor density. Optical tomography for quantitative 3-D imaging of NIR agents in small animals may overcome not only a requirement for dual labeled probe by providing biodistribution data directly, but also enable molecular imaging of orthotropic tumors. While phantom studies have demonstrated the possibility of optical tomography into deep tissues [82], to date small animal tomography remains under development in several laboratories including our own [83] and must be properly validated before being employed for kinetic analysis for determination of receptor densities.

5. CAN DYNAMIC *IN VIVO* FLUORESCENCE IMAGING ASSESS TISSUE COMPARTMENT OF MOLECULAR TARGET LOCATION?

Although PK analysis in Section 4 shows the uptake rate of Cy5.5-c(KRGDf) to αvβ3 was linearly related to administered dose [8], consistent with a model of unsaturated receptor binding, it did not differentiate between the different compartments of integrin binding, i.e. αvβ3 receptors expressed on tumor cells within the extravascular space and on proliferating endothelial cells within the vascular space. Building upon the results of the previous section, the experimental studies described in this section are intended to examine a second tumor model with known αvβ3 expression on the cancer cells, namely the xenograft of human melanoma (M21), to see if dynamic fluorescence imaging can differentiate between the vascular and extravascular expression of αvβ3 integrin. Kaposi's sarcoma, a frequent cancer in HIV-infected patients, is richly vascularized, characterized by intense angiogenesis, and has high αvβ3 expression in the vascular space [75, 84-86]. However, the cell line M21 is known to highly express αvβ3 on the cancer cells themselves and the tumorigenicity of melanoma is correlated to αvβ3 expression [87-89]. Therefore, PK analysis with dynamic fluorescence imaging is used to differentiate whether the binding of Cy5.5-c(KRGDf) to αvβ3 integrin occurred on either the proliferating endothelium within the vascular space or on the tumor cells within the extravascular space, which may guide the action of therapeutic intervention depending upon the location of the integrin receptor, i.e., anti-angiogenesis in the vascular space or direct cytotoxicity to cancer cells in the extravascular space

5.1 Materials and Methods

5.1.1 Imaging Agents, Tumor Cell Lines, and Animal Models

The synthesis of the fluorescent imaging agents was conducted by Dr. Wei Wang [43]. M21 and KS1767 cells (2-3 × 10^6 / animal) were implanted subcutaneously into the hind region of mice. Four to six week-old female athymic nude mice (nu/nu; 18 –22 g) were purchased from Harlan Sprague Dawley, Inc. (Indianapolis, IN) and housed five per cage and fed sterilized pelleted food (Harlan Sprague Dawley Inc., Indianapolis, IN) and sterilized water. Animals were maintained in a pathogen-free mouse colony in the Department of Veterinary Medicine (The University of Texas M. D. Anderson Cancer Center, Houston, TX) and in the Frensley Center for Imaging Research in the Critical Care Medicine (CCM) (Baylor College of Medicine, Houston, TX). The facilities are accredited by the American Association for Laboratory Animal Care and all experiments were performed in accordance with the guidelines of the respective Institutional Animal Care and Use Committee.

5.1.2 *In vivo* Dynamic Fluorescence Imaging and Experimental Methods

The dynamic fluorescence optical imaging system used in this section is the same as represented in Section 3. Mice were imaged when the tumor size reached approximately 6 to 10 mm in diameter. Prior to imaging and agent administration, mice were anesthetized with Nembutal (Sigma, St. Louis, MO, 50 mg/(kg bw) i.p.), and a tail vein catheter was introduced in each animal. Animals were then placed on the temperature-controlled water circulation pad (Heat Therapy Pump T/Pump®, Model No.

TP-500, Gaymar Industries Inc., Orchard Park, NY) at 37 C under isofluorane anesthesia (VetEquip, Pleasanton, CA and IsoSol Isofluorane USP, VEDCO Inc., St. Joseph, MO). Fluorescence images were acquired for approximately 20 min immediately following i.v. administration of 6 nmol and 3 nmol doses of Cy5.5-c(KRGDf). For competitive binding studies, a 600 nmol dose of unlabeled c(KRGDf) was administered one hour prior to the Cy5.5-c(KRGDf). The animals bearing KS 1767 xenografts received 3 nmol and M21 xenografts bearing animals received 6 nmol of the Cy5.5-c(KRGDf). The CCD integration time was 300-msec for KS1767 and 800-msec for M21 tumor bearing animals.

5.1.3 Data Analysis, Processing and Statistical Methods

The PK models used to analyze dynamic fluorescence images were the same as described in Section 3. Data analysis was accomplished by Matlab software (The MathWorks, Inc., Natick, MA), SigmaPlot software package (SPSS Inc., Chicago, IL), and ImageJ (National Institutes of Health, Washington, DC) after completion of the image acquisition. First, the average of the background images was subtracted from each of the acquired fluorescence images. Tumor and normal region of interests (ROIs) were defined from white light images. The mean of the fluorescence intensity within each ROI in each fluorescence image was then calculated. TBR was calculated by dividing the mean intensity in the tumor ROI by that in the contralateral normal ROI. The mean time-dependent fluorescence intensity profiles were fit by non-linear regression of grouped value in Equation (3.15), and the sum of the parameter estimates $\alpha + \beta$ and TBR were

compared with student t-test SPSS 12.0.1 statistical program (SPSS, Inc., Chicago, Illinois). $p < 0.05$ is considered as significant difference.

5.2 Results

5.2.1 Western Blot

It is important to record cell culture passage number, since tumor cells show different characteristics depending upon passage numbers or types of confluent tissue culture dishes. Although we did not record this information, the western blot analysis at protein level was performed before inoculation of KS1767 and M21 cells into mice to know whether both cells express integrin αvβ3. Figure 5.1 shows that the amount of αvβ3 from both cell lines was almost equal. Therefore, we confirmed that both cancer cell lines expressed αvβ3 integrin equally.

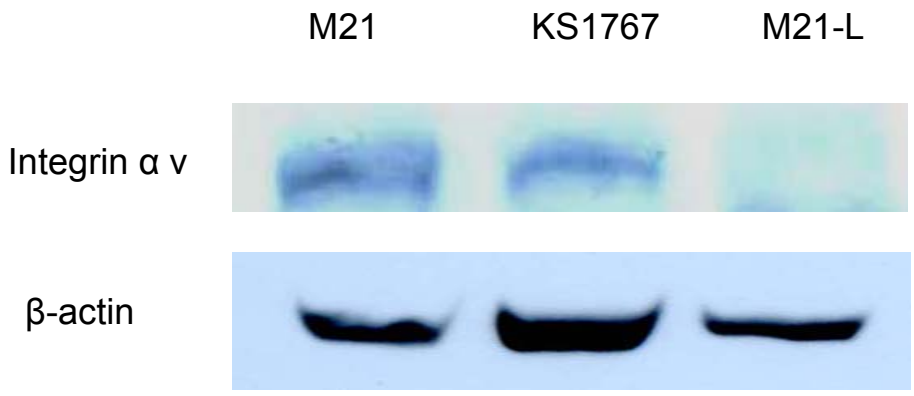

Figure 5.1 Western blot of M21, M21-L, and KS1767 provided by Dr. Shi Ke.

5.2.2 Fluorescence Intensity vs. Time Profiles

Figure 5.2 shows the fluorescence intensity vs. time profiles for tumor and the corresponding contralateral normal tissue ROIs for an example set of animals bearing Kaposi's Sarcoma (Figures 4.2(a) and (b)) and melanoma M21 (Figures 4.2(c) and (d)). The symbols denote the mean fluorescence intensity within the integrated regions after the injection of Cy5.5-c(KRGDf) at doses of 6 nmol (black), 3 nmol (red), and 3 nmol 1 hour after the injection of 600nmol of c(KRGDf) (KS1767; green), or 6 nmol 1 hour after the injection of 600nmol of c(KRGDf) (M21; green). The fluorescence intensity was maximum for the 6 nmol dose of Cy5.5-c(KRGDf) and the lowest for 3 nmol (KS1767) or 6 nmol (M21) dose of Cy5.5-c(KRGDf) 1 hour after the injection of 600 nmol dose of c(KRGDf) in both tumor models. In addition, the fluorescence intensities from tumor ROIs were higher than those from contralateral normal ROIs in all groups. Figure 5.2 also shows a small transient peak in intensity at 7 seconds in the M21 tumor ROI in after the injection of 3 and 6 nmol doses of Cy5.5-c(KRGDf). This small transient peak is neither shown in normal ROIs nor in KS1716 ROIs. Finally, Figure 5.2 shows the results of the least-square fit of the PK model to the fluorescence intensity vs. time profiles in each group. The coefficient of determination R^2 for the regression was 0.99 for KS1767 and 0.95 for M21.

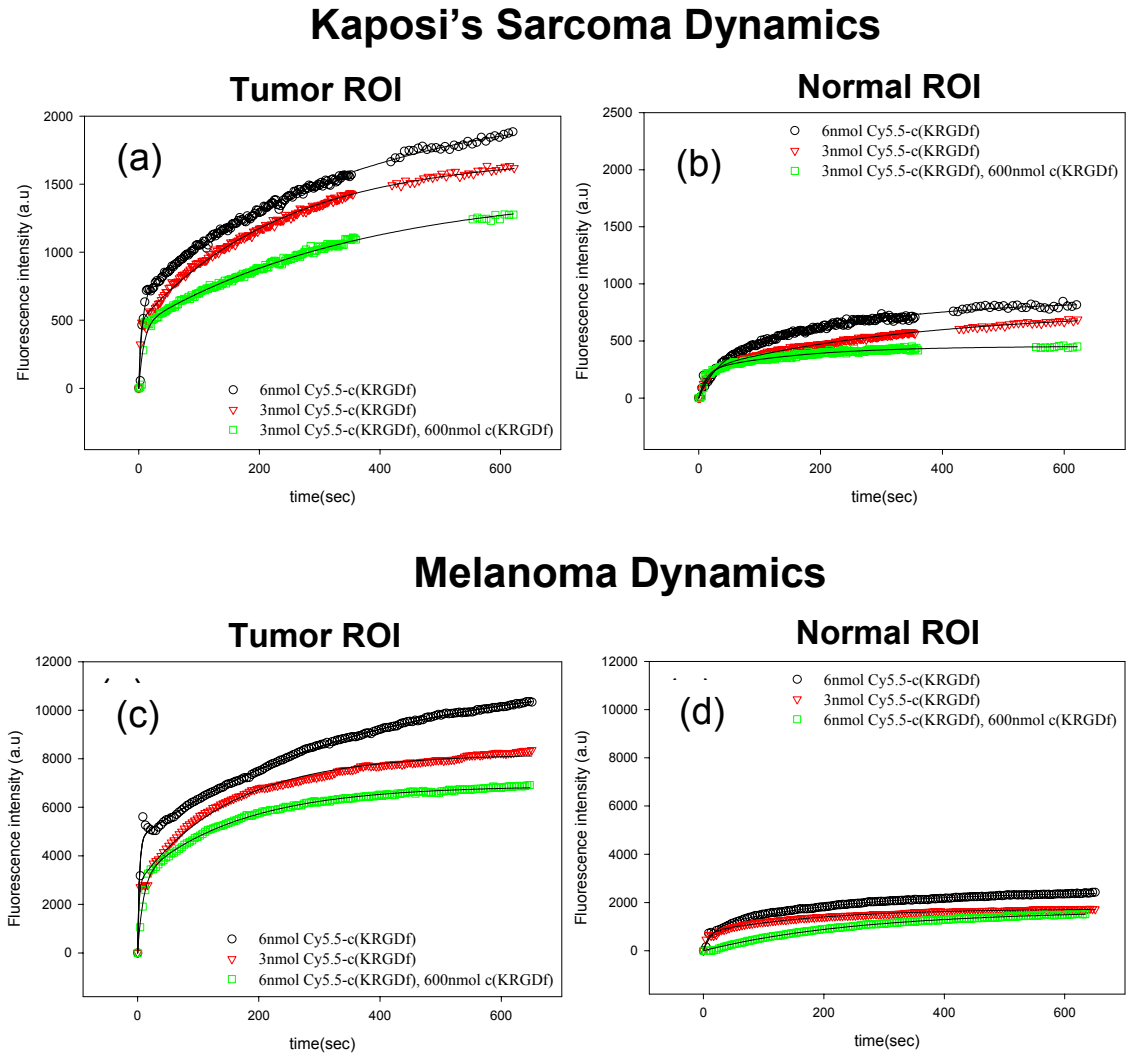

Figure 5.2. Fluorescence intensity vs. time profiles from tumor and normal ROIs in animals bearing KS1767 ((a) and (b))and M21 ((c) and (d)). Animals received an injection of the Cy5.5-c(KRGDf) conjugate at doses of 6 nmol (black), 3 nmol (red), and 3 nmol 1 hour after the injection of 600nmol of c(KRGDf) (KS1767; green), or 6 nmol 1 hour after the injection of 600nmol of c(KRGDf) (M21; green).

5.2.3 Target to Background Ratio

Figure 5.3 shows the histograms of TBR values from xenografts bearing KS1767 and M21 at times of 10 min (black bars) and 24 hours (white bars) after the injection of 3 and 6 nmol of Cy5.5-c(KRGDf) and after injection of unlabeled c(KRGDf) followed one hour later by Cy5.5-c(KRGDf). For KS1767, the values of TBR at 10 min and 24 hours were statistically different from those values measured when c(KRGDf) was administered as a competitive ligand ($p<0.05$). Furthermore, the TBR values in the KS1767 model decreased with time after the injection of 3 and 6 nmol of Cy5.5-c(KRGDf) ($p<0.05$). Perhaps indicative of the enhanced permeability associated with anti-angiogenesis action of RGD, the TBR values computed from images acquired 10 min after the injection of 3 nmol dose of Cy5.5-c(KRGDf) with pre-administration of 600 nmol dose of c(KRGDf) were higher than the TBR values computed from images 10 minutes after 300 nmol dose of c(KRGDf) ($p<0.05$). In contrast to the KS1767 model, Figure 5.3 shows there were no significant differences between the TBR values in the M21 model even when unlabeled c(KRGDf) was administered one hour before Cy5.5-c(KRGDf) as a competitive ligand.

(a)

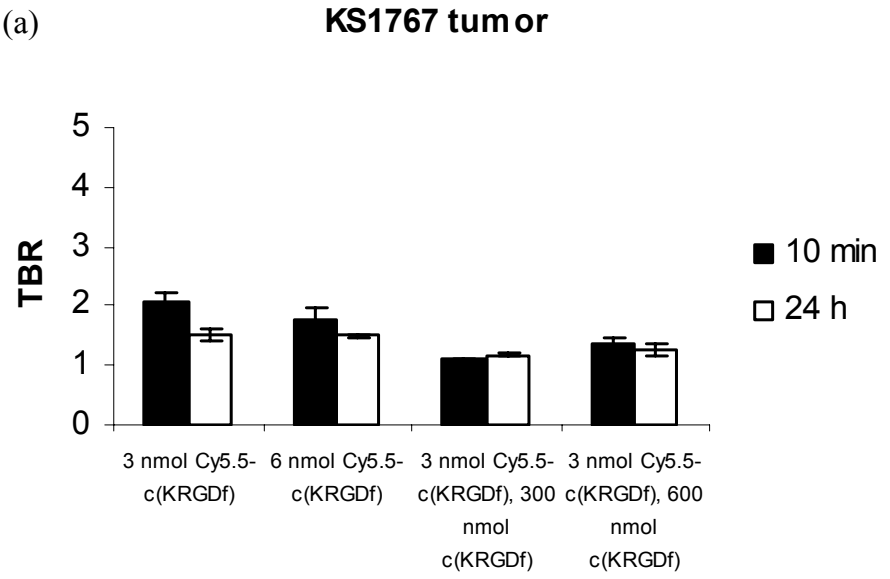

(b)

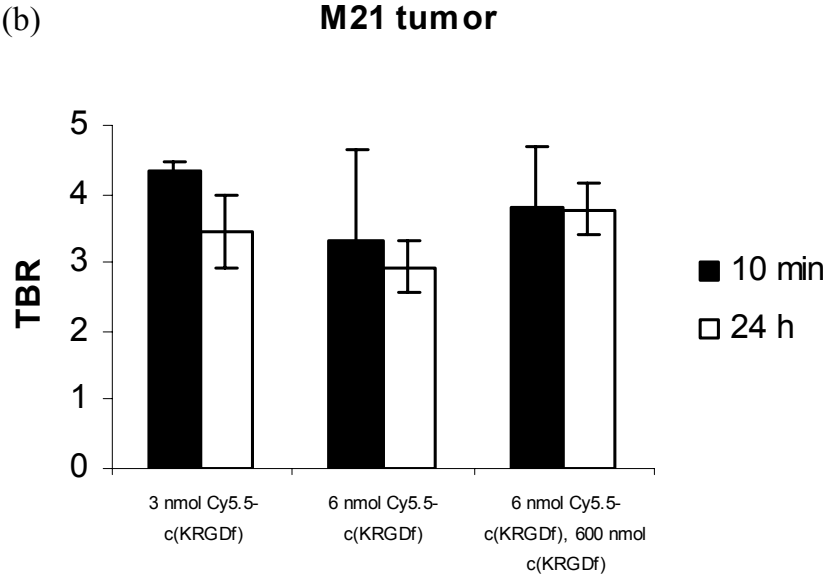

Figure 5.3 Tumor to background ratio (TBR). The filled and unfilled columns denote mean value of each test group 10 min and 24 hour after the injection of the Cy5.5-c(KRGDf), respectively, and the error bars represent the standard deviation.

5.2.4 Pharmacokinetic Analysis

Figure 5.4 illustrates the sum of the parameter estimates of $\alpha + \beta$ obtained from regression of fluorescence intensity vs. time profiles within tumor (black bars) and normal (white bars) ROIs. The values of $\alpha + \beta$ in tumor ROIs from xenografts bearing KS1767 injected with 3 and 6 nmol doses of Cy5.5-c(KRGDf) are statistically different from those in corresponding normal ROIs in KS1767 ($p<0.001$) except when 600 nmol of c(KRGDf) was pre-administered as a competitive ligand. In contrast, PK values of $\alpha + \beta$ in tumor ROIs and contralateral normal ROIs from xenografts bearing M21 are not significantly different among all test groups. Finally, there is no significant difference of PK values of $\alpha + \beta$ in the normal tissue ROIs across all doses regardless of whether pre-administration of unlabelled c(KRGDf) occurred.

5.3 Discussion

Since the interstitial diffusion coefficient and microvascular permeability of small molecules (MW<2000) is almost equal in normal and neoplastic tissue [43], the uptake of peptide tracers in tumor region would not be expected to benefit from enhanced permeability and retention (EPR) effect. Additionally, peptides targeting markers expressed in the vascular space do not need to diffuse into the extravascular space [58].

In this study, we demonstrated dynamic fluorescence imaging and early-time PK data for 20 mins after agent delivery to compare the differences in tumor biology of human Kaposi's sarcoma (KS1767), a cancer of the vasculature characterized by intense angiogenesis, and a human melanoma tumor line (M21) known to express integrin $\alpha v\beta 3$.

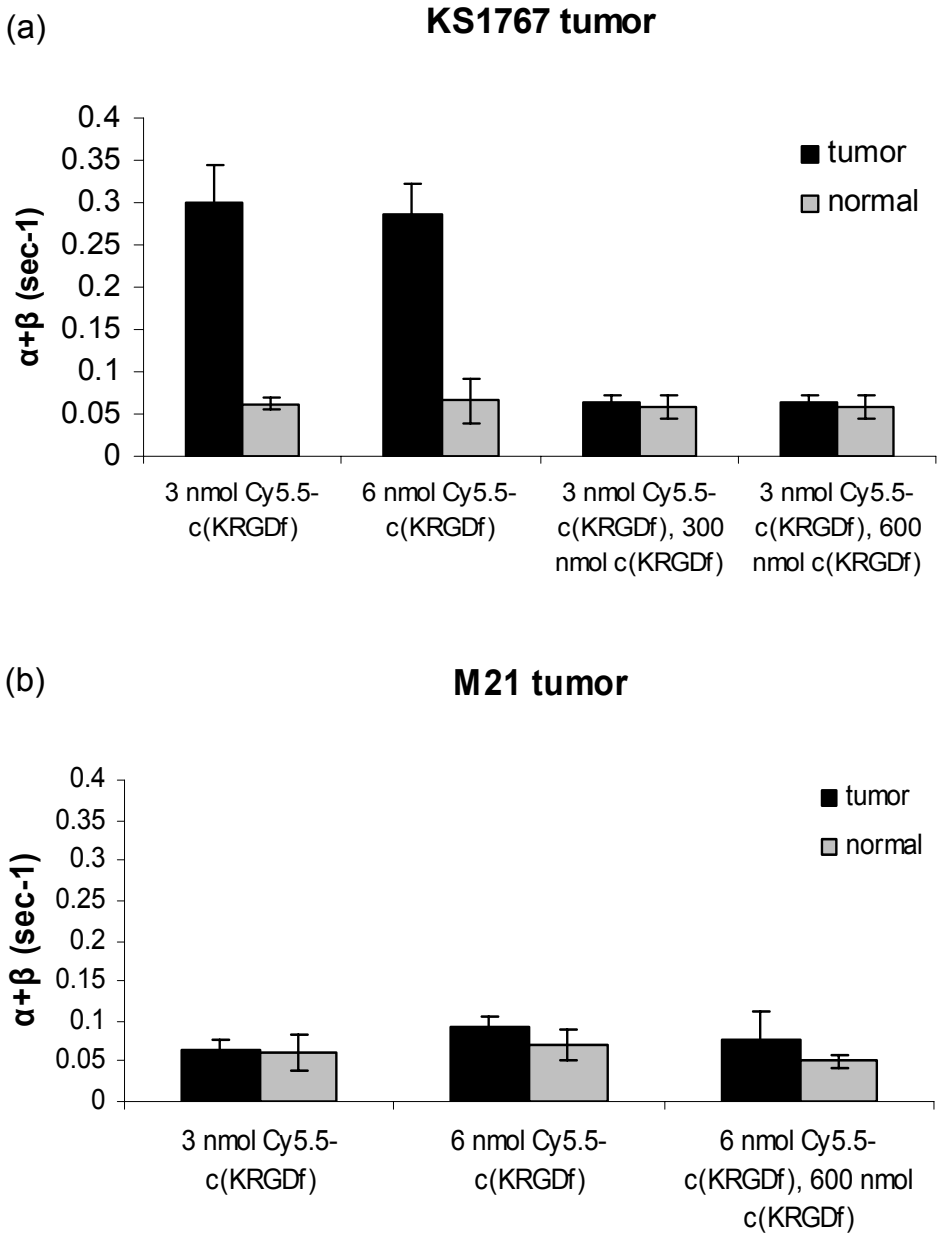

Figure 5.4 The sum of the PK constant α and β in the tumor (black columns) and normal (gray columns) ROIs. The column height represents the mean value of the test group and the error bars represent the standard deviation.

KS1767 and M21 cell lines express comparable levels of the integrin αvβ3 receptor as shown in Figure 5.1, but when grown as a the xenograft model or found within patients, the integrin expression may occur in potentially different tissue compartments: (i) on the proliferating endothelium within the vascular space, and/or (ii) on the surface of cancer cells in the extravascular space. While Kaposi sarcoma is a vascular cancer and integrin expression should be predominantly located in the vascular space, the M21 melanoma xenograft model may require host - cell signaling to induce angiogenesis. Consequently, while M21 cells express αvβ3, the vascular integrin expression in the xenografted M21 model may approach that of normal epithelium. As shown by Beer *et al.* [14], αvβ3 was highly expressed on tumor cells in melanoma patients with lymph node and cutaneous metastasis, while microvessel densities (MVD) were low in those tumors.

The αvβ3 receptors in the vascular space are readily available for Cy5.5-c(KRGDf) targeting and for competitive binding with c(KRGDf) following i.v. administration. On the other hand, the proportion of αvβ3 receptors on the cancer cells within the extravascular space may require longer time for extravasation, suggesting that early-time pharmacokinetics may not provide sufficient information on receptor availability on the M21 cancer cells. Furthermore, extravascular receptors may not be adequately saturated by free c(KRGDf) after one hour and if they are, early time pharmacokinetics of Cy5.5-c(KRGDf) may again not be sufficient to report extravascular receptor availabilities.

While used by other investigators to assess specificity of targeting agents [40], we previously found that the TBR generally has large error bars and does not track changes in receptor availabilities as dynamic fluorescence imaging does as discussed in Section 3 [8]. Specifically, the measurement of TBR is impacted by excitation light leakage through interference and holographic filters which can vary depending upon incident excitation illumination levels [78]. Nonetheless, we find that in the KS1767 tumor model, TBR is reduced with the pre-administration of c(KRGDf) as a competitive ligand one hour before administration of the imaging agent. In contrast within the M21 model, pre-administration of c(KRGDf) does not lead to a reduction in the TBR, consistent with extravascular expression of the αvβ3 target. The results for early-time PK uptake parameter are consistent with TBR results. In the KS1767 tumor model, the pre-administration of c(KRGDf) prior to imaging agent administration reduces the uptake rate to levels that occur in the contralateral normal tissues while in the M21 tumor model, there is no significant difference. Indeed, the uptake rates in M21 tissue ROIs are comparable to those in all contralateral normal tissue ROIs, suggesting that the availability of integrin receptors probed in early PK analysis in the M21 model is similar to that in normal tissues.

While the early-time PK analyses may reflect the availability of vascular integrin receptors, the time delay between administration of c(KRGDf) as a competitive ligand and the imaging agent may also impact whether vascular or extravascular integrin receptors are accessible and the clearance rates of c(KRGDf). For example, depending upon several factors (molecular size of competitive ligand and imaging agent, interstitial

pressure, and vessel permeability [90]) the time for saturation of extravascular integrin receptors following administration of competitive ligand may be longer than 1 hour. Indeed, using TBR analysis alone, it was noted that the blocking of αvβ3 integrin was the most effective 8 hours after the pre-administration of c(KRGDf) in M21 tumors.

Vessel permeability may be an important feature to image in monitoring response to angiogenesis therapy. EPR is a slow process, and significant uptake of targeting agent often needs several hours [91]. However, DeNardo *et al.* [92] showed that the αvβ3 integrin may be a target for transiently increasing permeability of tumor vessels for increasing tumor uptake of radiolabeled monoclonal antibody (MAb) in radioimmunotherapy. Cyclic RGD peptide (250 ug i.p.) provided 1 hr before 111-In-ChL6 MAb* resulted in a 40 to 50 % increase in tumor uptake, when compared to the control tumor uptake, of MAb 24 hr after administration. When cyclic RGD peptide was given as a continuous infusion (17.5 ug/hr) for 1 or 24 hr before 111-In-ChL6, tumor uptake of targeting agent was increased less. In KS1767 xenograft model, we found that the TBR from images acquired at 10 min after the injection of a 3 nmol dose of Cy5.5-c(KRGDf) with pre-administration of 600 nmol of c(KRGDf) was higher than that resulting from 300 nmol of c(KRGDf) ($p<0.05$), possibly indicating non-specific binding due to increased permeability (Figure 5.3(a)), since the early uptake parameters are not different. The higher fluorescence intensity in tumor ROI may result from transiently increased permeability due to the apoptosis of endothelial cells.

* ChL6: a mouse-human chimeric antibody in which a mouse constant domains of murine L6 were substituted with human IgG1 constant domains

As pointed out in the introduction, dynamic imaging of integrin receptors is clinically relevant, since action of integrin based therapies differs depending upon the location of the integrin receptor, i.e., anti-angiogenesis in the vascular space or direct cytotoxicity to cancer cells in the extravascular space. The investigation of therapeutic effects of integrin based therapy may not be fully understood from xenograft studies owing to host-cell interaction. Consequently, the staging of integrin therapy used as an adjuvant to chemotherapy or radiation [93] depends upon understanding the modes of interaction and the tissue compartment of the disease marker used as a therapeutic target. With the conjugation of integrin targeting moieties with near-infrared dyes, the opportunity to diagnostically monitor response to therapy in skin and superficial vascular cancers such as melanoma and Kaposi's sarcoma with dynamic fluorescence imaging is directly possible.

6. COMPARISON OF *IN VIVO* FLUORESCENCE IMAGING WITH NEAR INFRARED AND RED LIGHT EXCITABLE FLUORESCENT CONTRAST AGENTS

In Sections 4 and 5, PK analysis of dynamic CW fluorescence imaging was used to evaluate the uptake of a novel targeting agent, Cy5.5-c(KRGDf) into integrin αvβ3 positive tumors. Typically, free Cy5.5 in phosphate buffered saline is excited at 673 nm and the resulting fluorescence is collected at 692 nm [94]. In this thesis a 660 nm laser diode was used to excite Cy5.5 and a bandpass filter of 710 nm to transmit fluorescence emission was employed to provide a sufficient Stokes shift. However, there is significant autofluorescence in background tissues at red light (~700 nm) excitation which can significantly decrease the target to background ratio in whole body imaging [41]. IRDye800 or Indocyanine green (ICG) as a NIR dyes are excited at 785 nm and the emitted fluorescence collected at 830 nm. The use of NIR excitable fluorescent dyes reduces autofluorescence and promotes deep tissue penetration for preclinical, small animal imaging, and should do the same in future clinical trials.

The work presented in this section was performed as part of a collaborative effort. Animal care and preparation of fluorescent contrast agents were performed by our collaborators at Baylor College of Medicine who are recognized in the Acknowledgments of this thesis, while the fluorescence imaging and data analysis were performed entirely by the author. The experimental studies in this section compared whole animal fluorescence imaging with NIR and red light excitable fluorescent dyes.

6.1 Introduction

The epidermal growth factor receptor (EGFR) is a transmembrane glycoprotein that contributes to the regulation of cell growth, differentiation, apoptosis, and angiogenesis. EGFR is overexpressed in many solid tumors as summarized in Table 6.1, resulting in tumor angiogenesis and tumor growth. Therefore the detection of EGFR may help to determine an optimal strategy for cancer treatment. Most EGFR imaging has been performed using nuclear imaging as described in Table 6.2. Targeting agents such as antibodies against EGFR and its natural ligand, epidermal growth factor (EGF), have been labeled with a number of radionuclides. These studies showed that tumor visualization as well as TBR depended upon the sizes of the targeting agents. For example, although tumors were easily visualized with radiolabeled antibody (more than 4 hr after initial administration of radiolabeled agents), higher TBRs were observed with radionuclide labeled EGF [95, 96].

Table 6.1 EGFR density for A431, MDA-MB-468, MDA-MB-231, JW-97, MCF-7, $C6_{EGFR}$ glioma, and Normal hepatocytes tumor cells.

Tumor cell line	Number of receptors per cell
A431	2×10^6 [97]
MDA-MB-468	3×10^5 [97]; 1.3×10^6 [95]
MDA-MB-231	1.3×10^5 [95]
JW-97	2.7×10^5 [95]
MCF-7	5×10^3 [97]; 1.5×10^4 [95]
$C6_{EGFR}$ glioma	$10^5 \times 10^6$ [98]
Normal hepatocytes	8×10^4 to 3×10^5 [95]

Table 6.2 Imaging of epidermal growth factor (EGFR) or EGFR tyrosine-kinase.

	Imaging modality and agent	Dosage for imaging	Imaging period	Animal model and Cell line	Targeting location	Tumor uptake	comments
Ortu *et al.* [99]	PET Irreversible inhibitors of [^{11}C]ML03	i.v., 100-200 μCi	1 hr after injection of agent	rats A431	EGFr-TK	0.09 %id/g 15 min after injection	Low accumulation of [^{11}C]ML03 in the tumor and non specific binding in blocking study
Bonasera *et al.*	PET Reversible inhibitors of ^{18}[F]1 and ^{18}[F]4	i.v., 10-20 μCi	1 hr after injection of agent	mouse A431	EGFr-TK	^{18}[F]1: 1.34 %id/g 1 hr after injection; ^{18}[F]4: 2.83 %id/g 10 min after injection	Blocking time point is 10 min, but no decrease in radioactivity
Goldenberg *et al.* [97]	Gamma-camera imaging ^{111}In-DTPA-C225 MAb and ^{111}In-DTPA-KS1/4S-1	i.p., 230 μg (290 μCi) to A431 and 85 μg (105 μCi) to MDA-MB-436 xenografts	3 and 6 days after injection	mouse A431, MDA-MB-468, and MCF-7	EGFR	For A431 xenografts, 28 %id/g and 12.4 %id/g 3 and 7 days after injection, respectively; for MDA-MB-468 xenografts, 4.2 %id/g 8 days after injection	Localization of imaging agents depended on EGFR expression and non-specific binding was also shown
Divgi *et al.* [100]	Gamma-camera imaging and SPECT ^{111}In-DTPA-MAb 225	Infusion, Ranging from 4 to 300 mg of labeled MAb	three days after injection	human (phase I) Patients with squamous cell lung cancer	EGFR	3.4 %id/g 72 hrs after injection of 120 mg of labeled MAb	Toxicity was not observed when patients received up to 300 mg of MAb, and primary tumor could be imaged at doses of 20 mg or greater in dose-dependent manner
Wen [101]	Gamma-camera imaging ^{111}In-DTPA-PEG-C225 and ^{111}In-DTPA-C225	i.v., 10 μg; for blocking: 1 mg of C225 30 mins or 20 hrs before 10 μg of imaging agent	up to 48 hrs, however radioactivity in tumors reached at 24 hrs after injection	mouse MDA-MB-468, MDA-MB-435, and A431	EGFR	1:30 ^{111}In-DTPA-PEG-C225: 8.68 %id/g; 1 mg of C225 30 min before injection of ^{111}In-DTPA-PEG-C225: 13.85 %id/g	Imaging agent reduced the non specific liver uptake, which resulted in improved tumor visualization, while tumor uptake of radiotracer was not significantly reduced after pre-injection of C225

Table 6.2 Continued.

	Imaging modality and agent	Dosage for imaging	Imaging period	Animal model and Cell line	Targeting location	Tumor uptake	comments
Schechter [102]	SPECT ^{99m}Tc-EC-C225 and ^{99m}Tc-EC	i.v., 0.05mg (22 mCi) to human; 10 10 µg to rat	for biodistribution: 4 hrs; for imaging: 6 hrs	mouse, rat, and human For mouse and human: A431; for rat: 13762NF; for human:	EGFR	With ^{99mc}Tc-EC-C225 and ^{99mc}Tc-EC in 113762NF, 0.416 %id/g and 0.342 %id/g 30 min after injection, respectively	Biodistribution showed that tumor uptake of ^{99mc}Tc-EC-C225 was highest 30min after injection of imaging agent, and primary tumor but not nodal sites was visualized at 2 hr post-injection of imaging agent
Meenakshi [103]	Gamma camera imaging ^{99m}Tc-CIBCNSH3	i.v., 200 µCi	up to 24 hrs	mouse A431 and SUDHLH	EGFR	For A431 and SUDHLH, 12.15 and 0.2 %id/g 24 hr after injection	The results showed specific selective uptake of their agent by tumor with low uptake in other organs
Iznage-Escobar [104]	Gamma camera imaging ^{99m}Tc-moAb ior egf/r3	i.v., 30.3±11.9mCi (1 mg MAb) and 39.5 ±1.1mCi (3 mg MAb)	Up to 24 hr	human (phase I/II) Epithelial derived tumors	EGFR	N/A	Binding of imaging agent was dose-independent and that there was rapid clearance of radioactivity by renal and hepatobiliary excretion (87 %) 3 hr after injection of their agent
Ramos-Suzarte [105]	Gamma camera imaging and SPECT ^{99m}Tc-moAb ior egf/r3	i.v., 3 mg (50mCi, 1.85 GBq)	up to 24 hrs for gamma camera; 5 hrs after injection	human (phase I/II) Epithelial derived tumors	EGFR	N/A	Detected primary tumors as well as metastases with low amounts of imaging agents
Onn [106]	CT	N/A	N/A	human (72 patients) stage I non-small cell lung cancer (NSCLC)	EGFR and HER2	N/A	EGFR overexpression and cavitation in squamous cell carcinoma was found more than that in adenocarcinoma, and patients with NSCLC with cavitation had a worse prognosis

Table 6.2 Continued.

	Imaging modality and agent	Dosage for imaging	Imaging period	Animal model and Cell line	Targeting location	Tumor uptake	comments
Abdel-Nabi [107]	CT and SPECT ^{111}In-CYT 103	i.v. infusion, 4.1 mCi (152 MBq) of ^{111}In-CYT 103 at doses of 0.5 to 20 mg	2 to 7 days after infusion of imaging agent	human (28 patients, phase I/II) Colorectal carcinoma	EGFR	N/A	Tumor was detected at doses of 1 mg or higher, and pre-administration of 18 mg of unlabeled CYT 103 1 hr before injection of 2 mg of imaging agent did not cause a decrease in radioactivity uptake in normal liver tissue
Yang [98]	Gamma camera imaging ^{99m}Tc-EGF	i.c. or i.v., 31 to 43 μCi (1.7 to 2.3 μg)	4 and 24 hr after injection	rat EGFR gene transfected C6 rat glioma and C6 wildtype tumor	EGFR	From biodistribution, 0.34 and 0.45 %id/g 4 hr after i.c. injection with and without BBB-D, respectively, and 0.14 %id/g 4 hr after i.v. injection; from gamma scintigraphic images, 1.73, 2.80, and 2.94 counts/pixel 4 hr after i.v., i.c., and i.c. with BBB-D injection, respectively.	For brain tumor model, they showed i.c. injection is better than i.v. injection, but hperosmotic BBB-D did not improve tumor uptake of their imaging agent
Rusckowski [96]	Gamma camera imaging and autoradiography ^{99m}Tc-EGF, ^{99m}Tc-anti-EGFR IgG, and ^{99mc}Tc-BPTI	i.v., 34-50 μg (300 μCi) for ^{99mc}Tc-EGF; 8 μg (200 μCi) for ^{99mc}Tc-anti-EGFR IgG; 200 μg of unlabeled EGF 4 hr before injection of ^{99mc}Tc-EGF	12 or 18 hr after injection	mouse A431 and LS174T	EGFR	From biodistribution of ^{99mc}Tc-EGF, 0.40 (A431), 0.32 (LS174T), and 0.29 (preadministration of unlabeled EGF 4 hr before injection to xenografts bearing A431) %id/g in tumor thigh 18 hr after injection; from biodistribution of ^{99mc}Tc-anti-EGFR IgG, 0.65 %id/g 18 hr after injection	They showed that (i) more favorable tumor to normal tissue ratios with ^{99mc}Tc-EGF compared to ^{99mc}Tc-anti-EGFR IgG, (ii) similar accumulation of ^{99mc}Tc-EGF in both tumor models, although LS174T has lower expression of EGFR, and (iii) highest accumulation of ^{99mc}Tc-EGF in the kidneys. In addition, they showed that there was no significant difference in the accumulation between ^{99m}Tc-EGF and ^{99m}Tc-anti-EGFR IgG in tumor.
Schatten [108]	CT and US ^{123}I-EGF	s.c. into web space of each foot, 370 MBq/mg (50 μg)	Up to 24 hr after injection	human (14 patients with stage III/IV) Advanced cervical cancer	EGFR	N/A	CT and US confirmed nodal involvement for 4 and 2 patients of the 11 positive ^{123}I-EGF scan and target to non-target ratios were highest 6-8 hr after injection

Table 6.2 Continued.

	Imaging modality and agent	Dosage for imaging	Imaging period	Animal model and Cell line	Targeting location	Tumor uptake	comments
Reilly [95]	Gamma camera imaging ^{111}In-DTPA-MAb 528 and ^{111}In-DTPA-hEGF	i.v., 1.85-3.7 MBq ^{111}In-DTPA-hEGF (0.5-1μg) or ^{111}In-DTPA-MAb 528 (25-50 μg)	72 hr after injection	mouse MCF-7, MDA-MB-231, JW-97, and MDA-MB-468	EGFR	2.2 and 0.4 %id/g 72 hr after injection of ^{111}In-DTPA-hEGF with and without co-administration of unlabeled 500 μg hEGF, and 21.6 %id/g 24 hr after injection of ^{111}In-DTPA-MAb 528	They showed that (i) tumors were more easily visualized with ^{111}In-DTPA-MAb 528, while higher tumor to blood ratios were observed with the ^{111}In-DTPA-hEGF, (ii) no direct quantitative relationship between the level of receptors measured *in vitro* and the level of tumor uptake *in vivo* was not found, and (iii) tumor uptake *in vivo* is mostly controlled by elimination rate from the blood than by the expression level of receptor on cells.
Dadparvar [109]	Gamma camera and SPECT ^{111}In-EGFR 425, ^{111}In-Co17-1A, and ^{111}In-chloride	i.v., 2 to 2.2mCi	24 and 48 hr after injection	Human (28 patients) glioma	EGFR	N/A	They showed that the uptake of ^{111}In-EGFR 425 did not correlate with prognostic significance. In addition, they showed non-specific binding of ^{111}In-Co17-1A and ^{111}In-chloride, and low specificity of ^{111}In-EGFR 425 in glioma
Kalofonos [110]	Gamma camera imaging ^{131}I-H17E2 and ^{123}I-EGFR1 MAb	10 mCi	Up to 48 hr after injection	Human (27 patients) glioma	EGFR and PLAP	0.0009-0.0057 %id/g with specific antibody and 0.00018-0.00465 %id/g with non-specific antibody	They showed the localization of ^{131}I-H17E2 and ^{123}I-EGFR1 MAb in glioma tumor region. However, the difference in accumulation between specific and non-specific antibody in the tumor was small.
Vallis [111]	Gamma camera imaging and SPECT ^{99m}Tc-hR3	i.v., 3 or 6 mg (1010 MBq, 27mCi)	Up to 24 hr after injection	Human (12 patients) Epithelial derived carcinomas	EGFR	N/A	They found that (i) immunocytochemical staining of tumor biopsies for EGFR positivity did not predict positive tumor imaging, (ii) the increase in circulating radioactivity due to catabolism of ^{99mc}Tc-hR3 in tissue, and (iii) high accumulation in the liver and kidney, suggesting increasing the dosage of ^{99mc}Tc-hR3

Table 6.2 Continued.

	Imaging modality and agent	Dosage for imaging	Imaging period	Animal model and Cell line	Targeting location	Tumor uptake	comments
Lee *et al*. [112]	Gamma camera, ^{111}In-native 528 MAb, ^{111}In-cationized 528 MAb, and ^{111}In-PEG-cationized 528 MAb	i.v., 50 μCi	24 hr after injection	mouse U87	EGFR	N/A	They showed that the pegylation did not reverse the serum inhibition of the cationic charge on the MAb and that that radiolabeling a cationized MAb with DTPA produces a serum neutralization of the initial cationization modification
Cornelissen [113]	Gamma camera imaging ^{99m}Tc-HYNIC-hEGF	i.v., 3.7 MBq (1 μg) for imaging; 100 μg of unlabeled hEGF for displacement experiment	2 hr after injection	mouse LoVo cells	EGFR: for response to farnesyltransferase inhibitor (FTI) therapy	TBRs were 1.1 and 2.5 at 2 hr post-injection of ^{99m}Tc-HYNIC-hEGF with or without unlabeled hEGF, respectively; TBRs for untreated animals with FTI and 6 hr after administration of FTI were 2.6 and 1.1, respectively	They showed that (i) coinjection of unlabeled hEGF and blocking with MAb88910 decreased the tumor to normal tissue ratios to 1.1 and 1.2, respectively. In addition, they showed therapy response of FTI inhibitor, e.g., 100 mg/kg R115777
Vinter-Jensen [114]	Gamma camera imaging ^{131}I-EGF	Jugular i.v., 10 nmol (3.4-4.7 MBq/kg)	2 hr after injection	pig	EGFR	N/A	The uptake in the liver was the highest at 6-8 min after injection and remained at a plateau for 10 min before it declined. The time activity curve in the kidneys peaked after 3-5 min with a short plateau, and then declined
Ke [115]	Optical imaging Cy5.5-EGF, ICG, and Cy5.5	1 nmol of ICG , 2.9 nmol of Cy5.5, 1 nmol of EGF-Cy5.5 , and blocking study, 1.9 mg of C225 (12.7 nmol)	up to 192 hr after injection of imaging agent	mouse MDA-MB-468 and MDA-MB-435	EGFR	N/A	They showed that ICG and Cy5.5 did not bind to both tumors, while Cy5.5-EGF accumulated only in MDA-MB-468 tumors. Tumor uptake of Cy5.5-EGF was blocked by C225.

There are no correlation between in the imaging agents and the *in vitro* receptor densities [95]. It may indicate that tumor uptake *in vivo* is mostly controlled by elimination rate of imaging agents from the blood than by the expression level of receptor on cells. Recently, polyethylene glycol (PEG) as a linker between monoclonal antibody against EGFR and chelator has been employed to reduce liver uptake, which resulted in improved detection of EGFR-positive tumors [101].

Most standard nuclear imaging studies have shown static images, including information about tracer distribution and receptor densities. Recently EGFR positive tumors were visualized in whole body fluorescence imaging using Cy5.5 conjugated with EGF [115]. They showed dynamic measurement of fluorescence intensities for the first 20 min after tail vein injection. With high sensitivity and sub-second camera exposure time, dynamic whole-body imaging should be useful to differentiate tumors from normal tissue regions, and to monitor the real-time distribution of the imaging agents. In the studies, there was significant autofluorescence at 660 nm excitation, which can significantly decrease TBR and may reduce the image quality as previously discussed. Reducing the background autofluorescence should enhance the TBR, improving tumor detection and providing more information about therapeutic efficacy and tumor physiology during the uptake and washout phases. In order to investigate the impact of autofluorescence during dynamic imaging, we labeled EGF with two fluorescent dyes, a near-infrared fluorescence dye, IRDy800, and a red light excitable fluorescence dye, Cy5.5. Fluorescence images of each animal were compared before and after injection of either the NIR or the red fluorescent conjugate. We qualitatively compared the

background signals of an animal positioned next to a vial filled with 10 pmol of each fluorescent conjugate in 200 μl of normal saline.

6.2 Materials and Methods

6.2.1 Tumor Cell Lines and Animal Models

Human breast cancer cell line MDA-MB-468, positive for the epidermal growth factor receptor (EGFR), was purchased from American Type Culture Collection (Manassas, VA). The cells were cultured in DMEM/F12 (Invitrogen, Carlsbad, CA) with 10% FBS (Hyclone, Logan, UT) in a humidified incubator maintained at 37^{o}C with 5% CO_2. Four week old nude mice were purchased from Harlan (Indianapolis, IN). When the MDA-MB-468 cells reached 95% confluence, they were treated with trypsin, washed with PBS, and resuspended at $1x10^6$ cells per 100 μl PBS. Each mouse was injected subcutaneously with $1x10^6$ cells in the right flank. Palpable tumors of size 4 to 6 mm in diameter developed within 3 to 4 weeks.

6.2.2 Fluorescent Dye Conjugates

Epidermal growth factor (EGF) from mouse submaxillary glands was purchased from Invitrogen (Carlsbad, CA) and resuspended at 200 μg/ml in 0.1M sodium bicarbonate buffer pH 8.5. Cy5.5-NHS ester was obtained from GE Healthcare, formerly Amersham Pharmacia Biotech, (Piscataway, NJ) and resuspended in DMSO at 10mg/ml. IR800-NHS ester was obtained from Licor Biosciences (Lincon, NE) and resuspended in Methanol at 10mg/ml. EGF was reacted with Cy5.5-NHS or IR800-NHS in a 1:5 protein

to dye molar ratio for 1 hour at room temperature with shaking. Free dye was removed by size exclusion chromatography on a 10DG desalting column (Biorad, Hercules, CA).

6.2.3 Fluorescence Imaging System

A laser diode of 785 nm for IRDye800 excitation was added to the dynamic fluorescence optical imaging system described in Section 3. Both laser diode excitation sources (785-nm, 85-mW for IRDye800; 660-nm, 35-mW for Cy5.5) were operated at 85 mA for IRDye800 and 65 mA for Cy5.5, and expanded uniformly with a plano-convex lens and diffuser to approximately 8-cm diameter area for illumination of the whole body of a mouse. A holographic notch-plus band-rejection filter (660-nm center wavelength for Cy5.5, OD at λ_x reported to be > 6, 785-nm center wavelength for IRDye800, OD at λ_x reported to be > 6; Kaiser Optical Systems Inc., Ann Arbor, MI) and a bandpass filter (830-nm center wavelength for IRDy800, OD at λ_x reported to be > 4, 710-nm center wavelength for Cy5.5 OD at λ_x reported to be 3; CVI Laser Corporation, Albuquerque, NM) were fitted with the 50-mm lens to reject back-scattered and reflected excitation light and select fluorescence emission light. White light images were taken with a low-power lamp after all filters were removed.

6.2.4 *In vivo* Fluorescence Imaging

Before administration of the imaging agent, animals were placed on a temperature-controlled heat pad (Spin System, Australia) at 37 C under isofluorane anesthesia (VetEquip, Pleasanton, CA and IsoSol Isofluorane USP, VEDCO Inc., St.

Joseph, MO) and a catheter was inserted into the tail vein. All fluorescent images were acquired with 800 msec integration time, so the intensities from each image could be compared during analysis [8]. Intensifier gain was varied from 40% of the maximum gain for white light images to 95% of the maximum gain for fluorescence images. After taking white light images, 0.2 ml of either Cy5.5-EGF or IRDye800-EGF (1 nmol equivalent Cy5.5 and IRDye800 per mouse) was injected via the tail vein catheter. Two groups of control mice received 0.2 ml of Cy5.5 (1 nmol per mouse) and IRDye800 (1 nmol per mouse). In addition, one group of mice was pre-administered with C225, an EGFR antibody, at a dose of 1.9 mg (12.7 nmol per mouse) 24 hr before injection of 0.2 ml of IRDye800-EGF (1 nmol per mouse). Fluorescence images were obtained every 1.1 seconds for approximately 40 min with IRDye800, IRDye800-EGF, and IRDye800-EGF with pre-administration of C225 and 20 min with Cy5.5 and Cy5.5-EGF. Fluorescence images were taken up to 48 hr following initial injection of contrast agent. Six fluorescence images serve as "background" images prior to bolus administration of the imaging agent. Additionally, fluorescence images of an unmanipulated animal next to a vial containing 10 pmol of either Cy5.5-EGF or IRDye800-EGF in 200 μl of normal saline was taken to quantitatively measure autofluorescence background.

6.2.5 Data Processing and Statistics

After acquiring the images with V++ software (Digital Optics, Auckland, New Zealand), data analysis and processing were accomplished by Matlab software (The MathWorks, Inc., Natick, MA), SigmaPlot software package (SPSS Inc., Chicago, IL),

and ImageJ (National Institutes of Health, Washington, DC). Using white light images, two regions of interest (ROI), (i) the tumor for target ROI and (ii) the contralateral normal tissue region for background ROI, were defined, each having the same numerical surface area. The mean fluorescence intensity for each ROI in each fluorescence image was plotted as a function of time. TBR was calculated by dividing the mean intensity in the tumor ROI by that in the contralateral normal ROI. In addition, using fluorescence images, the chest, kidney, and head regions were defined as target ROIs, and the stomach as the background ROI. The statistical analysis was performed with SPSS 12.0.1 statistical program (SPSS, Inc., Chicago, Illinois). The differences were considered significant at $p < 0.05$.

6.3 Results

6.3.1 Autofluorescence

Figure 6.1 illustrates side by side comparison of conjugate free, unmanipulated animals illuminated with 660 nm (Figure 6.1 (a)) and 785 nm (Figure 6.1 (b)) light with a vial of 10 pmol of either EGF-IRDye800 or EGF-Cy5.5 for reference. The autofluorescence signals in NIR image (Figure 6.1 (b)) are significantly lower than from red fluorescent dye (Figure 6.1 (a)).

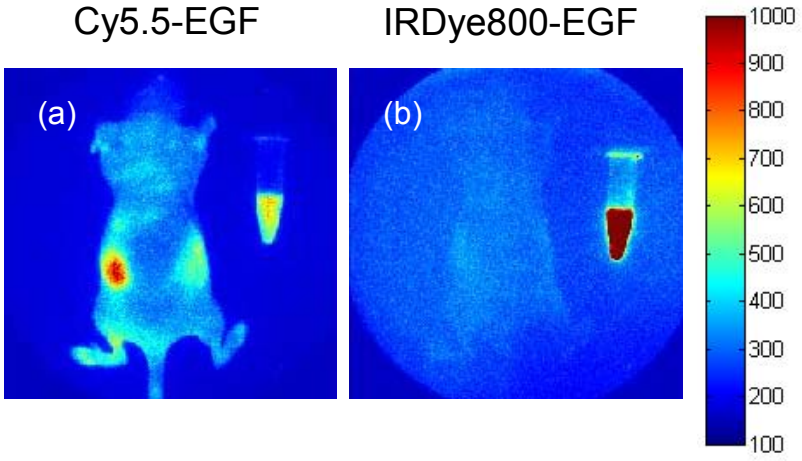

Figure 6.1 Comparison of autofluorescence in two different dye conjugates. Mice that have not been injected with any dye are next to a tube containing 10 pmol of Cy5.5-EGF (a) or IRDye800-EGF (b) in 200 µl of saline.

6.3.2 Dynamic Fluorescence Intensity vs. Time Profiles

Figure 6.2 displays an example of the normalized fluorescence intensities as a function of time from MDA-MB-468 tumor and contralateral normal tissue ROIs for 40 min after administration of IRDye800-EGF, IRDye800, and IRDye800-EGF 24 hr after injection of C225, and 20 min after administration of Cy5.5-EGF and Cy5.5. The tumor sizes in all animals studied in this experiment are ~ 6 mm in diameter, except one animal (12 mm in diameter), shown in Figure 6.2 (b). Figure 6.2 shows that the fluorescence intensities in the tumor ROIs increased more quickly than those in normal tissue ROIs after injection of IRDye800-EGF (Figure 6.2 (a) and (b)) and Cy5.5-EGF (Figure 6.2 (e)). The intensities in the tumor ROIs of mice injected with IRDye800 continually increased for 21 min, plateaued for 10 min, and then decreased to that of normal tissue ROIs as shown in Figure 6.2 (c).

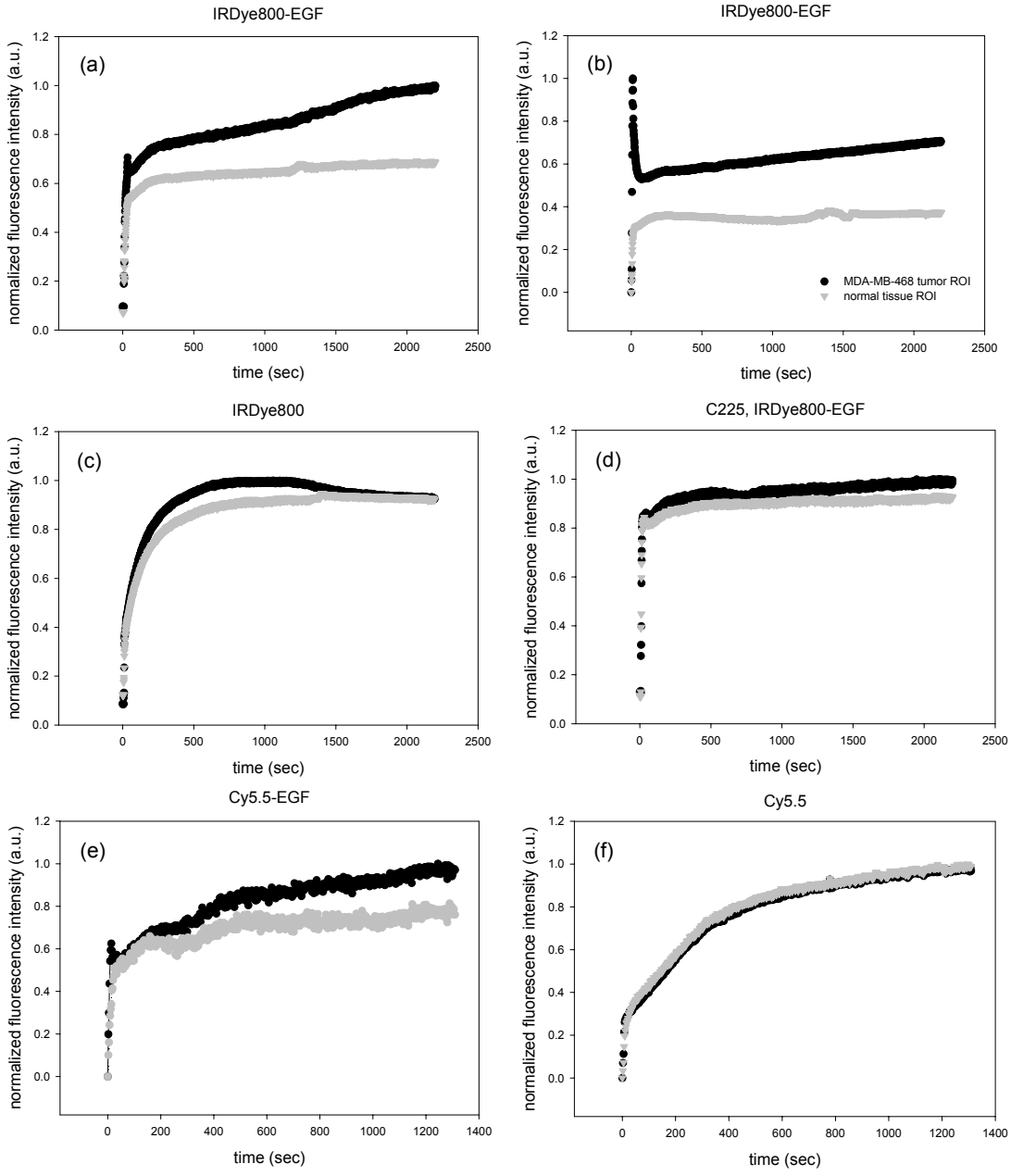

Figure 6.2 Normalized fluorescence intensity vs. time profiles from xenografts of MDA-MB-468 that received an injection of the (a) and (b) IRDye800-EGF, (c) IRDye800, (d) IRDye800-EGF 24 hr after administration of C225, (e) Cy5.5-EGF, and (f) Cy5.5 at 1 nmol in 200 µl of normal saline, acquired from the tumor (black) and normal (gray) ROIs.

In mice injected with Cy5.5, the fluorescence intensities for tumor and normal tissue ROIs were similar (Figure 6.2 (f)). In mice pre-administered with C225, the normalized fluorescence intensities from the tumor ROIs were reduced (Figure 6.2 (d)). The fluorescence intensities in tumor and normal tissue ROIs from MDA-MB-468 xenograft bearing mice after injection of Cy5.5-EGF or Cy5.5 were similar to our previous results [115]. A bolus peak in the fluorescence intensity profiles around 5.5 sec after injection of IRDye800-EGF or Cy5.5-EGF is also shown in Figure 6.2.

6.3.3 *In vivo* Fluorescence Imaging

Due to the sensitivity of our home-built fluorescence imaging system, we can image real-time circulation of small quantities of fluorescent conjugates throughout a live mouse. Figure 6.3 shows posterior white light and fluorescence images from one representative of each experimental group, displayed every 1.1 seconds for a period of approximately 7.7 seconds following initial injection of IRDye800 (first column), IRDye800-EGF administered without (second column) or with (third column) C225, and Cy5.5-EGF (forth column). All fluorescence images are illustrated on the same linear color scale to allow for a direct qualitative comparison. There was no autofluorescence from animals before injection of NIR fluoresce at 785 nm excitation as shown in Figure 6.3. There was, however, autofluorescence in stomach and gastrointestinal regions at 660 nm excitation before injection of red light excitable dyes.

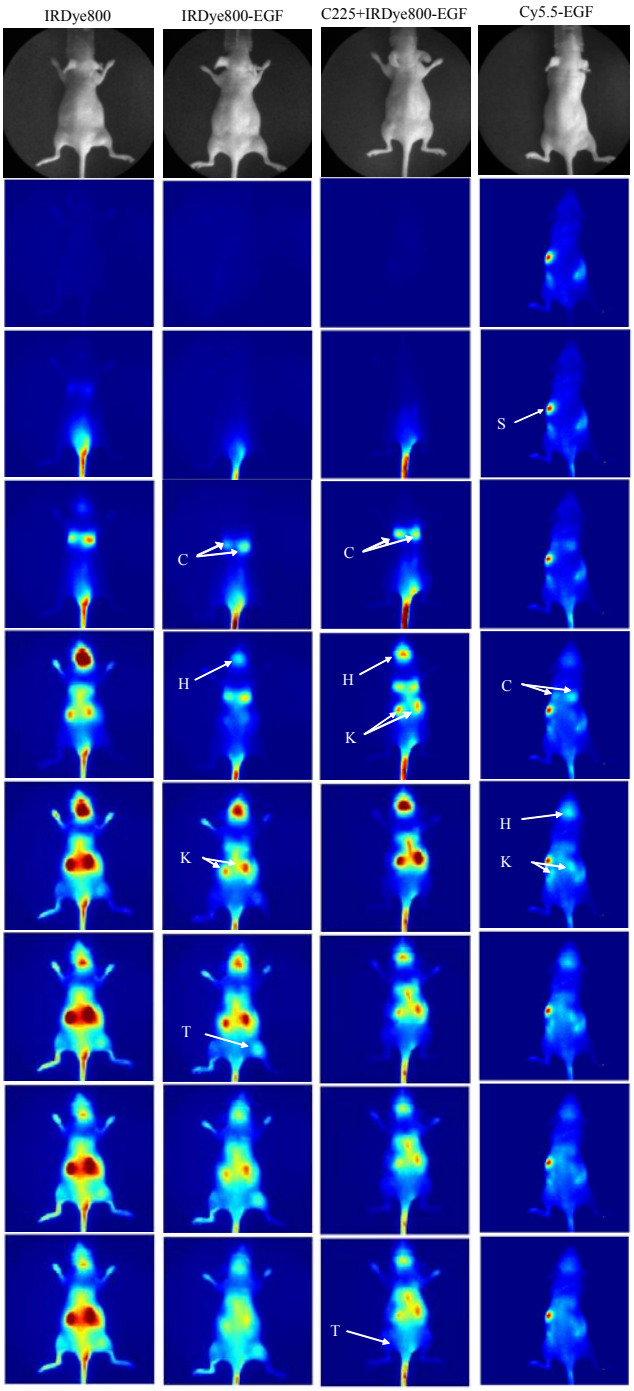

Figure 6.3 Dynamic fluorescence images immediately following injection of IRDye800 (first column), IRDye800-EGF (second column), IRDye800-EGF 24 hr after administration of C225 (third column), and Cy5.5-EGF (fourth column) at 1 nmol in 200 μl of normal saline for ~7.7 sec. C: chest, S: stomach, H: head, K: Kidney, and T: tumor.

Immediately after injection of NIR fluorescence dyes via a tail vein catheter, fluorescence signal was detected from the tail. Subsequently, the chest, kidneys, head regions were clearly seen with the interval of 1.1 sec. Moreover, the tumor was detected from 4.4 sec after injection of IRDye800-EGF and IRDye800 as shown in Figure 6.3. At 7.7 seconds after initial injection of the conjugate the whole body of a mouse became bright. In order to demonstrate the *in vivo* binding specificity of the IRDye800-EGF, fluorescence imaging was performed immediately after injection of 1 nmol dose of IRDye800-EGF but 24 hr after administration of 1.9 mg of native C225. Figure 6.3 shows that the tumor regions had little or no detectable fluorescence above the normal region after pre-administration of C225. The fluorescence images from MDA-MB-468 xenografts injected with Cy5.5-EGF showed limited ability to detect real-time spatial distribution of imaging agents due to the high level of autofluorescence as shown in Figure 6.3.

Figure 6.4 displays TBRs calculated using the animals' chest, kidneys, and head areas as target ROIs, and dividing their mean fluorescence intensities by that of the stomach area, which was set as the background ROI. The TBR values were computed at 7.7 seconds after injection of 1 nmol (in 0.2 ml volume) of IRDye800-EGF and Cy5.5-EGF (n=3 for each test group). Figure 6.4 shows that all the time dependent TBR values from IRDye800-EGF injections were higher than those of Cy5.5-EGF, because of high background signals from the abdomen area at 660 nm excitation.

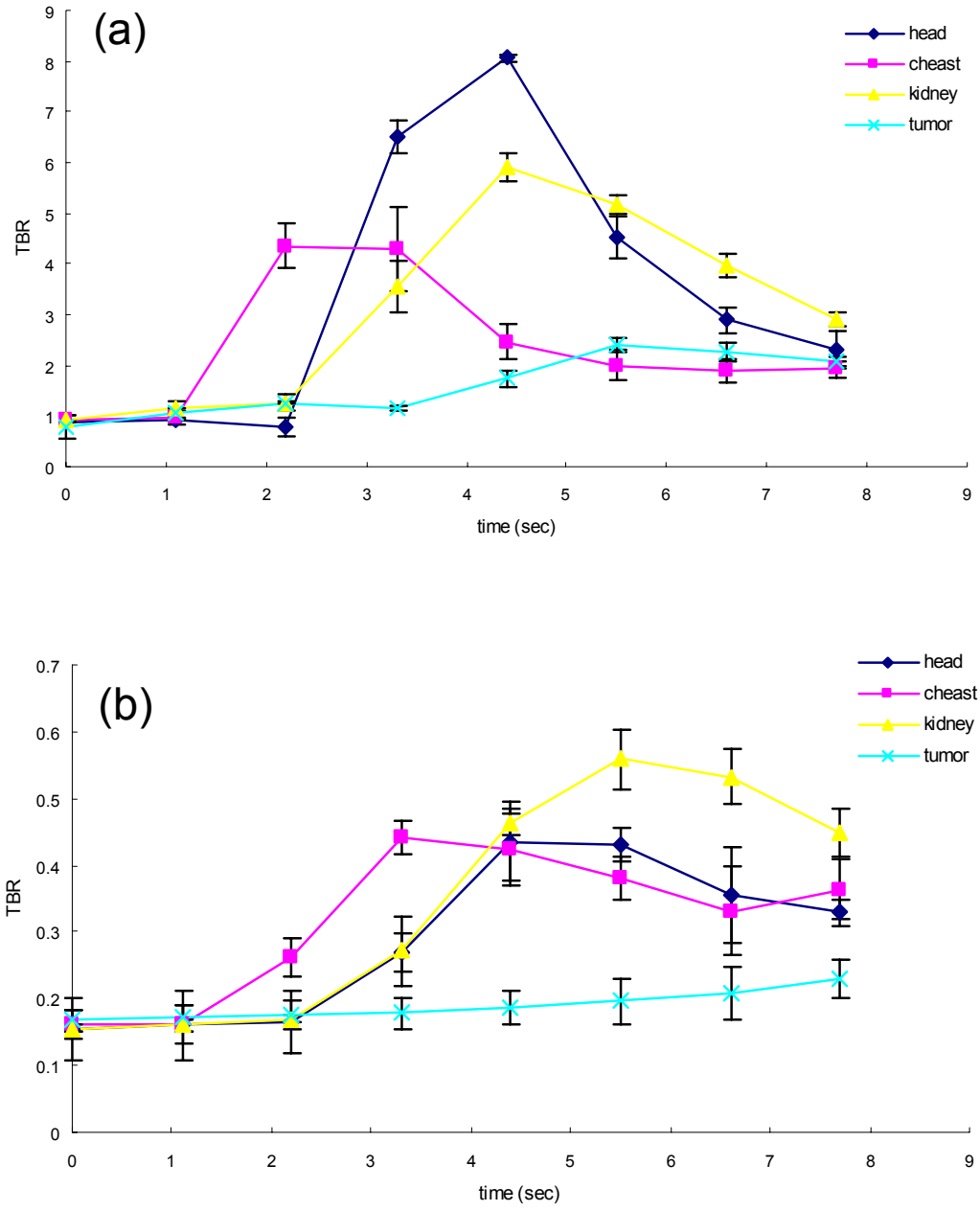

Figure 6.4 The ratio of head, chest, kidneys, and tumor ROIs to stomach background ROIs as a function of time in animals injected with 1 nmol of IRDye800-EGF (a) and Cy5.5-EGF (b) for 8 sec. Error bars represent the standard deviation.

Fluorescence imaging was also conducted 24 and 48 hours after initial injection of imaging agent. Fluorescence images of dissected organs from a xenograft bearing MDA-MB-468 tumors 48 hr after injection of 1 nmol of IRDye800-EGF, IRDye800, and IRDye800-EGF 24 hr after administration of C225 are shown in Figure 6.5. The tumor was detected from the fluorescence images after administration of IRDye800-EGF alone (Figure 6.5 (a) and (b)), while the tumor was not clearly detectable in fluorescence images 24 and 48 hr after injection of IRDye800 (Figure 6.5 (d) and (e)) and IRDye800-EGF with pre-administration of 1.9 mg of native C225 (Figure 6.5 (g) and (h)). In addition to the tumor from animals injected with IRDye800-EGF, the liver and kidneys also showed strong fluorescence signal (Figure 6.5 (c)). The fluorescence signal originating from the liver, kidneys, and tumor in animals injected with IRDye800 (Figure 6.5 (f)) or IRDye800-EGF 24 hr after administration of C225 (Figure 6.5 (i)) was significantly reduced.

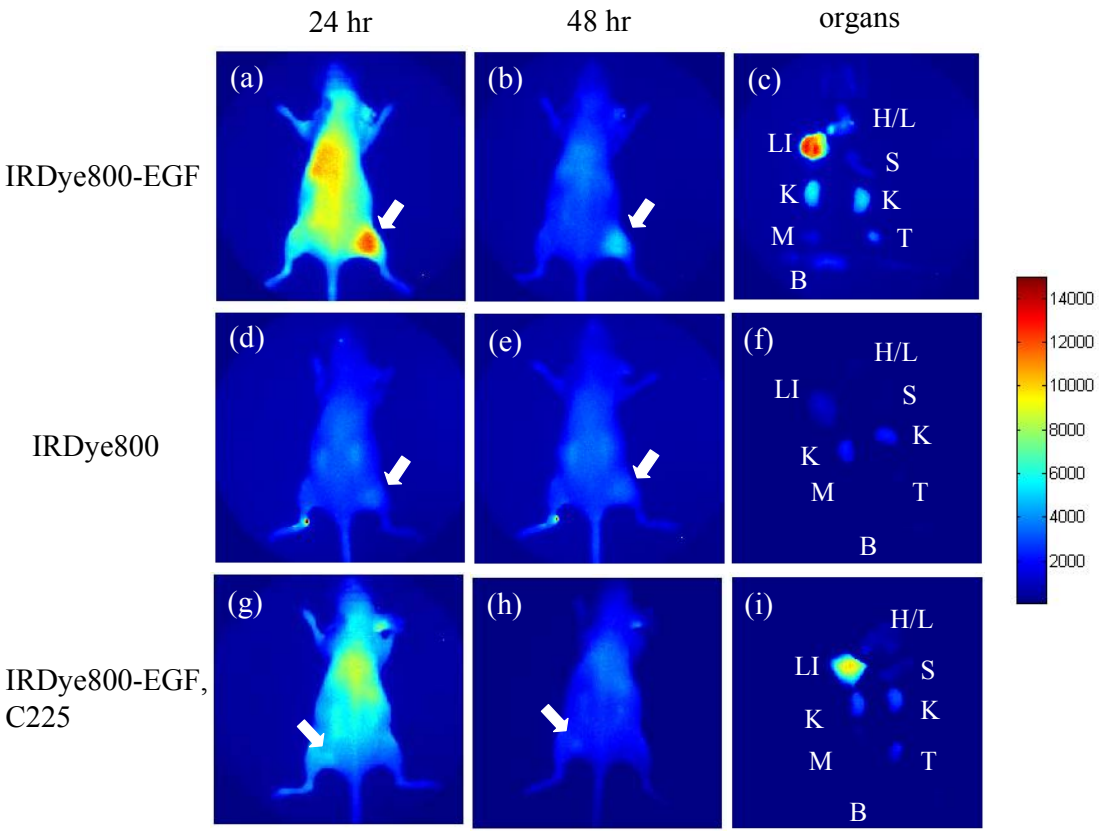

Figure 6.5 Whole-body fluorescence images of animals at 24 and 48 hr after the administration of 1 nmol of IRDye800-EGF (first row), IRDye800 (second row), and IRDye800-EGF 24 hr after administration of C225 (third row), and fluorescence images of dissected organs from a xenograft bearing MDA-MB-468 tumor 48 hr after injection of contrast agents. H/L: heart/lung, LI: liver, S: spleen, K: kidney, M: muscle, T: tumor, and B: blood.

In mice injected with Cy5.5-EGF, the tumor was also detectable 24 hr after initial injection (Figure 6.6). By removing the mouse skin around tumor and normal ROIs, a better image of the tumor with higher TBR (Figure 6.7) resulted due to reduced autofluorescence from the skin and increased fluorescence signal in the tumor ROI probably due to removal of signal attenuation in the skin ($p<0.05$).

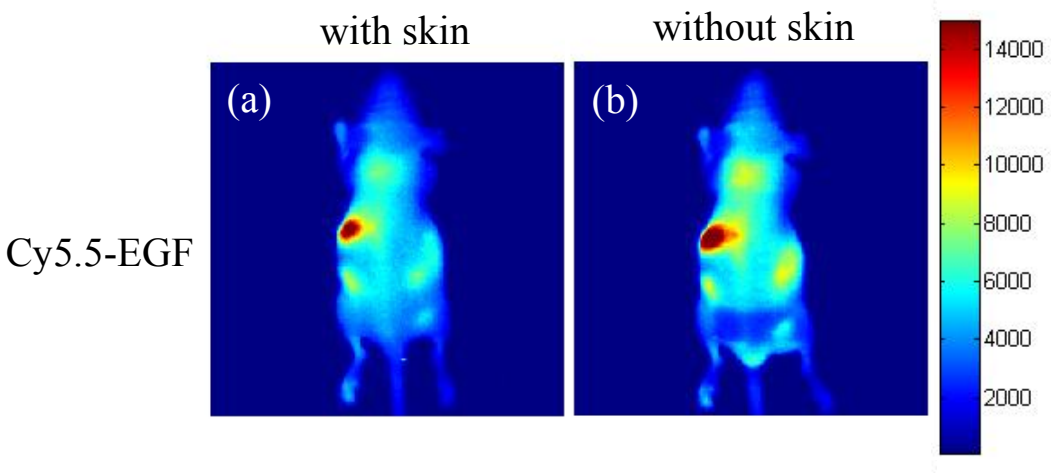

Figure 6.6 Fluorescence images of animals with and without skin in tumor and normal ROIs 24 hours after the administration of 1 nmol of Cy5.5-EGF.

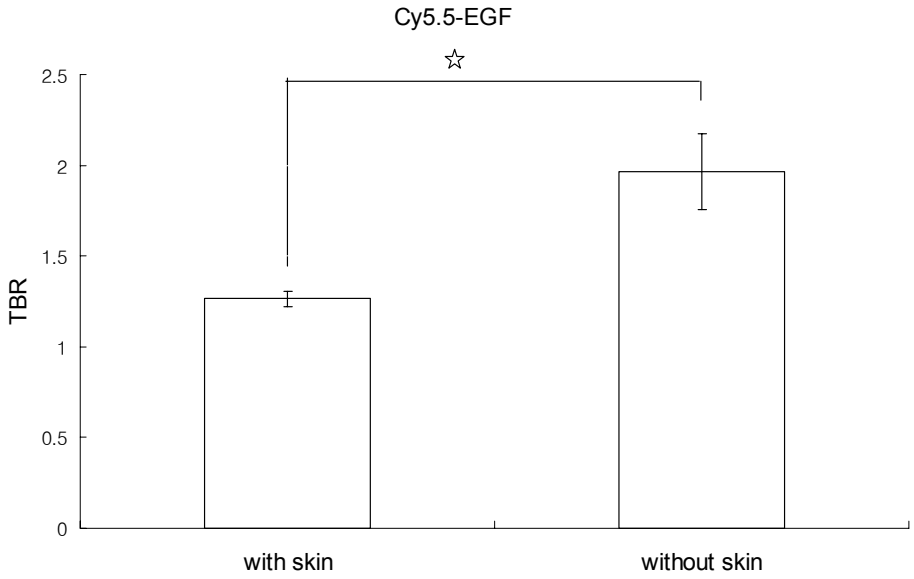

Figure 6.7 The ratio of tumor ROI to normal tissue ROI's intensities from animals with and without skin in tumor and normal ROIs at 24 hr after injection of 1 nmol of Cy5.5-EGF. The error bars represent the standard deviation and ☆ denotes the statistical significance.

Figure 6.8 shows the TBR for three groups of animals after the injection of IRDye800, IRDye800-EGF, and IRDye800-EGF after pre-administration of C225 (n=3) at different time points after administration. The background TBRs before administration of fluorescent agents were similar. However, the TBR at 40 min and 24 hr after injection of IRDye800-EGF is statistically different from that of animals injected with IRDye800 and IRDye800-EGF after injection of C225 ($p<0.05$).

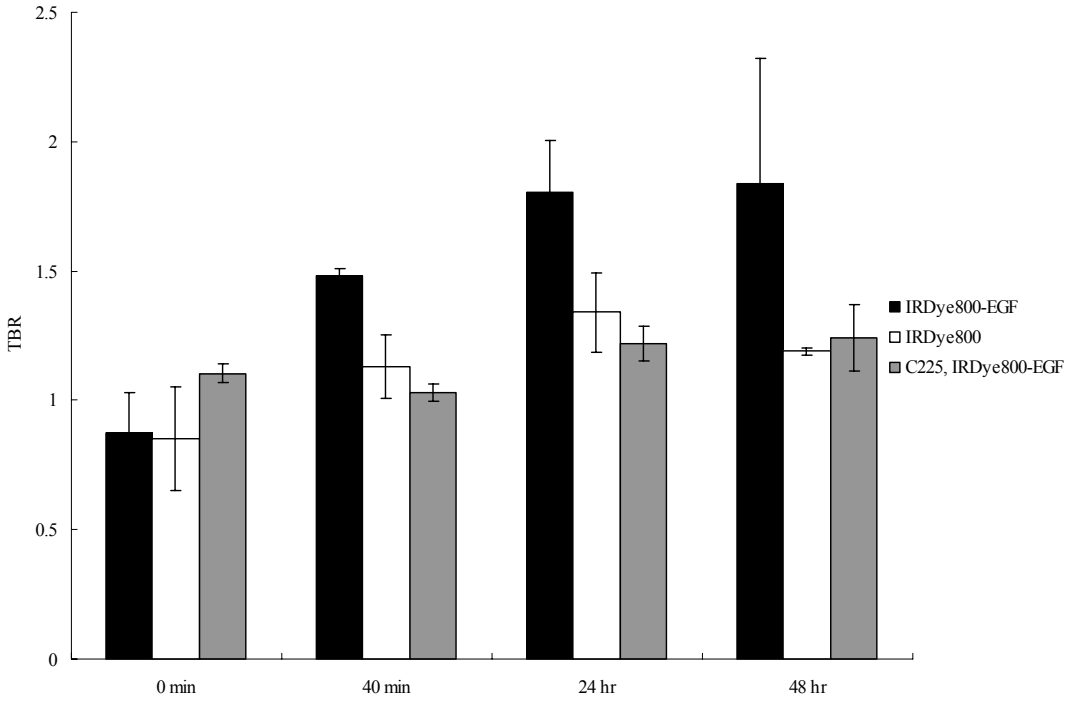

Figure 6.8 The ratio of the tumor to normal ROI intensities in MDA-MB-468 xenografts after injection of IRDye800-EGF (black column), IRDye800 (white column), and IRDye800-EGF with pre-administration of C225 antibody (gray column) at different time points. The points represent the mean value of the test group and the error bars the standard deviation.

6.4 Discussion

In this study, we demonstrated the advantages of dynamic fluorescence imaging to determine the spatial distribution of small quantities of NIR fluorescent contrast agents through the whole body of xenografts bearing MDA-MB-468 tumors for a short period of time. Dynamic imaging using targeting or non-specific agents has the potential for the study of delineation between normal and diseased tissues and of transient disease marker expression in tumor physiology resulting from cancer treatment. In addition, dynamic imaging might help screen drugs and optimize treatment procedure. Berard *et al.* [116] demonstrated dynamic PET imaging collecting one image every 60 sec for 2 hr to monitor transient metabolic processes and to investigate the mechanisms of photosensitizing drugs in the photo-dynamic therapy (PDT) of cancer. The ^{18}F-FDG time–activity curves showed distinct transient patterns during PDT. In our dynamic fluorescence imaging, the CCD exposure time is 800 msec, which enables near real-time *in vivo* fluorescence imaging. As shown in Figure 6.2, dynamic measurement of fluorescence intensities clearly showed different uptake in the first 40 min after injection of contrast agents. The rates of uptake of IRDye800-EGF and Cy5.5-EGF were significantly greater and faster in tumor ROIs than in contralateral normal tissue ROIs. However, the signals in tumor ROIs in animals injected with IRDye800 and IRDye800-EGF with pre-administration of CC5 antibody were similar to those in normal tissue ROIs.

Dynamic fluorescence imaging can be used to differentiate animals with different tumor stages. Fluorescence intensities in animals with larger tumors, i.e. > 12 mm in

diameter show higher peak at ~ 5.5 sec after initial injection of IRDye800-EGF (Figure 6.2 (b)) and slower uptake as compared to smaller tumors, possibly due to vascular permeability difference and highly elevated IFP resulting from tumor mass. Elevated IFP may reduce extravasation of the contrast agents causing the binding to occur over a longer time if the agent remains in circulation. Fluorescence intensities in tumor ROIs after injection of non-specific agent, IRDye800, increased for 21 min, plateaued for 10 min, and then decreased to the intensity level of normal tissue ROIs. The relatively increased fluorescence intensities in tumor ROIs over normal ROIs in the same animal may also be due to increased permeability in the leaky vasculature in tumor regions. Vascular permeability increases in tumors, which facilitates leakage of i.v. administered drugs into the surrounding tissue. Previously, it was reported that ICG and fluorescein angiograms could be used to assess cancerous regions due to different permeability levels [117-119]. However, fluorescence intensities did not differ between tumor and normal ROIs in mice injected with Cy5.5. In mice injected with IRDye800-EGF 24 hr after administration of C225, the fluorescence intensity profiles between tumor and normal ROIs were similar, which might result from reduced availability of EGFR.

Dynamic fluorescence images correlated well with the fluorescence intensity profiles. There was little or no autofluorescence from animals before injection of IRDye800-EGF or IRDye800 at 785 nm excitation. This enabled the detection of the spatial distribution of agent in the chest, head, and kidney regions every 1.1 sec immediately following a tail vein injection of NIR fluorescent agents as shown in Figure 6.3. The liver and bladder were also detected from anterior view. Interestingly, the

tumor was readily detected around 4.4 sec after injection of IRDye800-EGF and IRDye800 (Figure 6.3) at the same time the bolus peak in fluorescence intensities appeared in Figure 6.2. However, tumors were not detected in images of animals bearing MDA-MB-468 injected with IRDye800-EGF 24 hr after pre-administration of C225. Not yet proven, we hypothesize that tumor detection after administration of IRDye800-EGF and IRDye800 mainly resulted from increased permeability in tumor vasculature allowing dye entry into the tumor. Therefore, no visualization of tumors after pre-administration of C225 might result from decreased permeability and reduced availability of EGFR, indicating C225 as an anti-angiogenic therapeutic agent. Similarly, Izumi *et al.* [120] demonstrated that tumor blood vessels after herceptin (antibody against EGFR-2) treatment resemble a normal phenotype, resulting in reduced vascular permeability in tumor vasculature. In addition, C225 has been used to treat EGFR negative colorectal cancer patients [121], indicating the role of C225 as indirect anti-angiogenic therapeutics. Although it is difficult to verify whether tumor detection is only due to increased permeability or binding of the agent to EGFR, for a short time after injection of the contrast agents, dynamic fluorescence imaging may provide more quantitative information using PK models [8].

For red light excitable fluorescent dyes, Cy5.5-EGF autofluorescence at 660 nm increased the background signals deteriorating the image quality during dynamic imaging (Figure 6.3). The level of autofluorescence light from excitation at 660 nm & emission at 710 nm was greater than that of 10 pmol of Cy5.5-EGF (Figure 6.1). Therefore, an

adequate dose for molecular dynamic imaging at this wavelength must be above the threshold, e.g., to overcome the background autofluorescence.

Light generated by fluorescent imaging agents within tissue must propagate to the surface for collection through appropriate filters onto an area imaging device. Three characteristics impact the sensitivity of imaging agents *in vivo*: (i) the camera/detection sensitivity [122], (ii) excitation light leakage [78], and (iii) background autofluorescence [122-124]. Our experiments show that the ICCD camera system can detect small quantities of fluorescent conjugates (1 nmol in this study) and dynamically images in near real-time using a sub-second exposure time. In addition to the sensitive ICCD imaging system, the use of combined holographic and interference filter sets along with a narrow band illumination source, as used herein, reduced the out-of-band signal and the systematic noise level such as excitation light leakage [45]. Unfortunately, the background at 660 nm excitation is mainly due to autofluorescence. Since the optical density (OD) of holographic filters to reject the excitation wavelength for both fluorophores is comparable, and the OD of the bandpass filter to select the emission wavelength is greater for Cy5.5 than IRDye800, there should be less light leakage through the Cy5.5 filters than the IRDye800 filters. Troy *et al.* [122] showed quantitative analysis of autofluorescence signal, which resulted from tissue and instrumental autofluorescence. They showed that an alfalfa-free diet combined with appropriate filter sets could lower the autofluorescence signal in the gastrointestinal regions. In addition, fluorescence imaging with a spectral unmixing algorithm can further reduce the autofluorescence from endogenous chromophores up to far-red region of spectrum [125].

These findings suggest that dynamic planar optical imaging with reduced background can provide the spatial distribution of the fluorescence conjugates and sensitive detection of disease regions. Furthermore, specifically targeted contrast agents may be more effective for diagnosing of solid tumors.

7. IMAGING THE LYMPH NETWORK AND αvβ3 RECEPTOR EXPRESSED IN XENOGRAFTS OF HUMAN KAPOSI'S SARCOMA

In the previous sections we used single wavelength dynamic fluorescence imaging to detect only the tumor compartment. In this section, we imaged two different tissue compartments, tumor vasculature and the draining lymph node, using dual-wavelength fluorescence imaging. The ability to image both tumor blood vessels and lymph vessels will improve our understanding of disease progression.

7.1 Introduction

Lymph node status serves as an important prognostic marker in breast cancer as well as several other cancers. The sentinel lymph node (SLN) is the first lymph node on the lymphatic drainage pathway from the tumor site. The underlying hypothesis of SLN mapping is that the first draining node will contain tumor cells if the cancer is metastatic. When the SLN is resected and found to be negative for metastatic cells, it is assumed that there are no other positive nodes and further lymph node dissection is not necessary. The introduction of a less invasive SLN mapping technique could minimize the number of lymph nodes resected which would preserve lymphatic function.

Traditionally, SLN mapping has been conducted by nuclear imaging with ^{99m}Tc [126-129]. The radiocolloid is often coupled with blue dye for visual surgical guidance after gamma scintigraphy to locate the sentinel node. MRI [130, 131], CT [132], and PET [133-142] have also been used to detect lymphatics. In this Section, we imaged lymph nodes in non-tumor bearing mice after intradermal (i.d.) injection of Cardiogreen.

In addition, we detected tumors after i.v. injection of targeted, cold ^{111}-In-DTPA-K(IRDye800)-c(KRGDf) and lymphatics after i.d. injection of non-specific red light excitable Cy5.5 in mice bearing human Kaposi's sarcoma (KS SLK).

7.2 Materials and Methods

Using a 34-gauge or 26-gauge needle, 9.6 nmol of Cardiogreen in 200 µl of saline was injected into the left rear limb for popliteal node imaging and into the right front limb of four to six week-old female normal nude mice for axillary node imaging. A schematic diagram of the lymph node locations in mice is shown in Figure 7.1. After 20 mins, fluorescence guided lymphadenectomy was performed using near real-time fluorescence images. Histopathology was performed on the excised samples.

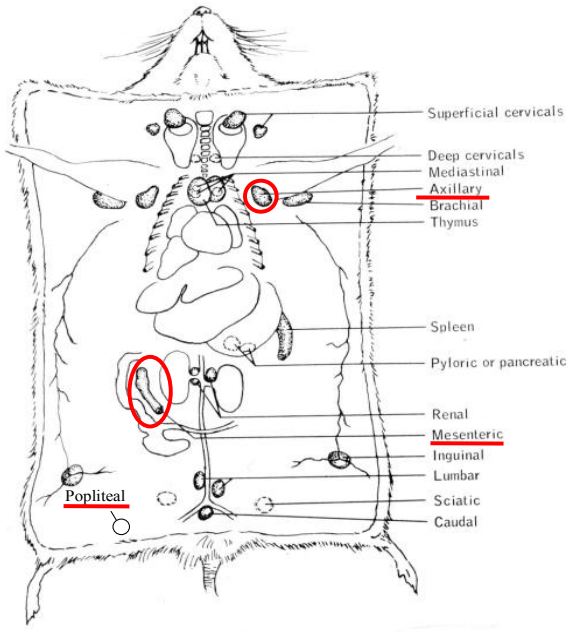

Figure 7.1 Schematic of localization of lymph system [6].

A Kaposi's sarcoma (KS SLK) xenograft tumor was used to image presence of αvβ3 integrin in tumor angiogenesis and lymphangiogenesis. Mice were imaged 24 hrs after the i.v. injection of αvβ3 targeting cold 111-In-DTPA-K(IRDye800)-c(KRGDf), and then 5 nmol of Cy5.5 in 200 μl of saline was injected into the rear left mouse foot using 31-gauge needle for imaging lymph nodes. Again, after 40 to 120 minutes, fluorescence guided lymphadenectomy was performed on tumor bearing mice.

Dual wavelength fluorescence imaging system was used in these studies. A laser diode (80 mW, 785-nm for near-infrared (NIR) dyes and 35 mW, 660-nm for Cy5.5 excitation) provided excitation light, which uniformly illuminated the whole body of the mouse through a convex lens and diffuser. To reject backscattered and reflected excitation light, a holographic notch-plus band rejection filter (780-nm center wavelength for NIR dyes and 660-nm center wavelength for Cy5.5) and a bandpass filter (830-nm center wavelength for NIR dyes and 710-nm center wavelength for Cy5.5) were positioned prior to a 28-mm Nikon lens (Nikon, Japan). The re-emitted fluorescent light was detected by an electron-multiplying charge-coupled device (EMCCD) camera. All the fluorescence images acquired in this study were taken with an 800 msec CCD integration time, by a personal computer running V++ imaging software.

7.3 Results

Figure 7.2 shows that the left popliteal node and the liver were visible 5 mins after the injection using 34-gauge needle, and the secondary node, mesenteric lymph node near G.I. tract was detected at 20 mins after the initial injection. A fluorescence guided

lymphadenectomy was performed by covering liver region to increase the signal intensity of mesenteric lymph node. Both popliteal and mesenteric nodes were successfully removed as presented in Figure 7.2. Successful excision of lymph nodes through image-guided surgery was verified by histology as shown in Figure 7.3.

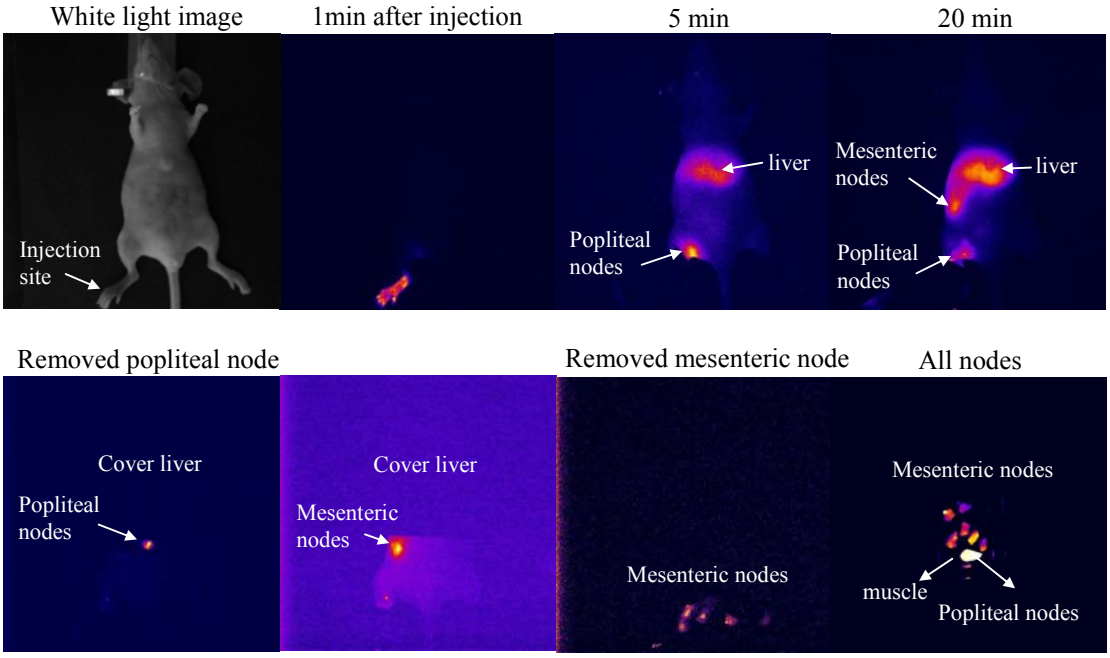

Figure 7.2 Dynamic NIR fluorescence images of a healthy mouse injected into the left mouse foot with 9.6 nmol of Cardiogreen in 200 µl of saline. Popliteal and secondary mesenteric nodes were successfully imaged, and thus removed through image-guided surgery.

Figure 7.3 Histopathology of muscle, and mesenteric and popliteal nodes from real-time NIR image-guided lymphadenectomy.

Figure 7.3 shows the histopathology results from the excised muscle, and mesenteric and popliteal nodes, which confirm the location of lymph nodes and the successful removal achived through image-guided surgery. Figure 7.4 shows fluorescence images after i.d. injection of 5 nmol of cardiogreen in 200 µl of saline into the right mouse paw using 26-gauge needle. After covering the injection site, the axillary lymph node was clearly detected and the liver was fluorescent 10 min after injection. The fluorescence signal in axillary lymph node started decreasing 1 hr after injection, possibly due to drainage of the contrast agent into a deeper location.

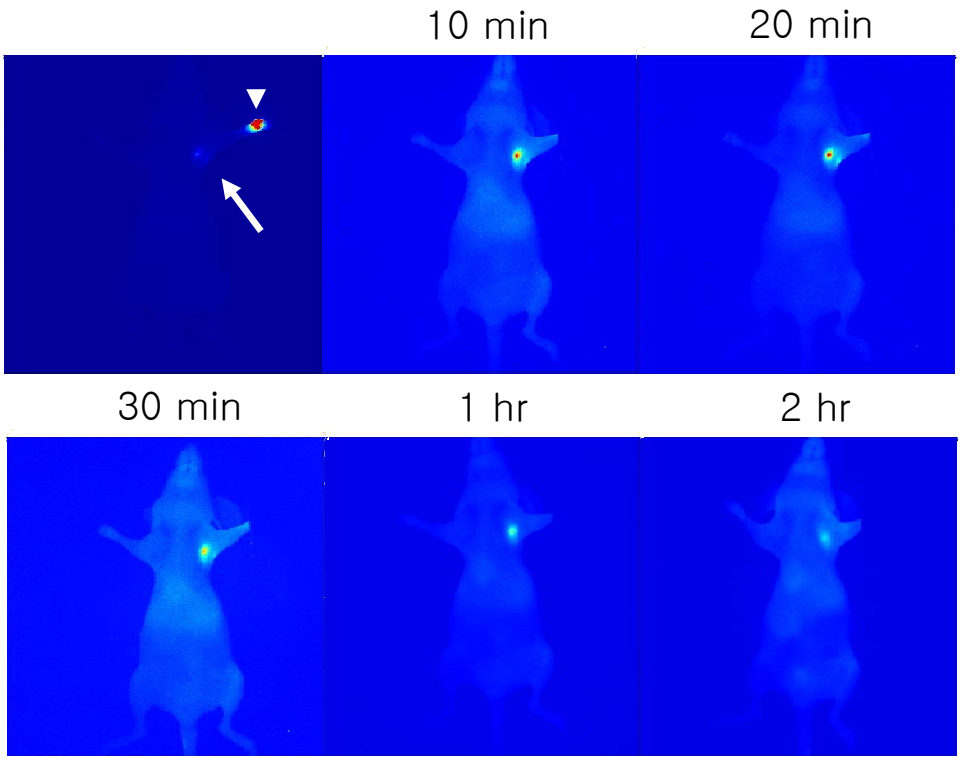

Figure 7.4 NIR Fluorescence images in a healthy animal injected into the right front limb with 5 nmol of Cardiogreen in 200 µl of saline. The axillary lymph node was detected up to 3 hrs after initial injection of Cardiogreen. The arrow head and arrow indicate injection site and the location of lymph node, respectively.

Fluorescence images were also acquired in a KS SLK xenograft model using 660 nm excitation and 710 nm collection optics after injection of 5 nmol of Cy5.5 in 200 µl of saline. As shown in Figure 7.5, the popliteal node was detected 5 min after i.d. injection of Cy5.5 using 31-gauge needle. Due to high autofluorescence signal, however, the secondary mesenteric node, as shown previously in Figure 7.2 could not be differentiated from G.I. tract. From the posterior view, fluorescence signal around the tumor region, which may result from a lymphatic vessel, was detected 10 mins after the injection of Cy5.5 and seen for up to 2 hrs after injection.

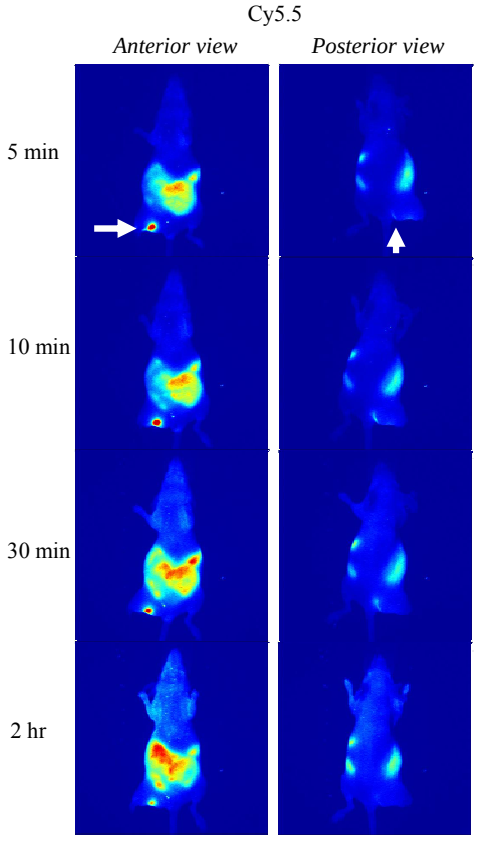

Figure 7.5 Dynamic fluorescence images acquired from a xenograft bearing KS SLK using 660 nm excitation and 710 nm collection optics for Cy5.5 after injection of 5 nmol of Cy5.5 in 200 µl of saline. The arrow indicates the location of lymphatics in tumor region.

Additionally, dual-wavelength fluorescence imaging was conducted in mice with KS SLK tumors and the excised organs using (i) 785 nm excitation illumination and 830 nm collection optics for cold ^{111}In-DTPA-K(IRDye800)-c(KRGDf) and (ii) 660 nm excitation and 710 nm collection optics for Cy5.5. Fluorescent imaging occurred 24 hrs following the initial i.v. injection of cold ^{111}In-DTPA-K(IRDye800)-c(KRGDf). Then, Cy5.5 was injected intradermally into the rear left mouse limb using 31-gauge needle. After 40 minutes, the popliteal node was visible and again removed through image-guided surgery. The removed node is shown in Figure 7.6.

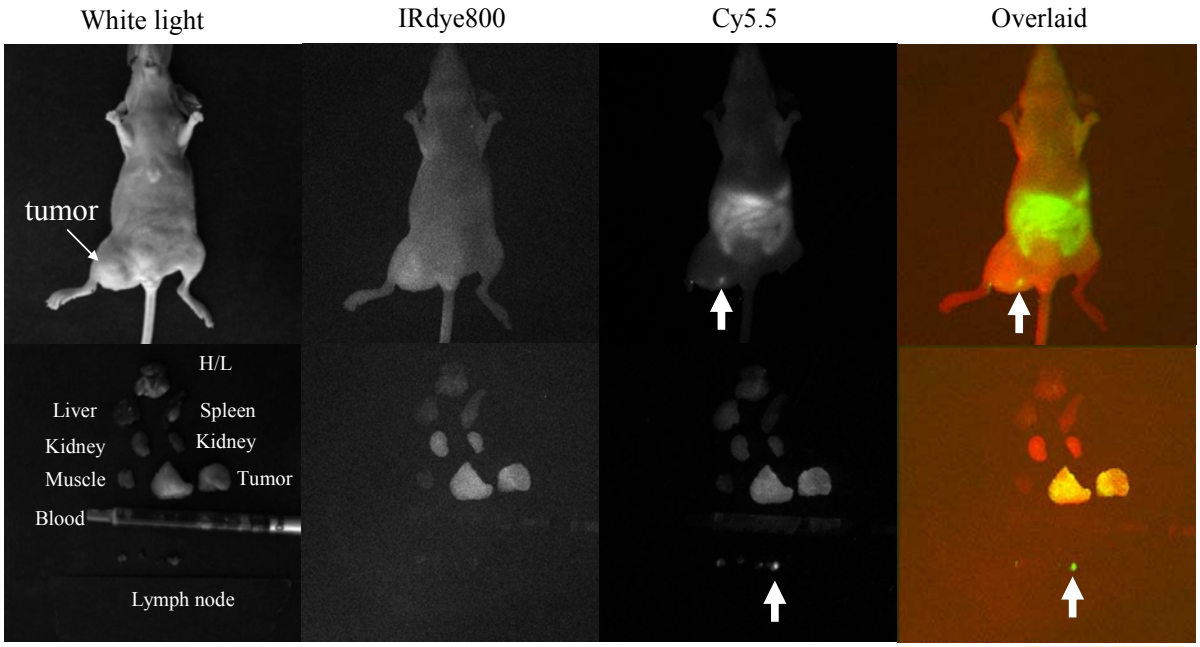

Figure 7.6 Fluorescence imaging of a KS SLK xenograft tumor bearing mouse and the excised organs using (i) 785 nm excitation illumination and 830 nm collection optics for IRDye800 and (ii) 660 nm excitation and 710 nm collection optics for Cy5.5. The arrow indicates popliteal node in the tumor region.

Figure 7.6 shows white light images, single wavelength fluorescence images for NIR and red light, and overlayed images of both NIR and red light images for the whole mouse and the excised organs. High background signal from excitation at 660 nm and emission at 710 nm limited the detection sensitivity. Overlaying single wavelength fluorescence images from the excised organs shows that ^{111}In-DTPA-K(IRDye800)-c(KRGDf), which targets αvβ3, and Cy5.5, which nonspecifically marked the lymph nodes, both accumulated within the tumor region.

7.4 Discussion

In the past, angiogenesis has provided a hallmark for characterizing cancers as well as several other diseases. As discussed in Section 2, αvβ3 integrins play an important role in tumor angiogenesis [18]. Recently, the role of lymphangiogenesis has also been implicated in cancer progression [143]. Lymph vessels control fluid homeostasis, immunity and possibly metastasis. Although extensive research on lymphatics has been performed, our understanding of the fine structure and function of the lymphatic system has progressed slowly [143].

Currently, there are few methods capable of *in vivo* imaging of the lymph system in a small animal. Since lymphatic vessels are relatively small and difficult to locate, there is a need for new delivery devices and imaging modalities with high sensitivity which could be developed into a real-time dynamic imaging system for the lymph system. In this Section, we demonstrated preliminary real-time fluorescence imaging of lymphatics associated with human Kaposi's sarcoma (KS SLK). The 26-, 31-, and 34-

gauge needles delivered agents into the dermal space for uptake into the lymphatic system in the mouse. Lymph nodes were detectable ~ 5 min after injection of fluorescent contrast agents. Additionally, as shown in Figure 7.2, secondary lymph node was detected 20 min after the injection. Fluorescence image-guided lymphadenectomy was successfully performed as shown in Figure 7.2 and 7.6. As an intraoperative imaging system described by Kim *et al*. [144], dynamic fluorescence imaging using an appropriate imaging system may be able to track lymph flow in real time and to guide resection of lymph nodes in cancer patients.

As previously discussed in Section 6, NIR excitable dyes, such as IRDye800 and Cardiogreen which were used in this study, resulted in reduced background signal and enhanced the detection ability, especially when compared with Cy5.5 imaging in the mouse abdomen. Fluorescence images in mice injected with Cy5.5 showed high autofluorescence near G.I. tract resulting from mouse diet, resulting in the limited detection of secondary lymph nodes as shown in Figure 7.6 and 7.7.

The popliteal nodes were detected in human Kaposi's sarcoma xenograft bearing mice following i.d. delivery of Cy5.5 to the rear left limb. In addition, in the posterior view of the mouse, the lymphatics were fluorescent up to 2 hrs after injection of Cy5.5 as shown in Figure 7.5 possibly due to lymphangiogenesis. Only lymph nodes but no lymphatic vessels were detected in a non-tumor bearing mouse during fluorescence imaging. Overlaid fluorescence images from excised organs showed that cold 111-In-DTPA-K(IRDye800)-c(KRGDf) and Cy5.5 were colocalized into tumors.

Although the imaging in Figure 7.6 required changing out the appropriate filter sets for fluorescence imaging with each specific wavelength, our results showed that dynamic multi-wavelength fluorescence imaging is promising and thus is explored further in the following section as a method for near simultaneous imaging of different agents targeting different markers in the xenografts.

8. DYNAMIC MULTI-WAVELENGTH WHOLE-BODY FLUORESCENCE IMAGING WITH LIQUID CRYSTAL TUNABLE FILTER

In Section 5, we demonstrated dynamic real-time fluorescence imaging, which enabled the tracking of NIR contrast agents through the whole body of mouse as well as the delineation of normal and diseased tissues. Additionally, in Section 7, we showed multi-wavelength fluorescence imaging of tumor and intact lymph nodes. The experimental studies described in this section describe developments for dynamic multi-wavelength fluorescence imaging after simultaneous injection of multiple contrast agents. Most importantly, the developments represent a step towards using our technology for image-guided surgery. The synthesis of contrast agents described in this section was performed by Dr. Wei Wang. Therefore, the experimental aspects related to contrast agents are discussed briefly for completeness.

8.1 Introduction

Multi-spectral fluorescence imaging techniques can improve diagnoses due to fluorescence spectra and emission intensity of the different chromophores [145-147]. A liquid crystal tunable filter (LCTF) has been used for acquiring spectral imaging, by allowing only light in a narrow wavelength range to reach the camera. In addition, the LCTF can allow rapidly switching of the peak position of the bandpass within milliseconds with about 1-nm precision [148, 149]. A series of fluorescence images can thus be rapidly acquired at different wavelengths to create spectral or dynamic multi-wavelength imaging data. Spectral imaging data can be further used to identify, separate

and remove the contribution of autofluorescence in analyzed images [150]. Multi-wavelength fluorescence imaging may also have the potential to (i) image and colocalize multiple targets, (ii) assess differential expression levels of multiple targets, and (iii) image response to targeted therapies.

Although near infrared (NIR) fluorescence imaging technology has gained a considerable amount of interest for possible applications in medicine due to low tissue absorption in NIR range, NIR fluorescence continuous-wave (CW) imaging is conducted in a dark room to maximize its sensitivity. To use NIR fluorescence optical imaging systems during human surgery, "white light" or visible light should be provided simultaneously with NIR light or "invisible" light so that the surgeon can identify tissues within the surgical field. Recently, Grand *et al.* [151] reported intraoperative NIR fluorescence imaging system. They used two laser sources, one providing NIR excitation light and the other "white" light via appropriate filters. In addition, a separate camera system was used to detect each light. Two lights, visible light and fluorescence light, were optically separated by a dichroic mirror and barrier filters, and detected by each camera. They successfully demonstrated their imaging system in large animal surgery. However, their intraoperative imaging was not dynamic and was limited to one specific fluorescence wavelength. For each additional wavelength to be imaged another light laser source and camera with the appropriate filter set must be added.

Herein, we demonstrate dynamic real-time whole-body multi-wavelength imaging using a liquid crystal tunable filter (LCTF). Since several different emission wavelengths can be selected after tuning LCTF, we showed dynamic fluorescence imaging in two

wavelengths in mice bearing M21 and M21L xenografts after injection of mixture of ^{111}In-DTPA-K(IRDye800)-c(KRGDf), targeting αvβ3, and non-specific agents, Cy5.5. In addition, since excitation light reflection can be used for "white" light images when LCTF transmits shorter wavelengths than the peak in the excitation light spectrum, fluorescence images and white light images can be dynamically acquired, enabling image-guided surgery. Finally, we compared the LCTF performance with a set of a holographic notch-plus band rejection filter with a narrow-band interference filter in order to assess excitation light leakage, which limits sensitivity in fluorescence imaging.

8.2 Materials and Methods

8.2.1 Fluorescence Imaging System

For fluorescence-enhanced imaging, appropriate wavelengths were selected to elicit fluorescence from embedded fluorophores. In these studies, the excitation light was provided by laser diodes (785-nm, 85-mW for IRDye800; 660-nm, 35-mW for Cy5.5, Thorlabs, Inc, NJ) at the selected wavelengths. The excitation light uniformly illuminated the whole surface area (10 X 10 cm) through convex lenses and diffusers. Each laser has a diode driver and temperature controller (ThorLabs, Inc., models LDC500 and TEC2000, respectively, Newton, NJ) to maintain a constant wavelength.

For multi-spectral and multi-wavelength imaging, a LCTF (Model: SNIR, VariSpec, CRI Inc, Woburn, MA) was used. The LCTF was placed in front of a 28 mm lens with a camera adapter thread ring. Placing the LCTF in front of the lens provides the accurate focus adjustment for calibration of the lens as shown in Figure 8.1. The imaging

system was designed so that the field of view could be varied from 5 X 5 cm to over 10 X 10 cm by varying the focal length of the 28-mm lens used to focus the image onto the EMCCD camera. Figure 8.1 shows a schematic of a multi-wavelength and multi-fluorescence imaging system. All serial commands sent through the USB interface to control the LCTF were ASCII text, which were scripted in V++ image acquisition software. Therefore, the LCTF was controlled using the image acquisition software, programmed with scripts to synchronize the frame transfer from the EMCCD camera, resulting in dynamic multi-wavelength imaging due to rapid tuning of wavelengths with the LCTF.

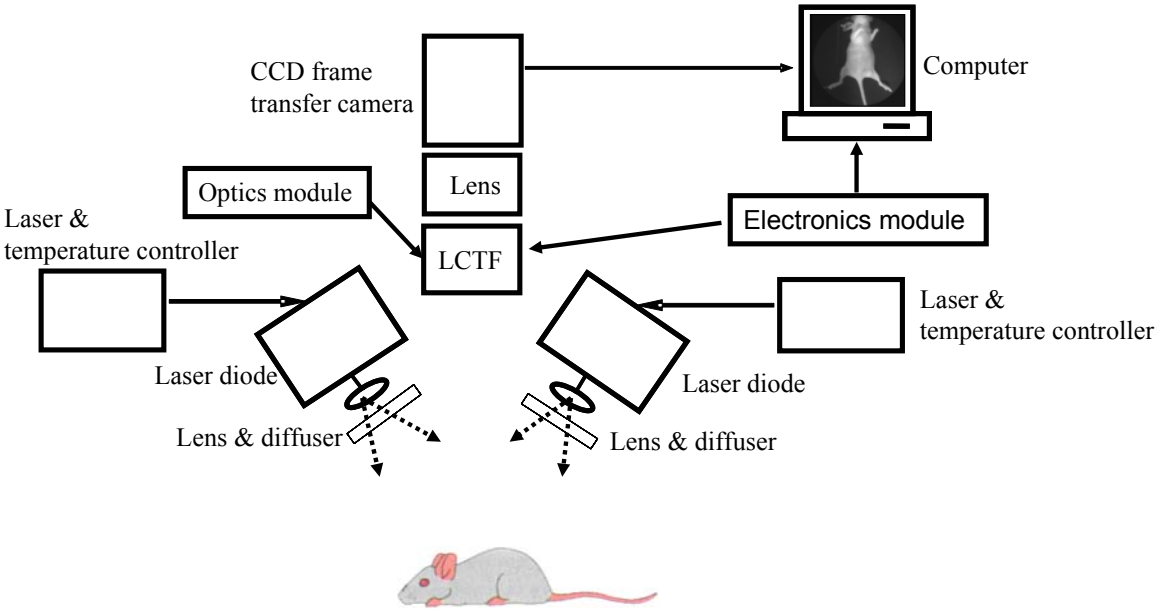

Figure 8.1 Schematic of multi-wavelength whole-body fluorescence imaging system with the LCTF.

For transmission of fluorescent light, LCTF was tuned for the specific emission wavelengths, i.e. 830-nm for IRDy800 and 710-nm for Cy5.5. For white light images, a shorter wavelength in the excitation light spectrum of Cy5.5, i.e. 650-nm was transmitted.

For comparison of filter performance, the set of the holographic notch-plus band rejection filter (660-nm center wavelength for Cy5.5, OD at λ_x reported to be >6, 785-nm center wavelength for IRDye800; Kaiser Optical Systems, OD at λ_x reported to be >6, Inc., Ann Arbor, MI) and narrow-band interference filter (830-nm center wavelength for IRDy800, OD at λ_x reported to be 4, 710-nm center wavelength for Cy5.5 OD at λ_x reported to be >3; CVI Laser Corporation, Albuquerque, NM) were fitted with a 28 mm lens to reject back-scattered and reflected excitation light while collecting fluorescence emission light. Fluorescence emission light was detected by electron multiplication charge-coupled device (EMCCD) camera. All fluorescence images acquired in this study were taken at 800 msec of EMCCD integration time.

8.2.2 *In vitro* Experiments

For multi-spectral and multi-wavelength imaging, 1 nmol of IRDye800 in 0.2 ml of saline, 1nmol of Cy5.5 in 0.2 ml of saline, and 0.2 ml of saline were imaged with the LCTF. At first, wavelength-resolved spectral imaging with LCTF and LCTF with holographic notch filters of Cy5.5 and IRDye800 were carried out with both lasers turned on. The tunable filter was stepped from 650 to 1000 nm in 10 nm increments. Multi-wavelength fluorescence imaging was dynamically performed for 40 min after setting wavelengths at 650 nm for “white” light imaging, and 710 and 830 nm for fluorescence

imaging of Cy5.5 and IRDye800, respectively. The mean of the fluorescence intensities for each dye in each fluorescence image using the different filters was then calculated.

For an analysis of background rejection by each filter, fluorescence imaging was performed after filters were coupled by the following combinations: (1) LCTF; (2) LCTF with the holographic notch filter; (3) a single bandpass filter; and (4) a bandpass filter with the holographic notch filter. LCTF was set at 710 nm for Cy5.5 and 830 nm for IRDye800. CW measurements were taken with the different optical filters with and without IRDye800 and Cy5.5 added at 25 μM of IRDye800 and Cy5.5 in a 2 % liposyn suspension. The images of the uniform media in the presence and absence of each fluorophore provide a method to assess excitation leakage. The transmission ratio for each collection optic is defined as:

$$R = \frac{S(\lambda_x)}{S(\lambda_m) - S(\lambda_x)} \tag{6.1}$$

where $S(\lambda_x)$ is the mean fluorescence intensity values associated with the measurements taken in the absence of IRDye800 and Cy5.5 in the solution and $S(\lambda_m)$ is averaged from the pixel intensity values associated with the measurements taken in the presence of IRDye800 or Cy5.5 in the solution. The $S(\lambda_x)$ signal represents "out of band" transmission signal, whereas the difference, $S(\lambda_m)$ - $S(\lambda_x)$, when taken at the same experimental condition, represents the "in-band" transmission signal.

8.2.3 *In vivo* Experiments

For *in vivo* imaging studies, six to eight week-old female SCID mice (18-22g) were purchased from Charles River, Inc, Wilmington, MA. Animals were housed in a pathogen-free mouse colony in the Frensley Center for Imaging Research (Baylor College of Medicine). The animal protocol was approved by the American Association for Laboratory Animal Care and all experiments were conducted in accordance with guidelines of the Institutional Animal Care and Use Committee.

Human melanoma M21 (integrin αvβ3 positive) and M21L (integrin αvβ3 negative) cells (2-3 × 10^6 / animal) were implanted subcutaneously into the left thigh region of mice. Tumors were allowed to grow approximately ~ 6 mm in size. Before administration of imaging agent, animals were placed on a temperature-controlled heating pad (Spin System, Australia) at 37 C under isofluorane anesthesia (VetEquip, Pleasanton, CA and IsoSol Isofluorane USP, VEDCO Inc., St. Joseph, MO). A tail vein catheter was inserted into each animal. Dual-labeled RGD peptides for optical and nuclear imaging, ^{111}In-DTPA-K(IRDye800)-c(KRGDf) [55, 152] (5 nmol in 200 μl of saline) [55] and Cy5.5 (5 nmol in 200 μl of saline) were injected into the tail vein of an anesthetized mouse with a constant injection rate (30 ml/min) controlled by a syringe pump (Model: PHD 2000, Harvard Apparatus in Holliston, MA). Multi-wavelength dynamic fluorescence images with the LCTF were obtained immediately following the injection of the imaging agents for approximately 40 min and at 24 and 48 hrs following injection of contrast agents. Fluorescence images from Cy5.5 and IRDye800 were also acquired with a bandpass filter and a holographic notch filter described previously at 24

and 48 hrs after the injection of the two contrast agents. In addition, scintigrams were acquired. Tumor and normal regions of interest (ROIs) were defined from "white" light images after collecting 650 nm reflected light. The mean of the fluorescence intensity within each ROI for each fluorescence image was then calculated. TBR was calculated by dividing the mean intensity in the tumor ROI by that in the contralateral normal ROI.

8.2.4 Software and Data Analysis

All images were acquired by a personal computer using V++ imaging software (Digital Optics, Auckland, New Zealand). The LCTF offers USB interface, which provides complete control of LCTF using a series of ASCII commands. V++ can control LCTF with ASCII commands, resulting in synchronization with the EMCCD camera. For tuning wavelengths with the LCTF, a 150 ms transition time at room temperature was added to the image acquisition program. Data analysis was accomplished with Matlab software (The MathWorks, Inc., Natick, MA), SigmaPlot software package (SPSS Inc., Chicago, IL), and ImageJ (National Institutes of Health, Washington, DC) after completion of the image acquisition. The transmission ratios were compared with the student t-test SPSS 12.0.1 statistical program (SPSS, Inc., Chicago, Illinois). If $p < 0.05$, the results are considered statistically significant.

8.3 Results

8.3.1 Multi-wavelength and Spectral Imaging

Dynamic dual fluorescence imaging of vials filled with IRDye800, Cy5.5, and normal saline as a control was conducted for 40 min to test the stability and synchronization of the LCTF and the camera during dynamic imaging. Figure 8.2 shows the normalized fluorescence intensity vs. time profiles within each ROI. Dynamic fluorescence intensities from IRDye800 and Cy5.5 were constant during dynamic imaging with three different wavelengths in sequence, one "white" light and two fluorescence images as shown in Figure 8.3.

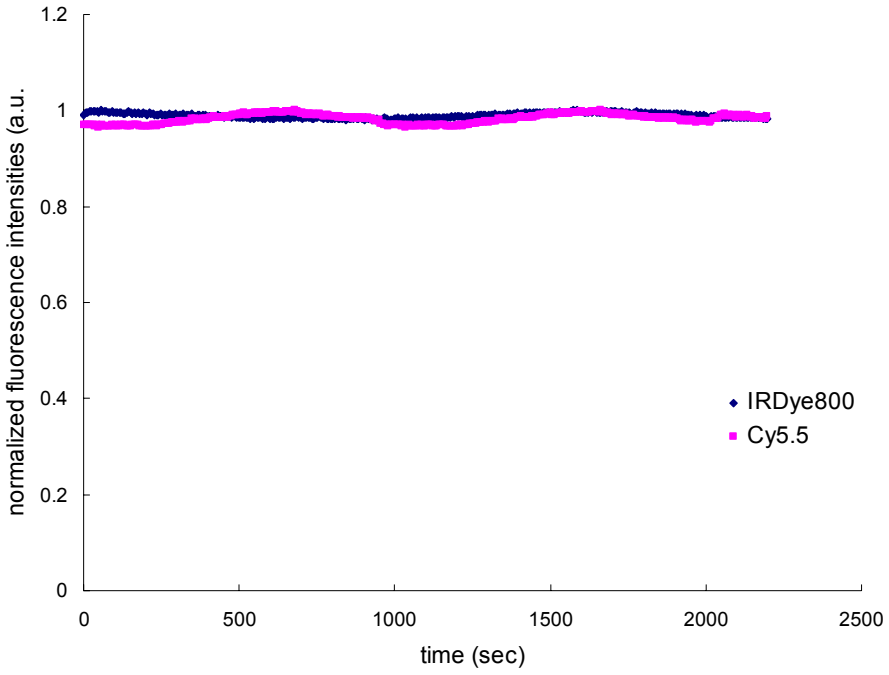

Figure 8.2 Fluorescence intensity vs. time profiles from ROIs in vials filled with IRDye800 and Cy5.5 for 40 min.

Figure 8.3 shows a "white" light image and fluorescence images of Cy5.5 and IRDye800, all of which were acquired with the LCTF at the respective emission wavelengths. Figure 8.4 shows fluorescence intensity vs. wavelength profiles for the spectral imaging. When the LCTF was used, two peaks were detected from the two excitation lights, 660 nm for Cy5.5 and 785 nm for IRDye800. In addition, two emission peaks were detected at 700 nm for Cy5.5 and 800 nm for IRDye800. When both holographic notch filters for Cy5.5 and IRDye800 were coupled with the LCTF, the two excitation light peaks were removed, and the emission peak of IRDye800 was shifted to 810 nm. Fluorescence emission intensities from Cy5.5 were reduced by 23 % at 700 nm, while signals from IRDye800 were reduced by 87 % at 800 nm and 34 % at 810 nm.

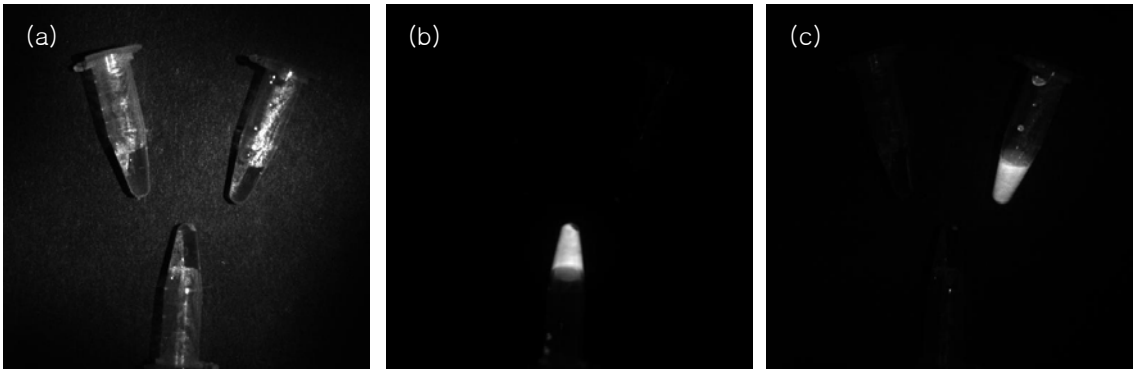

Figure 8.3 Images collected from the LCTF. "White" light image after transmitting the wavelength at 650 nm (a) and fluorescence images from vials filled with IRDye800 (b) and Cy5.5 (c) after transmitting wavelengths at 710 nm and 830 nm, respectively.

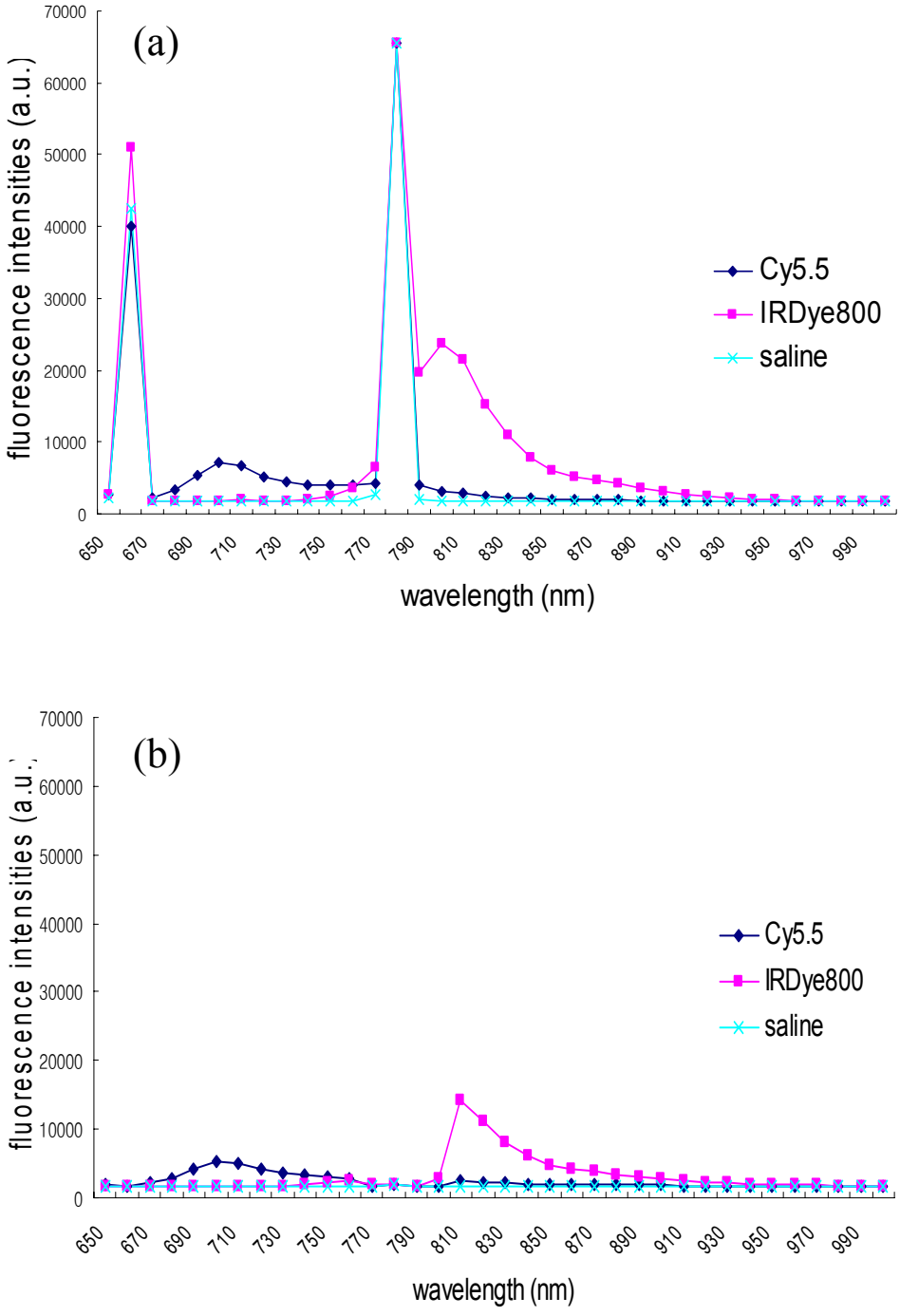

Figure 8.4 Fluorescence intensities from spectral imaging of 1 nmol of IRDye800 and Cy5.5 in 200 µl of saline and 200 µl of saline with (a) LCTF, and (b) LCTF with a holographic filter.

8.3.2 Background Rejection

As shown in Figure 8.4 (a), the emission peaks from IRDye800 and Cy5.5 are 800 nm and 700 nm, respectively. For comparison of filter performance for background rejection, however, LCTF transmitted fluorescence at 710 nm for Cy5.5 and at 830 nm for IRDye800. Table 8.1 shows, in-band, out-of-band, and transmission ratios acquired in the absence and presence of IRDye800 or Cy5.5 with optical filter combinations of (1) bandpass; (2) bandpass and holographic filters; (3) LCTF; and (4) LCTF and holographic filter. The transmission ratios with a single bandpass filter were the highest in 25 μM IRDye800 ($p<0.05$) and 25 μM Cy5.5 liposyn suspension ($p<0.05$) as expected. The transmission ratios with a bandpass filter and a holographic filter, LCTF, and LCTF with a holographic filter were similar. However, in-band transmission with a bandpass filter and a holographic filter, which are currently used in small animal imaging in our lab, was reduced by more than two orders of magnitude over the LCTF and the LCTF with a holographic filter (Table 8.1).

Table 8.1 Average intensity (in-band and out-of-band) and corresponding transmission ratios from 25 µM of IRDye800 and 25 µM of Cy5.5 in a 2 % liposyn suspension. Errors are represented as standard deviation values.

	Cy5.5		
	In-band	Off-band	Transmission ratio
A bandpass filter	38130 ± 47	7641 ± 27	0.20 ± 0.001
A bandpass filter with a holographic filter	35132 ± 72	6162 ± 10	0.17 ± 0.0003
LCTF	16533 ± 51	2869 ± 39	0.17 ± 0.002
LCTF with holographic filter	14421 ± 14	2290 ± 5	0.15 ± 0.0003

	IRDye800		
	In-band	Off-band	Transmission ratio
A bandpass filter	44935 ± 48	16201 ± 40	0.36 ± 0.001
A bandpass filter with a holographic filter	49498 ± 11	6624 ± 2	0.13 ± 0
LCTF	19058 ± 17	2256 ± 7	0.11 ± 0.0003
LCTF with holographic filter	14575 ± 43	1812 ± 2	0.12 ± 0.0002

8.3.3 *In vivo* Imaging

Figure 8.5 shows the normalized fluorescence intensity vs. time profiles in the tumor and contralateral normal tissue ROIs in mice bearing M21 (a) and M21L (b) immediately following the injection of ^{111}In-DTPA-K(IRDye800)-c(KRGDf) and Cy5.5.

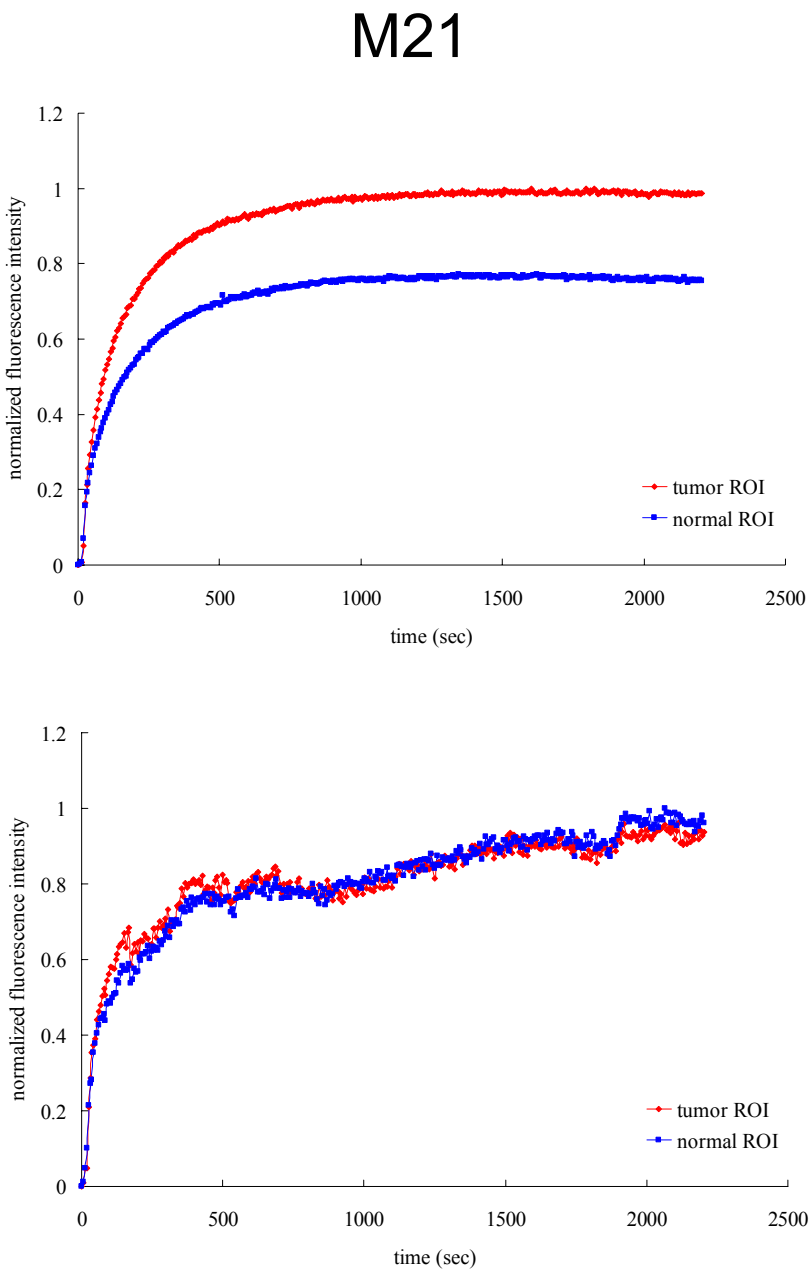

Figure 8.5 Normalized fluorescence intensity vs. time profiles from xenografts of M21 (a) and M21L (b) that received an injection of the IRDye800 conjugated RGD and Cy5.5 at each 5 nmol in 200 μl of normal saline, acquired from the tumor (red) and normal tissue (blue) ROIs. Emission wavelengths for Cy5.5 and IRDye800 were set as 710 nm and 830 nm, respectively.

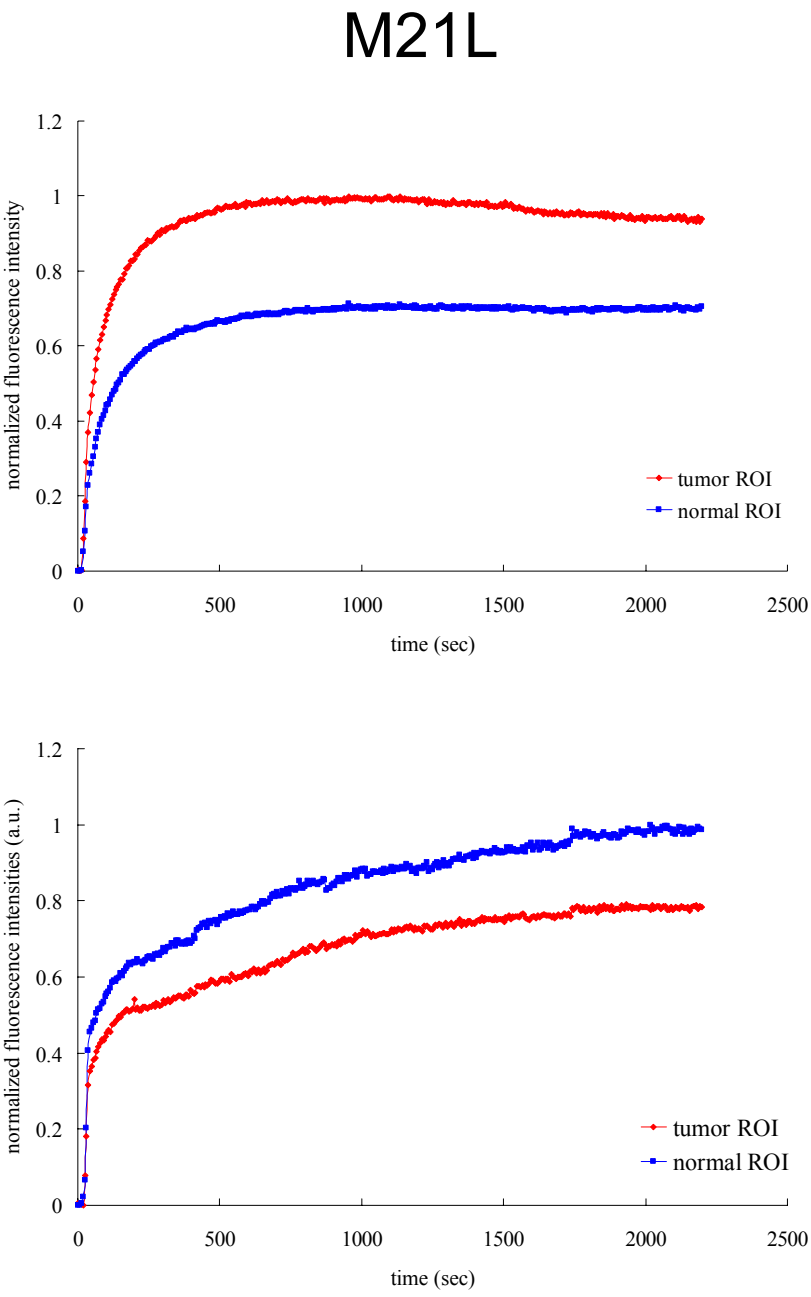

Figure 8.5 continued

Emission wavelengths for Cy5.5 and IRDye800 were set at 710 nm and 830 nm, respectively. Fluorescence intensities were acquired during dynamic multi-wavelength imaging, which took a series of fluorescence images of red light excitable and NIR fluorescent dyes. Fluorescence intensities in tumor ROIs showed higher accumulation than those in normal ROIs in M21 xenografts after injection of integrin αvβ3 targeting IRDye800 conjugated RGD (Figure 8.5). The amount of targeted agent in the tumor ROIs for the M21 xenografts increased over time. Non-specific, Cy5.5 showed similar accumulation in both normal and tumor ROIs. Fluorescence intensities in the tumor ROIs of M21L xenografts rapidly increased, then slowly decreased over 40 min following the injection of IRDye800 conjugated RGD, while intensities in normal ROIs in the M21L model were similar to those in the M21 model. In addition, fluorescence intensities in the normal ROIs in M21L xenograft bearing mice injected with Cy5.5 were higher or similar to those in the tumor ROIs.

Figures 8.6 and 8.7 show normalized fluorescence images using the bandpass and holographic filter sets, and LCTF in mice bearing a subcutaneous M21 (Figure 8.6) and M21L (Figure 8.7) human melanoma tumor on the left posterior limb 24 hours after the injection of 5 nmol of free Cy5.5 in 200 μl of saline and 5 nmol of ^{111}In-DTPA-K(IRDye800)-c(KRGDf) in 200 μl of saline. The M21 tumors were clearly detected in both normalized NIR fluorescence images with the bandpass and holographic filter set and LCTF. In addition, M21 tumors were shown in SPECT/CT images (Figure 8.6 (e)).

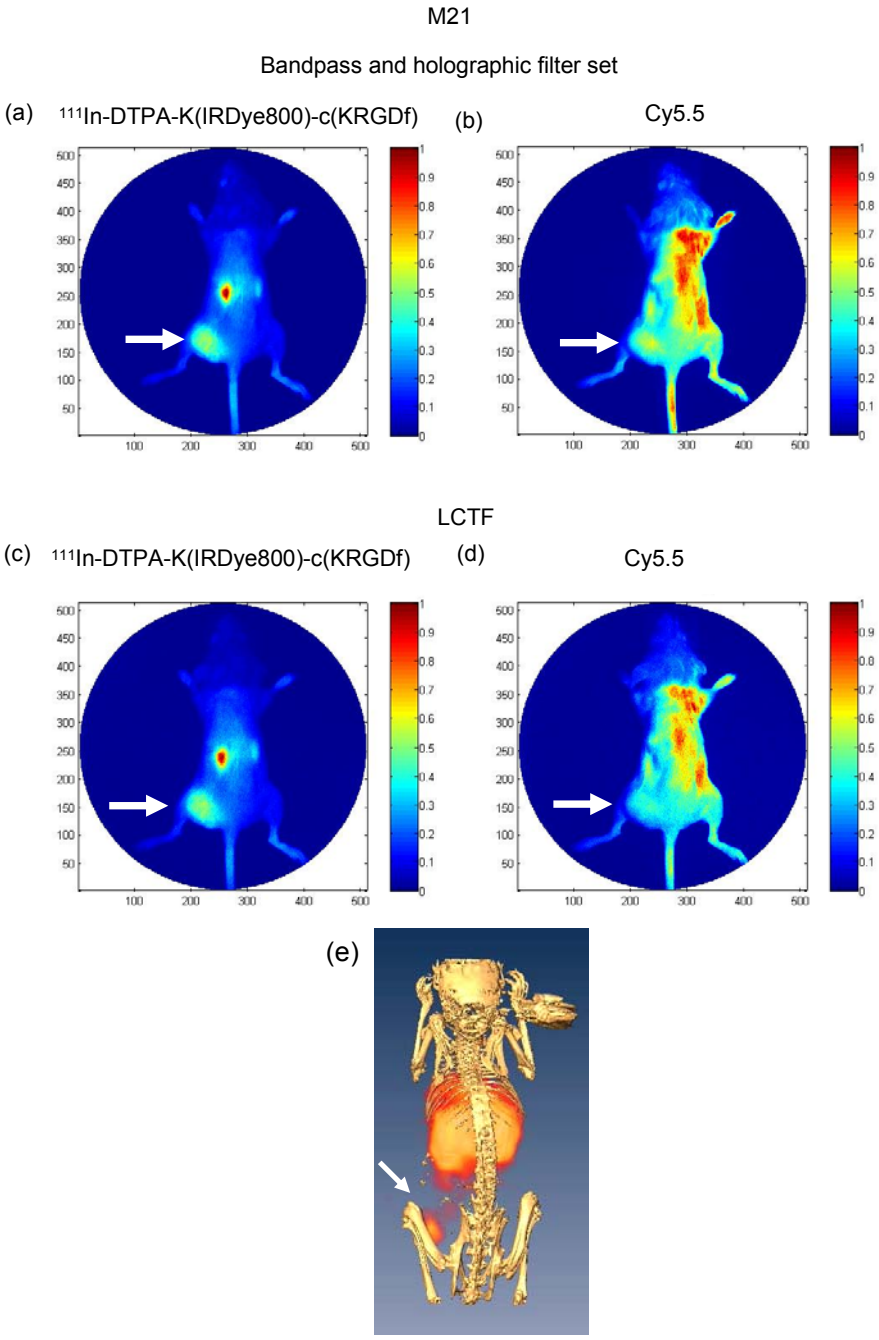

Figure 8.6 Normalized fluorescence images ((a), (b), (c), and (d)) and SPECT/CT image (e). Fluorescence images were acquired with a bandpass and holographic filter set ((a) and (b), and LCTF ((c) and (d)) in mice bearing M21 24 hr after injection of ^{111}In-DTPA-K(IRDye800)-c(KRGDf) ((a) and (c)) and Cy5.5 ((b) and (d)). The arrow indicates the tumor location.

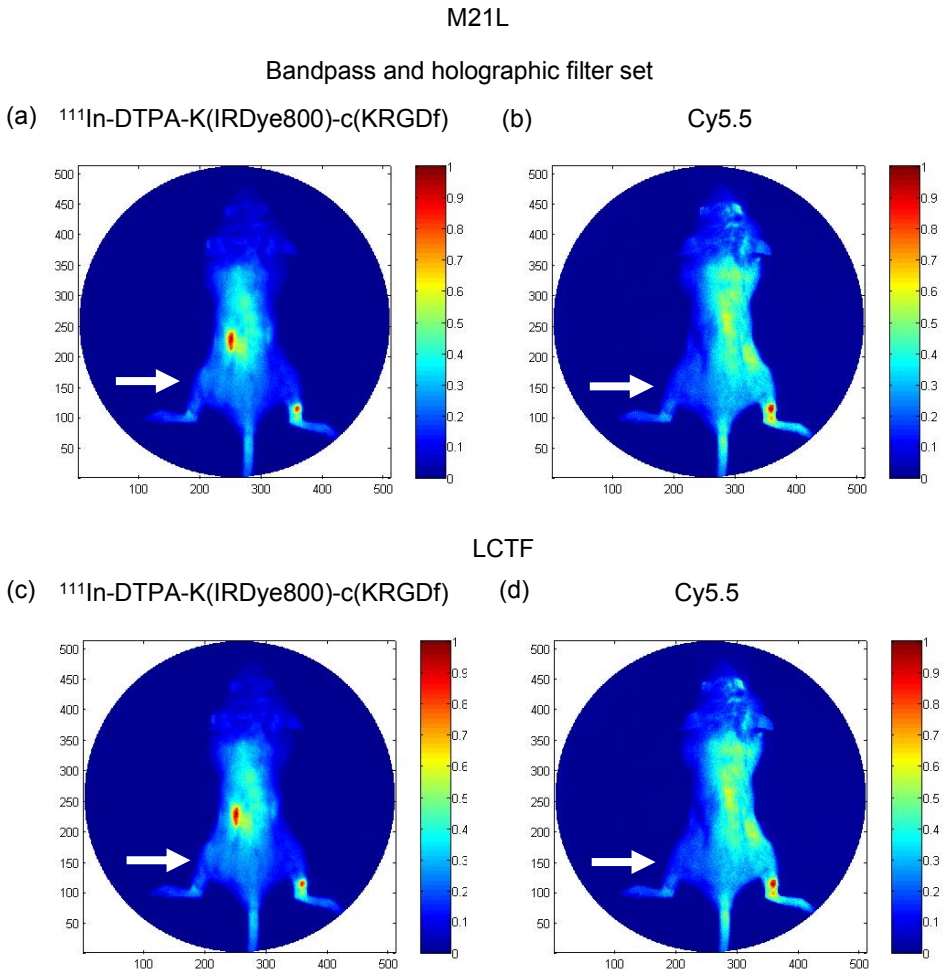

Figure 8.7 Normalized fluorescence images from a bandpass filter and holographic filter set ((a) and (b), and LCTF ((c) and (d)) in mice bearing M21L 24 hr after injection of ^{111}In-DTPA-K(IRDye800)-c(KRGDf) ((a) and (c)) and Cy5.5 ((b) and (d)). The arrow indicates the tumor location.

Fluorescence images with Cy5.5 show no tumor detection, greater excitation light leakage, and higher autofluorescence compared to those with IRDye800 as discussed in Section 5. The M21L tumor was not delineated in NIR or red light excitable fluorescence images, because it has no αvβ3 integrin. Autofluorescence and as excitation light leakage were detected in the red light excitable fluorescence images.

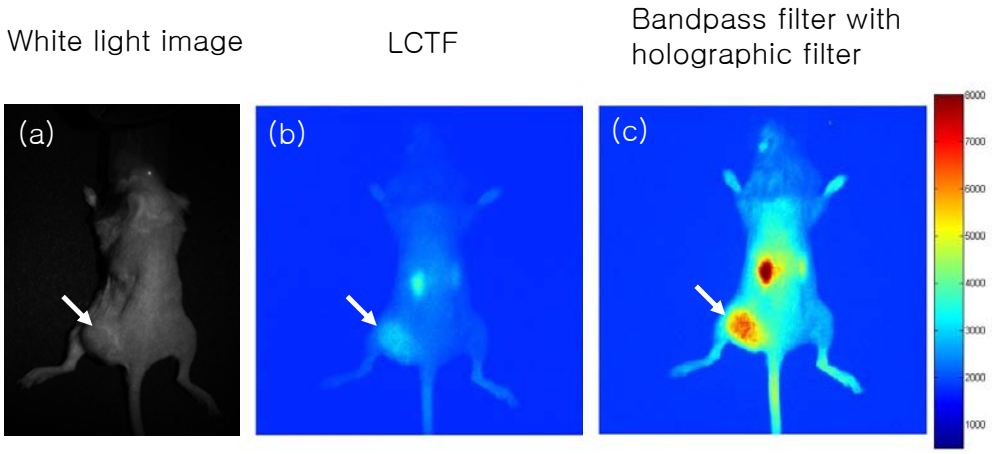

Figure 8.8 "White" light (a), NIR using the LCTF (b) and NIR using the bandpass filter and holographic filters (c) in mice of M21 24 hr after injection of ^{111}In-DTPA-K(IRDye800)-c(KRGDf). The arrow indicates the tumor location.

Figure 8.8 shows the "white" light image from the LCTF and NIR fluorescence images from the LCTF, and a bandpass filter and holographic filter set in M21 xenografts 24 hr after the injection of ^{111}In-DTPA-K(IRDye800)-c(KRGDf). As shown in Table 6.1, fluorescence intensities in tumor ROIs were more than two times lower with LCTF than those with a bandpass filter and holographic filter. Figure 8.9 shows TBR values in M21 xenografts 24 hr after injection of ^{111}In-DTPA-K(IRDye800)-c(KRGDf) and Cy5.5. TBRs from NIR fluorescence images with a bandpass and holographic filter were not statistically different from those with LCTF. TBRs from red light excitable fluorescence images were also similar in each filter configuration.

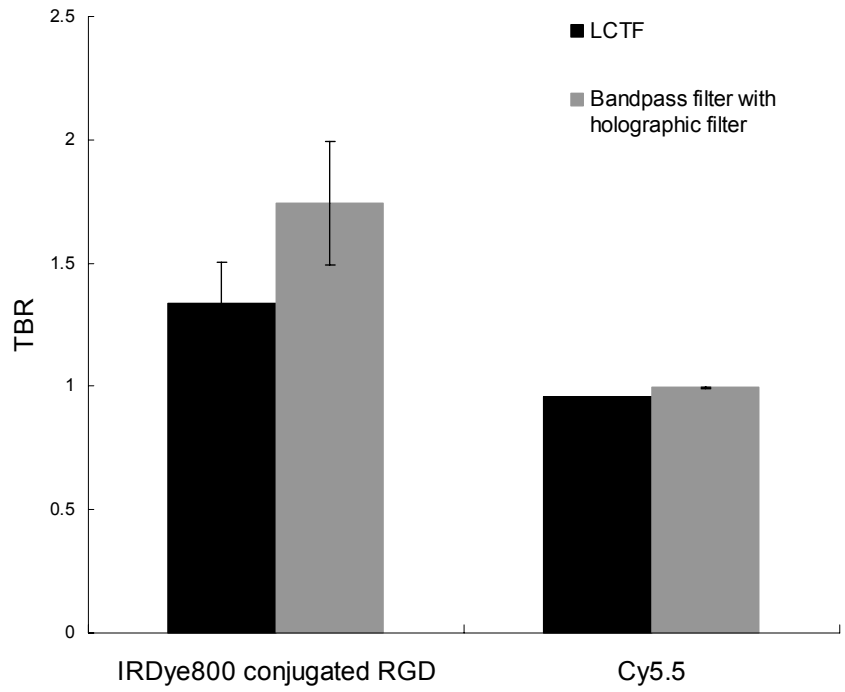

Figure 8.9 Tumor to background ratio (TBR). The black and gray columns denote the mean value of each test group 24 hour after the injection of the IRDye800 conjugated RGD and Cy5.5 with LCTF and a bandpass filter and holographic filter, respectively, and the error bars represent the standard deviation.

8.4 Discussion

In this section, we demonstrated dynamic multi-wavelength whole-body fluorescence imaging using the LCTF. As shown Figure 8.1, the LCTF was mounted to the front of a lens attached directly to a camera. In this configuration, the lens can be focused normally. A filter with a 10 mm aperture was used and successfully prevented vignetting of the fluorescence images. A compact electronics controller box is connected to the filter's optics housing, to accept serial commands from the host computer.

Therefore, a simple program can be used to control the LCTF for synchronization with a camera though an available USB port on a PC-compatible computer. Since (i) the LCTF can be set to allow the light from a narrow set of wavelengths to reach the camera and (ii) the peak position of this bandpass can be rapidly switched to any other position within 150 milliseconds, a series of dynamic multi-wavelength images could be rapidly acquired at different wavelengths. Additionally, since no filter wheel is needed, images are registered perfectly. During dynamic multi-wavelength fluorescence imaging for 40 min, tuning wavelengths with the LCTF was synchronized with the camera (Figure 8.2).

Dynamic multi-wavelength imaging can be used to correct for blood perfusion when the accumulation of targeting agent in different xenograft tumor models is compared as shown previously in dual energy window in SPECT [96] which was discussed in Section 2. Furthermore, it can be used to image several different locations with different targeted fluorescence conjugates, such as the tumor neovasculature or the tumor cells themselves or the tumor lymphatics. In addition to multi-wavelength fluorescence imaging, when shorter wavelengths than that excitation peak are transmitted by the LCTF it is possible to collect visible light images. The sensitivity to wavelengths between 400 and 700 nm is more than two logs lower than that of those above 700 nm [151], allowing for the capture of visible light which can be used for “white” light images to guide a surgeon within the surgical area during fluorescence imaging. Figures 8.3 and 8.8 show “white” light images collected by transmitting 650 nm light, and fluorescence images, IRDye800 collected by transmitting 830 nm light and Cy5.5 with 710 nm light. Both multi-wavelength imaging and spectral imaging have been also used in medicine.

In a melanoma tumor, for example, spectral imaging can overcome the problem of pigment interference in the human melanocytic progression pathway [146].

However, the nonuniformity of the excitation light may cause the nonuniform fluorescence generation seen from area illumination in the phantom and from the small-animal studies as shown in Cy5.5 fluorescence images (Figures 8.6 and 8.7). Houston *et al.* [45] showed that the different filter combinations alter (i) the transmission of specularly reflected and diffusely propagated excitation light, (ii) the transmission of generated emission light, and (iii) the spatial distribution of intensities. Since the LCTF uses polarization in the spectral selection process, transmission efficiencies are typically in the 30%-range while traditional interference filters transmit approximately 90% of the incoming light. As shown in Table 6.1, fluorescence signals from LCTF are reduced by 59% for Cy5.5 and 70% by IRDye800 as compared to each set of a bandpass and holographic filter set. Therefore, the contribution of excitation light leakage to lower transmission efficiencies should be studied. Since the expanded laser beam intensity was nonuniform and covered an area smaller than that of the imaged surface, a region of uniform excitation light delivery in the center of the images was selected, covering an area ~5 cm-diameter. The image of the surface of the tissue phantom in the presence and absence of IRDye800 and Cy5.5 was used to assess excitation light leakage. Table 6.1 shows that transmission ratios from a bandpass filter with a holographic filter were similar to those from LCTF and LCTF with a holographic filter, indicating similar capacity to reject excitation light leakage. Lower transmission efficiencies can be improved by increasing camera gain, integration time, and laser power. Nonetheless,

NIR fluorescence images after using LCTF in mice bearing M21 tumors showed clear visualization of the tumors. In addition, TBR from a bandpass filter with a holographic filter was not significantly different from that with the LCTF ($p>0.05$). Therefore, the benefit of spectral information as well as dynamic multi-wavelength may outweigh the impact of the lower transmission efficiencies, and could enable *in vivo* small animal imaging and ultimately clinical imaging.

9. SUMMARY AND CONCLUSIONS

A novel fluorescence imaging modality has been developed for non-invasive dynamic small animal imaging, and ultimately for human clinical trials. Fluorescence imaging was conducted with contrast agents specifically targeted to disease markers, enabling the detection of cancerous regions and measurement of therapeutic efficacies. The continuous wave (CW) fluorescence imaging modality consists of an intensified charge-coupled device (ICCD) or an electron-multiplying CCD (EMCCD) camera, both capable of detecting low fluorescence emission signals. In addition to high sensitivity, the fluorescence imaging modality allows for sub-second camera integration time even for small amounts of contrast agent. Therefore, dynamic fluorescence imaging should be able to track biodistribution and differentiate between tumor and normal tissue regions. The work presented in this thesis was conducted to (i) assess dose-dependent uptake using dynamic fluorescence imaging with pharmacokinetic (PK) models, (ii) evaluate disease target availability in potentially different tissue compartments in two different xenograft tumor models, (iii) compare the impact of autofluorescence in fluorescence imaging with NIR vs. red light excitable fluorescent contrast agents, (iv) examine fluorescence image-guided surgery and dual-wavelength fluorescence imaging of different tissues or targets, and (v) develop dynamic multi-wavelength whole-body fluorescence imaging with more than two different fluorescent contrast agents. The following conclusions were reached in the studies discussed above.

1. Dynamic fluorescence images were obtained from subcutaneous human Kaposi's sarcoma (KS1767) xenografts immediately following the i.v

injection of integrin targeting Cy5.5-c(KRGDf) at doses from 0.75 to 6 nmol/mouse. The fluorescence images were acquired using an intensified charge-coupled device (ICCD) system and were analyzed with a three-compartment pharmacokinetic (PK) model to determine uptake parameters in the tumor and normal tissue regions of interest as a function of administered dose. PK analysis showed that the uptake of Cy5.5-(KRGDf) in tumor regions were; (i) significantly greater than the contralateral normal tissue regions; (ii) linearly increased with dose of Cy5.5-c(KRGDf) up to 1.5 nmol/mouse; and (iii) were blocked by pre-injection of c(KRGDf). Above doses of 1.5 nmol/mouse, the uptake no longer increased with dose, suggesting integrin receptor saturation. In normal tissues, the PK uptake parameters were not influenced by Cy5.5-c(KRGDf) dose or preadministration of c(KRGDf).

2. Dynamic *in vivo* fluorescence optical imaging can enable assessment of early αvβ3 receptor availability in potentially different compartments: (i) on the proliferating endothelium within the vascular space, and/or (ii) on the surface of cancer cells in the extravascular space. In this study, xenografts bearing human Kaposi's sarcoma (KS1767) and human melanoma tumor (M21) were imaged following i.v. injection of αvβ3 targeting fluorescent contrast agent, Cy5.5-c(KRGDf). The tumor and contralateral normal tissue regions were evaluated using pharmacokinetic (PK) models and target to background ratios (TBRs). TBR and PK analysis showed that KS1767 exhibited early and rapid

uptake of Cy5.5-c(KRGDf) which was blocked by the prior administration of c(KRGDf) as a competitive binder to αvβ3. The results indicate that vascular αvβ3 receptors are readily available for Cy5.5-c(KRGDf) targeting as well as for competitive ligand with c(KRGDf). M21 tumors showed different characteristics from KS1767, with non-significant differences of TBR and early uptake rates between M21 and contralateral normal tissue regions. These results are consistent with the extravascular location of αvβ3 receptors on M21 cancer cells. Dynamic fluorescence imaging may provide insights into the different tissue compartments and mechanisms of therapeutic action of anti-angiogenic and cytotoxic agents.

3. Dynamic real-time fluorescence imaging was used to evaluate the impact of endogenous fluorescence with near infrared (NIR) and red light excitable fluorescent conjugates, IRDye800-EGF (780/830 nm Ex/Em) and Cy5.5-EGF (660/710 nm Ex/Em), respectively in mice bearing epidermal growth factor receptor (EGFR) positive xenografts. Fluorescence images were taken every 1.1 sec for a period of approximately 8 seconds immediately following i.v. injection of 1 nmol of IRDye800-EGF or Cy5.5-EGF each fluorescent contrast agent. Imaging showed fast distribution of fluorescent contrast agent through the chest, kidney, and head regions of interest (ROIs) in animals injected with IRDye800-EGF with excitation at 780 nm. The tumor was detected 4.4 sec after injection of IRDye800-EGF due to high permeability. However, internal organs were not seen upon injection of Cy5.5-EGF due to

high background autofluorescence from 660 nm excitation. When the TBR vs. time profiles were plotted for the chest, kidneys, and head as target ROIs using the stomach as the background ROI, the results showed that the TBR was significantly higher in mice injected with IRDye800-EGF than with Cy5.5-EGF. The low background at 830 nm autofluorescence measured through bandpass filter with 780 nm excitation made it possible not only image deep tissues, but also to evaluate near real-time biodistribution at early injection time points using dynamic fluorescence imaging.

4. NIR fluorescence images showed the uptake of fluorescent contrast agents in human Kaposi's sarcoma (KS SLK) tumor models. After NIR imaging, 24 hrs following injection of fluorescent conjugates, a second red light excitable fluorescent dye was injected and after 5 min, the lymphatics were imaged in the tumor region. The lymph nodes were then successfully dissected, as guided by fluorescence imaging. Dual-wavelength fluorescence imaging can be applied to characterize tumors by targeting different tissues, such as blood vessels, lymphatics, or tumors. Therefore, the ability to image both angiogenic and lymph vasculatures and follow the response to treatment will improve understanding of disease progression which should translate into more effective clinical therapeutics.
5. Whole-body dynamic multi-wavelength fluorescence imaging was accomplished using a liquid crystal tunable filter (LCTF). Since several different emission wavelengths can be selected by tuning the LCTF, two

wavelength dynamic fluorescence imaging was conducted in mice bearing M21 and M21L after injection of mixture of NIR fluorescent conjugated RGD peptide targeting to integrin αvβ3 and non-specific dye, Cy5.5. Dynamic multi-wavelength imaging with LCTF can differentiate the uptake of different fluorescent contrast agents between tumor and normal tissue ROIs in M21 and M21L xenograft models. Although fluorescence signals through the LCTF were two times lower than those from the holographic and bandpass filter set used previously, the results showed similar background rejection for both filter setups. In addition, LCTF can transmit shorter wavelengths than the peak in the excitation light spectrum, allowing excitation light to be used for "white" light images. Therefore, fluorescence images and white light images can be dynamically acquired one by one, which should enable image-guided surgery.

REFERENCES

[1] Tandon VR (2005). Alpha v beta 3 integrin: A novel therapeutic target. www.pharmainfo.net

[2] Lim HW and Soter NA (1993). *Clinical Photomedicine*. Dekker, New York, NY.

[3] Lakowicz JR (1999). *Principle of Fluorescence Spectroscopy*. Kluwer Acasdemic/Plenum Publishers, New York.

[4] Princeton Instruments (2005). Schematic of 'on-chip multiplication gain' in EMCCD camera system http://www.piacton.com/products/photonmax/default.aspx#1

[5] Slawson RW, Ninkov Z and Horch EP (1999). Hyperspectral imaging: Wide-Area spectrophotometry using a liquid-crystal tunable filter. *The Publications of the Astronomical Society of the Pacific*, **111**, 612-626.

[6] Dunn TB (1954). Normal and pathological anatomy of the reticular tissue in laboratory mice. *J Natl Cancer Inst*, 14, 1281-1434.

[7] Houston JP, Ke S, Wang W, Li C and Sevick-Muraca EM (2005). Quality analysis of *in vivo* NIR fluorescence and conventional gamma images acquired using a dual-labeled tumor-targeting probe. *J Biomed Opt*, **10**, 054010-054020.

[8] Kwon S, Ke S, Houston JP, Wang W, Wu Q, Li C and Sevick-Muraca EM (2005). Imaging dose-dependent pharmacokinetics of an RGD-fluorescent dye conjugate targeted to αvβ3 receptor expressed in Kaposi's sarcoma. *Mol Imaging*, **4**, 75-87.

[9] Hynes RO (1992). Integrins: versatility, modulation, and signaling in cell adhesion. *Cell*, **69**, 11-25.

[10] Hood JD and Cheresh DA (2002). Role of integrins in cell invasion and migration. *Nat Rev Cancer*, **2**, 91-100.

[11] Mizejewski GJ (1999). Role of integrins in cancer: Survey of expression patterns. *Exp Biol Med*, **222**, 124-138.

[12] Eliceiri BP and Cheresh DA (1999). The role of αv integrins during angiogenesis: Insights into potential mechanisms of action and clinical development. *J Clinl Invest*, **103**, 1227-1230.

[13] Marshall J, Rutherford D, Happerfield L, Hanby A, McCartney A, Newton-Bishop J and Hart I (1998). Comparative analysis of integrins *in vitro* and *in vivo* in uveal and cutaneous melanoma. *Br J Cancer*, **77**, 522-529.

[14] Beer AJ, Haubner R, Sarbia M, Goebel M, Luderschmidt S, Grosu AL, Schnell O, Niemeyer M, Kessler H, Wester H-J, Weber WA and Schwaiger M (2006). Positron emission tomography using [18F]Galacto-RGD identifies the level of integrin αvβ3 expression in man. *Clin Cancer Res*, **12**, 3942-3949.

[15] Kerr JS, Slee AM and Mousa SA (2002). The α_v integrin antagonists as novel anticancer agents: An update. *Expert Opin Investig Drugs*, **11**, 1765-1774.

[16] Haubner R, Weber WA, Beer AJ, Vabuliene E, Reim D, Sarbia M, Becker K-F, Goebel M, Hein R, Wester H-J, Kessler H and Schwaiger M (2005). Noninvasive visualization of the activated αvβ3 integrin in cancer patients by positron emission tomography and [^{18}F]Galacto-RGD. *PLOS Medicine*, **2**, 0244-0252.

[17] Sloan EK, Pouliot N, Stanley KL, Chia J, Moseley JM, Hards DK and Anderson RL (2006). Tumor-specific expressed of αvβ3 integrin promotes spontaneous metastasis of breast cancer to bone. *Breast Cancer Res*, **8**, R20.

[18] Brooks PC, Montgomery A, Rosenfeld M, Reisfeld R, Hu T, Klier G and Cheresh D (1994). Integrin αvβ3 antagonists promote tumor regression by inducing of angiogenic blood vessels. *Cell*, **79**, 1157-1164.

[19] Brooks PC, Stromblad S, Klemke R, Visscher D, Sarkar FH and Cheresh DA (1995). Antiintegrin αvβ3 blocks human breast cancer growth and angiogenesis in human skin. *J Clin Invest.*, **96**, 1815-1822.

[20] Friedlander M, Brooks PC, Shaffer RW, Kincaid CM, Varner JA and Cheresh DA (1995). Definition of two angiogenic pathways by distinct αv integrins. *Science*, **27**, 1500-1502.

[21] Bader BL, Rayburn H, Crowley D and Hynes RO (1998). Extensive vasculogenesis, angiogensis, and organogenesis precede lethality in mice lacking all αv integrins. *Cell*, **95**, 507-519.

[22] Huang XZ, Griffiths M, Wu JF, Farese RV and Sheppard D (2000). Normal development, wound healing, and adenovirus susceptibility in β5-deficient mice. *Mol Cell Biol*, **20**, 755-759.

[23] Hodivala-Dilke KM, McHugh KP, Tsakiris DA, Rayburn H, Crowley D, Ullman-Cullere M, Ross FP, Coller BS, Teitelbaum S and Hynes RO (1999). β3-Integrin-deficient mice are a model for Glanzmann Thrombasthenia showing placental defects and reduced survival. *J Clin Invest*, **103**, 229-238.

[24] Reynolds LE, Wyder L, Lively JC, Taverna D, Robinson SD, Huang X, Sheppard D, hynes RO and Hodivala-Dilke KM (2002). Enhanced pathological angiogenesis in mice lacking β3 integrin or β3 and β5 integrins. *Nat Med*, **8**, 27-34.

[25] Cheresh DA and Stupack DG (2002). Integrin-mediated death: An explanation of the integrin-knockout phenotype? *Nat Med*, **8**, 193-194.

[26] Sipkins DA, Cheresh DA, Kazenmi MR, Nevin LM, Bednarski MD and Li KCP (1998). Detection of tumor angiogenesis *in vivo* by αvβ3-targeted magnetic resonance imaging. *Nat Med*, **4**, 623-626.

[27] Anderson SA, Rader RK, Westlin WF, Null C, Jackson D, Lanza GM, Wickline SA and Kotyk JJ (2000). Magnetic resonance contrast enhancement of neovasculature with αvβ3-targeted nanoparticles. *Magn Reson Med*, **44**, 433-439.

[28] Winter PM, Morawski AM, Caruthers SD, Fuhrhop RW, Zhang H, Williams TA, Allen JS, Lacy EK, Robertson JD, Lanza GM and Wickline SA (2003). Molecular imaging of angiogenesis in early-stage atherosclerosis with αvβ3-integrin-targeted nanoparticles. *Circulation*, **108**, 2270-2274.

[29] Schmieder AH, Winter PM, Caruthers SD, Harris TD, Williams TA, Allen JS, Lacy EK, Zhang H, Scott MJ, Hu G, Robertson JD, Wickline SA and Lanza GM (2005). Molecular MR imaging of melanoma angiogenesis with αvβ3-targeted paramagnetic nanoparticles. *Magn Reson Med*, **53**, 621-627.

[30] Janssen ML, Oyen WJ, Dijkgraaf I, Massuger LF, Frielink C, Edwards DS, Rajopadhye M, Boonstra H, Corstens FH and Boerman OC (2002). Tumor targeting with radiolabeled αvβ3 integrin binding peptides in a nude mouse model. *Cancer Res*, **42**, 6146-6151.

[31] Sadeghi MM, Krassilnikova S, Zhang J, Gharaei AA, Fassaei HR, Esmailzadeh L, Kooshkabadi A, Edwards S, Yalamanchili P, Harris TD, Sinusas AJ, Zaret BL and Bender JR (2004). Detection of injury-induced vascular remodeling by targeting activated αvβ3 integrin *in vivo*. *Circulation*, **110**, 84-90.

[32] Meoli DF, Sadeghi MM, Krassilnikova S, Zhang J, Gharaei AA, Fassaei HR, Esmailzadeh L, Kooshkabadi A, Edwards S, Yalamanchili P, Harris TD, Sinusas AJ, Zaret BL and Bender JR (2004). Detection of injury-induced vascular remodeling by targeting activated αvβ3 integrin *in vivo*. *J Clin Invest*, **113**, 1684-1691.

[33] Sivolapenko GB, Skarlos D, Pectasides D, Stathopoulou E, Milonakis A, Sirmalis G, Stuttle A, Courtenay-Luck NS, Konstantinides K and Epenetos AA (1998). Imaging of metastatic melanoma utilising a technetium-99m labelled RGD-containing synthetic peptide. *Eur J Nucl Med*, **25**, 1383-1389.

[34] Posey JA, Khazaeli MB, DelGrosso A, Saleh MN, Lin CY, Huse W and LoBuglio AF (2001). A pilot trial of Vitaxin, a humanized anti-vitronectin receptor (anti αvβ3) antibody in patients with metastatic cancer. *Cancer Biother Radiopharm*, **16**, 125-132.

[35] Haubner R and Wester HJ (2004). Radiolabeled tracers for imaging of tumor angiogenesis and evaluation of anti-angiogenic therapies. *Curr Pharm Des*, **10**, 1439-1455.

[36] Ellegala DB, Leong-Poi H, Carpenter JE, Klibanov AL, Kaul S, Shaffrey ME, Sklenar J and Lindner JR (2003). Imaging tumor angiogenesis with contrast ultrasound and microbubbles targeted to αvβ3. *Circulation*, **108**, 336-341.

[37] Leong-Poi H, Christiansen J, Klibanov AL, Kaul S and Linder JR (2003). Noninvasive assessment of angiogenesis by ultrasound and microbubbles targeted to αv-integrins. *Circulation*, **107**, 455-460.

[38] Leong-Poi H, Christiansen J, Heppner P, Lewis CW, Klibanov AL, Kaul S and Lindner JR (2005). Assessment of endogenous and therapeutic arteriogenesis by contrast ultrasound molecular imaging of integrin expression. *Circulation*, **111**, 3248-3254.

[39] Weller GER, Wong MKK, Modzelewski RA, Lu E, Klibanov AL, Wagner WR and Villanueva FS (2005). Ultrasonic imaging of tumor angiogenesis using contrast microbubbles targeted via the tumor-binding peptide arginine-arginine-leucine. *Cancer Res*, **65**, 533-539.

[40] Chen X, Conti PS and Moats RA (2004). *In vivo* near-infrared fluorescence imaging of integrin αvβ3 in brain tumor xenografts. *Cancer Res.*, **64**, 8009-8014.

[41] Cheng Z, Wu Y, Xiong Z, Gambhir SS and Chen X (2005). Near-infrared fluorescent RGD peptides for optical imaging of integrin αvβ3 expression in living mice. *Bioconjug Chem*, **16**, 1433-1441.

[42] Wu Y, Cai W and Chen X (2006). Near-infrared fluorescence imaging of tumor integrin alpha (v) beta (3) expression with Cy7-labeled RGD multimers. *Mol Imaging Biol*, **4**, 226-236.

[43] Wang W, Ke S, Wu Q, Charnsangavej C, Gurfinkel M, Gelovani JG, Sevick-Muraca EM and Li C (2005). Near-infrared optical imaging of integrin αvβ3 in human tumor xenografts. *Mol Imaging,*, **3**, 343-351.

[44] Gurfinkel M, Ke S, Wang W, Li C and Sevick-Muraca EM (2005). Quantifying molecular specificity of αvβ3 integrin-targeted optical contrast agents with dynamic optical imaging. *J Biomed Opt.*, **10**, 034019-1-9.

[45] Houston JP, Thompson AB, Gurfinkel M and Sevick-Muraca EM (2003). Sensitivity and depth penetration of continuous wave versus frequency-domain photon migration near-infrared fluorescence contrast.enhanced imaging. *Photochem Photobiol*, **77**, 420-430.

[46] Chen X, Hou Y, Tohme M, Park R, Khankaldyyan V, Gonzales-Gomez I, Bading JR, Laug WE and Conti PS (2004). Pegylated arg-gly-asp peptide: ^{64}Cu labeling and PET imaging of brain tumor αvβ3-integrin expression. *J Nucl Med*, **45**, 1776-1783.

[47] Chen X, Park R, Hou Y, Tohme M, Shahinian AH, Bading JR and Conti PS (2004). MicroPET and autoradiographic imaging of breast cancer αv-integrin expression using ^{18}F- and ^{64}Cu-labeled RGD peptide. *Bioconj Chem*, **15**, 41-49.

[48] Chen X, Park R, Hou Y, Khankaldyyan V, Gonzales-Gomez I, Tohme M, Bading JR, Laug WE and Conti PS (2004). MicroPET imaging of brain tumor angiogenesis with ^{18}F-labeled PEGylated RGD peptide. *Eur J Nuc Med Mol Imaging*, **31**, 1081-1089.

[49] Haubner R, Wester H-J, Weber WA, Mang C, Ziegler SI, Goodman SL, Senekowitsch-Schmidtke R, Kessler H and Schwaiger M (2001). Noninvasive imaging of αvβ3 integrin expressing using ^{18}F-labeled RGD-containing glycopeptide and positron emission tomography. *Cancer Res*, **61**, 1781-1785.

[50] Haubner R, Wester HJ, Burkhart F, Senekowitsch-Schmidtke R, Weber W, Goodman SL, Kessler H and Schwaiger M (2001). Glycosylated RGD-containing peptides: Tracer for tumor targeting and angiogenesis imaging with improved biokinetics. *J Nucl Med*, **42**, 326-336.

[51] Haubner R, Wester HJ, Reuning U, Senekowitsch-Schmidtke R, Diefenbach B, Kessler H, Stocklin G and Schwaiger M (1999). Radiolabeled αvβ3 integrin atagonists: A new class of tracers for tumor targeting. *J Nucl Med*, **40**, 1061-1071.

[52] Chen X, Conti PS and Moats RA (2004). *In vivo* near-infrared fluorescence imaging of integrin αvβ3 in brain tumor xenografts. *Cancer Res*, **64**, 8009-8014.

[53] Hua J, Dobrucki LW, Sadeghi MM, Zhang J, Bourke BN, Cavaliere P, Song J, Chow C, Jahanshad N, Royen Nv, Buschmann I, Madri JA, Mendizabal M and Sinusas AJ (2005). Noninvasive imaging of angiogenesis with a 99mTc-labeled peptide targeted at αvβ3 Integrin after murine hindlimb ischemia. *Circulation*, **111**, 3255-3260.

[54] Poethko T, Schottelius M, Thumshirn G, Hersel U, Herz M, Henriksen G, Kessler H, Schwaiger M and Wester HJ (2004). Two-step methodology for high-yield routine radiohalogenation of peptides: ^{18}F-labeled RGD and octreotide analogs. *J Nucl Med*, **45**, 892-902.

[55] Li C, Wang W, Wu Q, Houston JP, Sevick-Muraca EM, Dong L, Chow D, Charnsangavej C and Gelovani JG (2006). Dual optical and nuclear imaging of integrin αvβ3 in human melanoma xenografts using a single imaging Probe. *Nucl Med Biol*, **33**, 349-358.

[56] Hagen PMv, Breeman WAP, Bernard HF, Schaar M, Mooij CM, Srinivasan A, Schmidt MA, Krenning EP and Jong Md (2000). Evaluation of a radiolabelled cyclic DTPA-RGD analogue for tumour imaging and radionuclide therapy. *Int J Cancer*, **90**, 186-198.

[57] Cheng Z, Levi J, Xiong Z, Gheysens O, Keren S, Chen X and Gambhir SS (2006). Near-infrared fluorescent deoxyglucose analogue for tumor optical imaging in cell culture and living mice. *Bioconjug Chem*, **3**, 662-669.

[58] Line BR, Mitra A, Nan A and Ghandehari H (2005). Targeting tumor angiogenesis: Comparison of pPeptide and polymer-peptide conjugates. *J Nucl Med*, **9**, 1552-1560.

[59] Cambridge Research & Instrumentation, Inc (2000). Varispec^{TM}, liquid crystal tunable imaging filter,.
http://www.cri-inc.com/Pages/search/VariSpec.html.

[60] Felding-Habermann B, O'Toole TE, Smith JW, Fransvea E, Ruggeri ZM, Ginsberg MH, Hughes PE, Pampori N, Shattil SJ, Saven A and Mueller BM (2001). Integrin activation controls metastasis in human breast cancer. *Proc Natl Acad Sci USA*, **98**, 1853-1858.

[61] Friedlander M, Brooks PC, Shaffer RW, Kincaid CM, Varner JA and Cheresh DA (1995). Definition of two angiogenic pathways by distinct α_v integrins. *Science*, **270**, 1500-1502.

[62] Wong NC, Mueller BM, Barbas CF, Ruminski P, Quaranta V, Lin ECK and Smith JW (1998). Alpha (v) integrins mediate adhesion and migration of breast carcinoma cell lines. *Clin Exp Metastasis*, **16**, 50-61.

[63] Albelda SM, Mette SA, Elder DE, Stewart R, Damjanovich L, Herlyn M and Buck CA (1990). Integrin distribution in malignant melanoma: Association of the beta 3 subunit with tumor progression. *Cancer Res*, **50**, 6756-6764.

[64] Stromblad S and Cheresh DA (1996). Integrins, angiogenesis and vascular cell survival. *Chem Biol*, **3**, 881-885.

[65] Folkman J (1985). Toward an understanding of angiogenesis: Search and discovery. *Perspect Biol Med*, **29**, 10-36.

[66] Carmeliet P and Jain RK (2000). Angiogenesis in cancer and other diseases. *Nature*, **407**, 249-257.

[67] Clark RA, Tonnesen MG, Gailit J and Cheresh DA (1996). Transient functional expression of αvβ3 on vascular cells during wound repair. *Am J Pathol*, **148**, 1407-1421.

[68] Max R, Gerritsen RRCM, Nooijen PTGA, Goodman SL, Sutter A, Keilholz U, Ruiter DJ and DeWaal RM (1997). Immunohistochemical analysis of integrin αvβ3 expression on tumor-associated vessels of human carcinomas. *Int J Cancer*, **71**, 320-324.

[69] Natali PG, Hamby CV, Felding-Habermann B, Liang BT, Nicotra MR, DiFilippo F, Giannarelli D, Temponi M and Ferrone S (1997). Clinical significance of alpha(v)beta(3) integrin and intercellular adhesion molecule-1 expression in cutaneous malignant melanoma lesions. *Cancer Res*, **57**, 1554-1560.

[70] Eliceiri BP and Cheresh DA (1999). The role of av integrins during angiogenesis: Insights into potential mechanisms of action and clinical development. *J Clin Invest*, **103**, 1227-1230.

[71] Felding-Habermann B, Mueller BM, Romerdahl CA and Cheresh DA (1992). Involvement of integrin αv gene expression in human melanoma tumorigenicity. *J Clin Invest*, **89**, 2018-2022.

[72] Brooks PC, Montgomery AM, Rosenfeld M, Reisfeld RA, Hu T, Klier G and Cheresh DA (1994). Integrin αvβ3 antagonists promote tumor regression by inducing apoptosis of angiogenic blood vessels. *Cell*, **79**, 1157-1164.

[73] Buckley C, Pilling D, Henriquez N, Parsonage G, Threlfall K, Scheel-Toellner D, Simmons D, Albar A, Lord J and Salmon M (1999). RGD peptides induce apoptosis by direct caspase-3 activation. *Nature*, **397**, 534-539.

[74] Zitzmann S, Ethemann V and Schwab M (2002). Arginine-Glycine-Aspartic (RGD)-peptide binds to both tumor and tumor-endothelial cells *in vivo*. *Cancer Res*, **62**, 5139-5143.

[75] Safai B, Johnson KG, Myskowski PL, Koziner B, Yang SY, Cunningham-Rundles S, Godbold JH and Dupont B (1985). The natural history of Kaposis's sarcoma in the acquired immunodeficiency syndrome. *Ann Intern Med*, **103**, 744-750.

[76] Rader C, Popkov M, Neves JA and Barbas CFI (2002). Integrin αvβ3 targeted therapy for Kaposi's sarcoma with an *in vitro* evolved antibody. *FASEB J*, **16**, 2000-2002.

[77] Benelli R, Adatia R, Ensoli B, Stetler-Stevenson WG, Santi L and Albini A (1994). Inhibition of AIDS-Kaposi's sarcoma cell induced endothelial cell invasion by TIMP-2 and a synthetic peptide from the metalloproteinase propeptide: Implications for an anti-angiogenic therapy. *Oncol Res*, **6**, 251-257.

[78] Hwang K, Houston JP, Rasmussen J, Ke S, Li C and Sevick-Muraca EM (2005). Enhanced fluorescent optical imaging with improved excitation light rejection. *Mol Imaging*, **4**, 194-204.

[79] Castel S, Pagan R, Mitjans F, Piulats J, Goodman S, Jonczyk A, Huber F, Vilaro S and Reina M (2001). RGD peptides and monoclonal antibodies, antagonists of α_v-integrin, enter the cells by independent endocytic pathways. *Lab Invest*, **81**, 1615-1626.

[80] Kok RJ, Schraa AJ, Bos EJ, Moorlag HE, Asgeirsdottir SA, Everts M, Meijer DKF and Molema G (2002). Prepararion and functional evaluation of RGD-modified proteins as αvβ3 integrin directed therapeutics. *Bioconjug Chem*, **13**, 128-135.

[81] Vera DR and Mattrey RF (2002). A molecular CT blood pool contrast agent. *Acad Radiol*, **9**, 784-792.

[82] Godavarty A, Thompson AB, Roy R, Eppstein MJ, Zhang C and Sevick-Muraca EM (2005). Detection of multiple targets in breast phantoms using fluorescence enhanced optical imaging. *Radiology*, **32**, 992-1000.

[83] Ntziachristos V, Tung CH, Bremer C and Weissleder R (2002). Fluorescence molecular tomography resolves protease activity *in vivo*. *Nat Med*, **8**, 757-761.

[84] Rader C, Popkov M, Neves JA and III CFB (2002). Integrin αvβ3 targeted therapy for Kaposi's sarcoma with an *in vivo* evolved antibody. *FASEB*, **16**, 2000-2002.

[85] Samaniego F, Young D, Grimes C, Prospero V, Christofidou-Solomidou M, DeLisser HM, Prakash O, Sahin AA and Wang S (2002). Vascular endothelial growth factor and Kaposi's sarcoma cells in human skin grafts. *Cell Growth Differ*, **13**, 387-395.

[86] Benelli R, Adatia R, Ensoli B, Stetler-Stevenson WG, Santi L and Albibi A (1994). Inhibition of AIDS-Kaposi's sarcoma cell induced endothelial cell invasion by TIMP-2 and a synthetic peptide from the metalloproteinase propeptide: Implications for an anti-angiogenic therapy. *Oncol Res*, **6**, 251-257.

[87] Allman R, Cowburn P and Mason M (2000). *In vitro* and *in vivo* effects of a cyclic peptide with affinity for the αvβ3 integrin in human melanoma cells. *Eur J Cancer*, **36**, 410-422.

[88] Petrirclerc E, Stromblad S, Schalscha TLv, Mitjans F, Piulats J, Montgomery AMP, Cheresh DA and Brooks PC (1999). Integrin αvβ3 promotes M21 melanoma growth in human skin by regulating tumor cell survival. *Cancer Res.*, **59**, 2724-2730.

[89] Felding-Habermann B, Mueller BM, Romerdahl CA and Cheresh DA (1992). Involvement of integrin av gene expression in human melanoma tumorigenicity. *J Clin Invest*, **89**, 2018-2022.

[90] Jain RK (1990). Vascular and interstitial barriers to delivery of therapeutic agents in tumors. *Cancer Metastasis Rev.*, **9**, 253-266.

[91] Wester HJ and Kessler H (2005). Molecular Targeting with Peptides or Peptide-Polymer Conjugates: Just a Question of Size? *J Nucl Med*, **46**, 1940-1945.

[92] DeNardo SJ, Burke PA, Leigh BR, O'Donnell RT, Miers LA, Kroger LA, Goodman SL, Matzku S, Jonczyk A, Lamborn KR and DeNardo GL (2000). Neovascular targeting with cyclic RGD peptide (cRGDf-ACHA) to enhance delivery of radioimmunotherapy. *Cancer Biothe Radiopharm*, **15**, 71-79.

[93] Abdollahi A, Griggs DW, Zieher H, Roth A, Lipson KE, Saffrich R, Grone H-J, Hallahan DE, Reisfeld RA, Debus J, Niethammer AG and Huber PE (2005). Inhibition of αvβ3 integrin survival signaling enhances antiangiogenic and antitumor effects of radiotherapy. *Clin Cancer Res,* **17**, 6270-6279.

[94] GE Healthcare (2001). Excitation / emission wavelengths of Cy5.5 dye http://www1.amershambiosciences.com.

[95] Reilly RM, Kiarash R, Sandhu J, Lee YW, Cameron RG, Hendler A, Vallis K and Gariepy J (2000). A comparison of EGF and MAb 528 labeled with ^{111}In for imaging human breast cancer. *J Nucl Med*, ***41***, 903-911.

[96] Rusckowski M, Qu T, Chang F and Hnatowich DJ (1997). Technetium-99m labeled epidermal growth factor-tumor imaging in mice. *J Peptide Res*, **50**, 393-401.

[97] Goldenberg A, Masui H, Divgi C, Kamrath H, Pentlow K and Mendelsohn J (1989). Imaging of human tumor xenografts with an indium-111-labeled anti-epidermal growth factor receptor monoclonal antibody. *J Natl Cancer Inst*, **81**, 1616-1625.

[98] Yang W, Barth RF, Leveille R, Adams DM, Ciesielski N, Fenstermaker RA and Capala J (2001). Evaluation of systemically administered radiolabeled epidermal growth factor as a brain tumor targeting agent. *J Neuro-Oncology*, **55**, 19-28.

[99] Ortu G, Ben-David I, Rozen Y, Freedman NMT, Chisin R, Levitzli A and Mishani E (2002). Lalbeld EGFR-TK irreversibleinhibitor (ML03): *In vitro* and *in vivo* properties, potential as PET biomarker for cancer and feasibility as anticancer drug. *Int J Cancer*, **101**, 360-370.

[100] Divgi CR, Welt S, Kris M, Real FX, Yeh SDJ, Gralla R, Merchant B, Schweighart S, Unger M, Larson SM and Mendelsohn J (1991). Phase I and imaging trial of indium 111-labeled anti-epidermal growth factor receptor monoclonal antibody 225 in patient with squamous cell lung carcinoma. *J Natl Cancer Inst*, **83**, 97-104.

[101] Wen X, Wu Q-p, Ke S, Ellis L, Charnsangavej C, Delpassand AS, Wallace S and Li C (2001). Conjugation with ^{111}In-DTPA-Poly(Ethylene Glycol) improves imaging of anti-EGF receptor antibody C225. *J Nucl Med*, **42**, 1530-1537.

[102] Schechter NR, Yang DJ, Azhdarinia A, Kohanim S, Wendtlll R, Oh C-S, Hu M, Yu D-F, Bryant J, Ang KK, Forster KM, Kim EE and Podoloff DA (2003). Assessment of epidermal growth factor receptor with ^{99m}Tc-Ethylenedicysteine-C225 monoclonal antibody. *Anti-Cancer Drugs*, **14**, 49-56.

[103] Meenakshi A, Ganesh V, N. RSK and Kumar S (2003). Radioimmuno targeting ^{99mc}Technetium labeled anti-epidermal growth factor receptor monoclonal antibodies in experimental tumor models. *Q J Nucl Med*, **47**, 189-144.

[104] Iznaga-Escobar N, Arocha LAT, Morales AM, Suzarte MR, Mesa NR and Rodriguez RP (1998). Technetium-99m-antiepidermal growth factor receptor antibody in patients with tumors of epithelial origin: Part II. pharmacokinetics and clearances. *J Nucl Med*, **39**, 1918-1927.

[105] Ramos-Suzarte M, Rodriguez N, Oliva JP, Iznaga-Escobar N, Perera A, Morales A, Gonzalez N, Cordero M, Torres L, Pimentel G, Borron M, Gonzalez J, Torres O, Rodriguez T and Perez R (1999). 99mcTc-Labeled antihuman epidermal growth factor receptor antibody in patients with tumors of epithelial origin: Part III. Clinical Trials Safety and Diagnostic Efficacy. *J Nucl Med*, **40**, 768-775.

[106] Onn A, Choe DH, Herbst RS, Correa AM, Munden RF, Truong MT, Vaporciyan AA, Isobe T, Gilcrease MZ and Marom EM (2005). Tumor carvitation in stage I non-small cell lung cancer: Epidermal growth factor receptor expression and prediction of poor outcome. *Radiology*, **237**, 342-347.

[107] Abdel-Nabi H, Doerr RJ, Chan H-W, Balu D, Schmelter RF and Maguire RT (1990). In-111-Labeled monoclonal antibody immunoscintigraphy in colorectal carcinoma: Safety, sensitivity, and preliminary clinical results. *Radiology*, **175**, 163-171.

[108] Schatten C, Pateisky N, Vavra N, Ehrenbock P, Angelberger P, Sivolapenko G and Epenetos A (1991). Lymphoscintigraphy with ^{123}I-labeled epidermal growth factor. *Lancet*, **337**, 395-396.

[109] Dadparvar S, Krishna L, Miyamoto C, Brady LW, Brown SJ, Bender H, Slizofski WJ, Eshleman J, Chevres A and Woo DV (1994). Indium-111-labeled anti-EGFr-425 scintigraphy in the detection of malignant gliomas. *Cancer*, **73**, 884-889.

[110] Kalofonos HP, Pawlikowska TR, Hemingway A, Courtenay-Luck N, Dhokia B, Snook D, Sivolapenko GB, Hooker GR, McKenzie CG, Lavender PJ, Thomas DGT and Epenetos AA (1989). Antibody guided diagnosis and therapy of brain gliomas using radiolabeled monoclonal antibodies against epidermal growth factor receptor and placental alkaline phosphatase. *J Nucl Med*, **30**, 1636-1646.

[111] Vallis KA, Reilly RM, Chen P, Oza A, Hendler A, Cameron R, Hershkop M, Iznaga-Escobar N, Ramos-Suzarte M and Keane P (2002). A Phase I study of ^{99m}Tc-hR3 (DiaCIM), a humanized immunoconjugate directed towards the epidermal growth factor receptor. *Nuclear Medicine Communications*, **23**, 1155-1164.

[112] Lee HJ and Pardridge WM (2003). Monoclonal antibody radiopharmaceuticals: cationization, pegylation, radiometal chelation, pharmacokinetics, and tumor imaging. *Bioconj Chem*, **14**, 546-553.

[113] Cornelissen B, Kersemans V, Burvenich I, Oltenfreiter R, Vanderheyden J, Boerman O, Vanderwiele C and Slegers G (2005). Synthesis, biodistribution and effects of farnesyltransferase inhibitor therapy on tumour uptake in mice of ^{99m}Tc labelled epidermal growth factor. *Nucl Med Commun*, ***26***, 147-153.

[114] Vinter-Jensen L, Frokiaer J, Jorgensen PE, Marqversen J, Rehling M, Dajani EZ and Nexo E (1995). Tissue distribution of 131I-Labeled epidermal growth factor in the pig visualized by dynamic scintigraphy. *J Endocrinology*, **144**, 5-12.

[115] Ke S, Wen X, Gurfinkel M, Charnsangavej C, Wallace S, Sevick-Muraca EM and Li C (2003). Near-infrared optical imaging of epidermal growth factor receptor in breast cancer xenografts. *Cancer Res*, **63**, 7870-7875.

[116] Berard V, Rousseau JA, Cadorette J, Hubert L, Bentourkia Mh, Lier HEv and Lecomte R (2006). Dynamic imaging of transient metabolic processes by small-animal PET for the evaluation of photosensitizers in photodynamic therapy of cancer. *J Nucl Med*, **47**, 1119-1126.

[117] Gurfinkel M, Thompson AB, Ralston W, Troy TL, Ana L. Moore, Moore TA, Gust JD, Tatman D, Reynolds JS, Bruce Muggenburg, Nikula K, Pandey R, Mayer RH, Hawrysz DJ and Sevick-Muraca EM (2000). Pharmacokinetics of ICG and HPPH-car for the detection of normal and tumor tissue using fluorescence, near-infrared reflectance imaging: A case study. *Photochem. Photobiol*, **72**, 94-102.

[118] Ntziachristos V, Yodh AG, Schnall M and Chance B (2000). Concurrent MRI and diffuse optical tomography of breast after indocyanine green enhancement. *PNAS*, **97**, 2767-2772.

[119] Cuccia DJ, Bevilacqua F, Durkin AJ, Merritt S, Tromberg BJ, Gulsen G, Yu H, Wang J and Nalcioglu O (2003). *In vivo* quantification of optical contrast agent dynamics in rat tumors by use of diffuse optical spectroscopy with magnetic resonance imaging coregistration. *Applied Optics*, **42**, 2940-2950.

[120] Izumi Y, Xu L, Tomaso Ed, Fukumura D and Jain RK (2002). Herceptin acts as an anti-angiogenic cocktail. *Nature*, **416**, 279-280.

[121] Chung K, Shia J, Kemeny NE, Shah M, Schwartz GK, Tse A, Hamilton A, Pan D, Schrag D, Schwartz L, Klimstra DS, Fridman D, Kelsen DP and Saltz LB (2005). Cetuximab shows activity in colorectal cancer patients with tumors that do not express the epidermal growth factor receptor by immunohistochemistry. *J Clin Oncol*, **23**, 1803-1810.

[122] Troy T, Jekic-McMullen D, Sambucetti L and Rice B (2004). Quantitative comparison of the sensitivity of detection of fluorescent and bioluminescence reporters in animal models. *Mol Imaging*, **3**, 9-23.

[123] Frangioni JV (2003). *In vivo* near-infrared fluorescence imaging. *Curr Opin Chem Biol*, **7**, 626-634.

[124] Weagle G, Paterson PE, Kennedy J and Pottier R (1988). The nature of the chromophore responsible for naturally occurring fluorescence in Mouse Skin. *Photochem Photobiol B*, **2**, 313-320.

[125] Gao X, Cui Y, Levenson RM, Chung LWK and Nie S (2004). *In vivo* cancer targeting and imaging with semiconductor quantum dots. *Nat Biotechol*, **22**, 969-976.

[126] McNeill GC, Witte MH, Witte CL, Williams WH, Hall JN, Patton DD, Pond GD and Woolfenden JM (1989). Whole-body lymphangioscintigraphy: preferred method for initial assessment of the peripheral lymphatic system. *Radiology*, **172**, 495-502.

[127] O'Mahony S, Rose SL, Chilvers AJ, Ballinger JR, Solanki CK, Barber RW, Mortimer PS, Purushotham AD and Peters AM (2004). Finding an optimal method for imaging lymphatic vessels of the upper limb. *Eur J Nucl Med Mol Imaging*, **31**, 555-563.

[128] Ellner SJ, Hoh CK, Vera DR, Darrah DD, Schulteis G and Wallace AM (2003). Dose-dependent biodistribution of [(99m)Tc]DTPA-mannosyl-dextran for breast cancer sentinel lymph node mapping. *Nucl Med Biol*, **30**, 805-810.

[129] Wallace AM, Hoh CK, Vera DR, Darrah DD and Schulteis G (2003). Lymphoseek: A molecular radiopharmaceutical for sentinel node detection. *Ann Surg Oncol*, **10**, 531-538.

[130] Suga K, Yuan Y, Ogasawara N, Okada M and Matsunaga N (2003). Visualization of normal and interrupted lymphatic drainage in dog legs with interstitial MR lymphography using an extracellular MR contrast agent, gadopentetate dimeglumine. *Invest Radiol*, **38**, 349-357.

[131] Liu N, Wang C and Sun M (2005). Noncontrast three-dimensional magnetic resonance imaging vs lymphoscintigraphy in the evaluation of lymph circulation disorders: A comparative study. *J Vasc Surg*, **41**, 69-75.

[132] Tangoku A, Yamamoto S, Suga K, Ueda K, Nagashima Y, Hida M, Sato T, Sakamoto K and Oka M (2004). Sentinel lymph node biopsy using computed tomography-lymphography in patients with breast cancer. *Surgery*, **135**, 258-265.

[133] Utech CI, Young CS and Winter PF (1996). Prospective evaluation of fluorine-18 fluorodeoxyclucose positron emission tomography in breast cancer for staging of the axilla related to surgery and immunocytochemistry. *Eur J Nucl Med*, **23**, 1588-1593.

[134] Adler LP, Faulhaber PF, Schnur KC, Al-Kasi NL and Shenk RR (1997). Axillary lymph node metastases: Screening with [F-18]2-deoxy-2-fluoro-D-glucose (FDG) PET. *Radiology*, **203**, 323-327.

[135] Smith IC, Ogston KN, Whitford P, Smith FW, Sharp P, Norton M, Miller ID, Ah-See AK, Heys SD, Jibril JA and Eremin O (1998). Staging of the axilla in breast cancer: Accurate *in vivo* assessment using positron emission tomography with 2-(fluorine-18)-fluoro-2-deoxy-D-glucose. *Ann Surg*, **228**, 220-7.

[136] Hubner KF, Smith GT, Thie JA, Bell JL, Nelson HS and Hanna WT (2000). The potential of F-18-FDG PET in breast cancer. Detection of primary lesions, axillary lymph node metastases, or distant metastases. *Clin Positron Imaging*, **3**, 197-205.

[137] Greco M, Crippa F, Agresti R, Seregni E, Gerali A, Giovanazzi R, Micheli A, Asero S, Ferraris C, Gennaro M, Bombardieri E and Cascinelli N (2001). Axillary lymph node staging in breast cancer by 2-fluoro-2-deoxy-D-glucose-positron emission tomography: Clinical evaluation and alternative management. *J Natl Cancer Inst*, **93**, 630-635.

[138] Ivancevic VV, Wolter A, Winzer K, Aldinger H, Muller JM and Munz DL (2000). Intraindividual comparison of F-18-Fluorodeoxyglucose and Tc-99m-Tetrofosmin in planar scintimammography and SPECT. *Clin Positron Imaging*, **3**, 17-29.

[139] Yutani K, Shiba E, Kusuoka H, Tatsumi M, Uehara T, Taguchi T, Takai SI and Nishimura T (2000). Comparison of FDG-PET with MIBI-SPECT in the detection of breast cancer and axillary lymph node metastasis. *J Comput Assist Tomogr*, **24**, 274-280.

[140] Guller U, Nitzsche EU, Schirp U, Viehl CT, Torhorst J, Moch H, Langer I, Marti WR, Oertli D, Harder F and Zuber M (2002). Selective axillary surgery in breast cancer patients based on positron emission tomography with 18F-fluoro-2-deoxy-D-glucose: Not yet! *Breast Cancer Res Treat*, **71**, 171-173.

[141] van der Hoeven JJ, Hoekstra OS, Comans EF, Pijpers R, Boom RP, van Geldere D, Meijer S, Lammertsma AA and Teule GJ (2002). Determinants of diagnostic performance of [F-18]fluorodeoxyglucose positron emission tomography for axillary staging in breast cancer. *Ann Surg*, **236**, 619-624.

[142] Barranger E, Grahek D, Antoine M, Montravers F, Talbot JN and Uzan S (2003). Evaluation of fluorodeoxyglucose positron emission tomography in the detection of axillary lymph node metastases in patients with early-stage breast cancer. *Ann Surg Oncol*, **10**, 622-627.

[143] Jain RK and Padera TP (2002). Prevention and treatment of lymphatic metastasis by antilymphangiogenesis therapy. *J Natl Cancer Inst*, **94**, 785-787.

[144] Kim S, Lim YT, Soltesz EG, Grand AMD, Lee J, Nakayama A, Parker JA, Mihaljevic T, Laurence RG, Dor DM, Cohn AH, Bawendi MG and Frangioni JV (2004). Near-infrared fluorescent type II quantum dots for sentinel lymph node mapping. *Nat Biotechnol*, **22**, 93-97.

[145] Vo-Dinh T, Cullum B and Kasili P (2003). Development of a multi-spectral imaging system for medical application. *J Phys D*, **36**, 1663-1668.

[146] Farkas DL and Becker D (2001). Application of spectral imaging: Detection and analysis of human melanoma and its precursors. *Pigment Cell Res*, **14**, 2-8.

[147] Zimmermann T, Rietdorf J and Pepperkok R (2003). Spectral imaging and its applications in live cell microscopy. *FEBS Letters*, **546**, 87-92.

[148] Mansfield JR, Sowa MG and Mantsch HH (2000). Development of LCTF-based visible and near-IR spectroscopic imaging systems for macroscopic samples. *Proc SPIE*, 99-107.

[149] Farkas DL, Du C, Fisher GW, Lau C, Niu W, Wachman ES and Levenson RM (1998). Non-invasive image acquisition and advanced processing in optical bioimaging. *Comput Med Imaging Graph*, **22**, 89-102.

[150] Mansfield JR, Gossage KW, Hoyt CC and Levenson RM (2004). Autofluorescence removal, multiplexing, and automated analysis methods for in-vivo fluorescence imaging. *J Biomed Opt,* **10**, 1-9.

[151] Grand AMD and Frangioni JV (2003). An Operational Near-infrared fluorescence imaging system prototype for large animal surgery. *Technol Cancer Res Treat*, **2**, 1-10.

[152] Wang W, McMurray JS, Wu Q, Campbell ML and Li C (2005). Convenient solid-phase synthesis of diethylenetriaminepenta-acetic acid (DTPA)- conjugated cyclic RGD peptide analogues. *Cancer Biother Radiopharm*, **20**, 547-556.

VITA

SUN KUK KWON

13107 Imperial Shore Dr.
Pearland, TX, 77584

EDUCATION

Texas A&M University, College Station, TX
Ph.D., Chemical Engineering, December 2006

Hanyang University, Seoul, South Korea
B.S., Chemical Engineering, February 2002

PEER-REVIEWED PUBLICATIONS

Kwon S, Ke S, Rasmussen J, Wang W, Cameron AG, and Sevick-Muraca EM (2006). Dynamic Multi-wavelength Whole-Body Fluorescence Imaging with Liquid Crystal Tunable Filter. *J Biomed Opt*, in preparation.

Ke S, Yallampalli A, Kwon S, Wang W, Adams KE, Cameron AG, Mawad ME, and Sevick-Muraca EM (2006). Multimodal (Optical/SPECT/PET/CT) Imaging Tumor Interleukin 11 Receptor and Metabolic Status in Small Animal Xenograft. *Radiology*, in preparation.

Wang W, Ke S, Kwon S, Yallampalli S, Cameron AG, Adams KE, Mawad ME, and Sevick-Muraca EM (2006). A Dual-Labled Optical and Nuclear Imaging Agent Targeting Interleukin 11 Receptor Alpha-Chain. Submitted to *Bioconj Chem*.

Adams KE, Ke S, Kwon S, Liang F, Fan Z, Lu Y, Barry MA, Hirshi K, Mawad ME, and Sevick-Muraca EM (2006). Comparison of small animal imaging performance using visible and near-infrared wavelength excitable fluorescent dyes for targeting cancer. Submitted to *J Biomed Opt.*

Kwon S, Ke S, Houston JP, Wang W, Wu Q, Li C, and Sevick-Muraca EM (2005). Imaging dose-dependent pharmacokinetics of an RGD-fluorescent dye conjugate targeted to alpha v beta 3 receptor expressed in Kaposi's sarcoma. *Mol Imaging*, **4**, 75-87.